Max Planck Institut für Kolloid und Grenzflächenforschung

Biomass Derived Carbon for New Energy Storage Technologies

Dissertation
zur Erlangung des akademischen Grades
"doctor rerum naturalium"
(Dr. rer. nat.)
in der Wissenschaftsdisziplin "Physikalische Chemie"

eingereicht an der
Mathematisch-Naturwissenschaftlichen Fakultät
der Universität Potsdam

von
Florian Schipper

Geboren am 08 Juli 1985

Potsdam, 29 April 2014

EIDESSTATTLICHE ERKLÄRUNG / STATUTORY DECLARATION

“Hiermit erklaere ich an Eides statt, dass ich die vorliegende Dissertation selbstaendig und ohne Hilfe verfasst, keine anderen als die angegebenen Quellen und Hilfsmittel benutzt und woertlich oder inhaltlich entnommene Stellen als solche kenntlich gemacht habe.”

“I herewith formally declare that I myself have written the submitted dissertation independently. I did not use any outside support except for the quoted literature and all the other sources which I employed producing this academic work, either literally or in content.”

Potsdam, 29 April 2014

Florian Schipper

“An alleged scientific discovery has no merit
unless it can be explained to a barmaid.”

Ernest Rutherford

Acknowledgements

First and foremost I want to thank my supervisor professor Markus Antonietti for the opportunity to work in such a great scientific environment with such a great set of awesome people. I had a blast the last two and half years and learned something new every day.

I also want to give my deepest thanks to my group leader Dr. Tim Fellinger for being such a great person on a scientific and personal level. I learned a lot and not only about science and hopefully future projects will lead to repeated collaboration.

Robert Dominko and Andreas Taubert are highly acknowledged for agreeing to review this thesis. At the same time I want to tank Carolin Nuglish for proof reading the thesis in such short time, I know it was at very short notice.

Furthermore I want to give my thanks to all the members of the EUROLIS project and the European Commission for funding. A special thanks goes to Alen Vizinti for all the battery measurements (I have a bottle of Jaegermeister in store for you ;).

Laurent Chabanne and Guylhaine Clavel are thanked for the TGA and HRTEM/EELS test, respectively and of cause also for being such splendid co-workers and friends. I also want to thank the technician Regina, Heike, Rona, Sylvia, Jessica and Ursula for all the invaluable help with SEM, TEM, EA and ordering throughout my stay here.

Dr. Daniel Weingarth and Gerard Sans Palacios of the research group of Jun.-Prof. Dr. Volker Presser are thanked for all the SC measurements under neutral conditions and the fruitful discussions. I had a great time in Saarbruecken and hope to see you guys again in the future.

Further on I want thank all my office, lap mates and friends: Dasha, Nina, Debby, Christian, Ken-san, Karina, Vale, Guylhaine, Vince, Marco, Stefan, Steffie, Laurent, Giami, Alen, Roberto, Dana, Afroditi, Danuta, Kang Ko, Simon, Torsten and Marie for creating such a great environment here at the MPI and the countless evenings we spent out in Berlin. I also want to give my thanks to my longtime friends here in Berlin for their support.

Last but not least I want to thank my family for their constant support and understanding.

Table of Contents

A Introduction

B Hydrothermal Carbonization

C Ionothermal Carbonization of Biomass via a Salt Melt Approach

F Appendix

A Introduction

1 General Introduction and Motivation

Fig. 1 Replica of the Lohner-Porsche (GNU license)

The Exposition Universelle of 1900 in Paris held many breathtaking wonders in store for the over 50 million spectators. Not only could Rudolf Diesel present a combustion engine running on coconut oil but Ferdinand Porsche displayed one of the first electric vehicles (**EV**) ever created, the Lohner-Porsche (**Fig. 1**)[1, 2]. It seemed that mankind was on a good track into a green future, but with the commercialization of the electric starter in 1912, and the plummeting oil prices internal combustion engine became more popular and soon outperformed competitive systems[3]. Over the last 100 years humanity has grown more and more depended on fossil fuels as a convenient source for energy production, heat generation, and gasoline production (**Fig. 2 left**)[4].

The ever increasing demand for more electrical energy leads to a rapid depletion of natural resources, especially oil and gas. The economic growth of developing countries (e.g. China and India) in combination with an expected growth of the global population by 30% over the next 25 years leads to an estimated depletion of oil, gas, and coal within the next 35, 37, and 107 years, respectively[5]. Furthermore are those resources not evenly distributed and a small number of countries hold the majority of the oil and gas reserves (**Fig. 2 right**)[5]. This may lead to more dangerous endeavors to

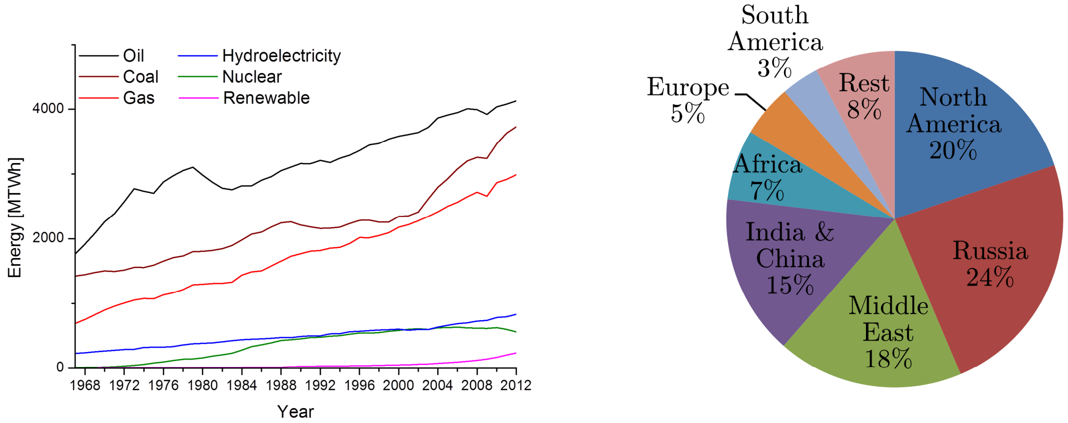

Fig. 2 Left: Energy consumption by resource from 1967 to 2012 worldwide in MTWh
Right: Distribution of fossil fuel reserves

exploit new fossil fuel reservoirs and could lead to a repetition of events like the Deepwater Horizon incident[6].

With the start of the industrialization in the middle of the 18th century, the human impact on nature was more intense than ever before. The carbon dioxide emission increased from 1850 to 2008 to a total value of about 32 Gt annually (**Fig. 3**)[7]. With CO_2 being the most prominent greenhouse gas (84%) next to methane (9%) and nitrous gases (5%), a cut down in CO_2 emission is believed to have a tremendous effect on global warming[8]. Most countries undergo efforts to cut their CO_2 emission by changing to renewable resources for energy production like solar, wind, and water power. Since hydroelectricity is not an option for every location, solar and wind power are very attractive for a general approach towards a green energy production. A major shortcoming of the two is the uneven energy supply which can change significantly over the course of a day. A viable option to overcome this problem is to store energy into an intermediate form and release it on demand rather than just producing a constant amount which might not be needed[9]. There are various options to store energy on side e.g. flywheels[10], pumped-storage hydroelectricity[11], compressed air[12], or batteries[13]. So far, pumped-storage is the largest form of grid energy storage but with the advent of lithium-ion batteries (**LIB**), batteries have become a viable option[14]. State of the art LIB have a specific energy of about 150 Wh kg^{-1}[13] and an increase is desirable not only for consumer electronics but also for grid energy storage.

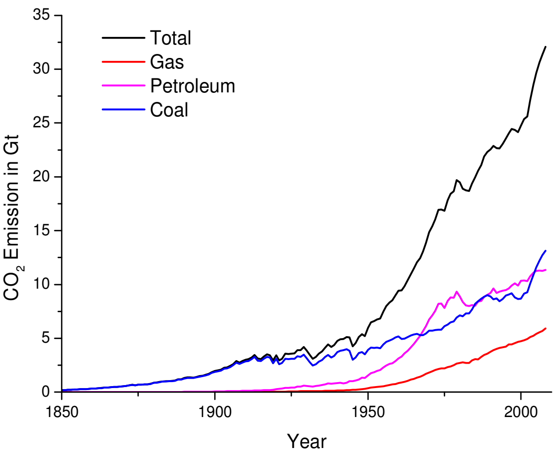

Fig. 3 CO_2 Emission in Gt per year from 1850 to 2008

Set aside from renewable energy production, the development of EV and hybrid electric vehicles (**HEV**) has become once more the focus of various car manufactures[15]. Since the automotive sector is accounting for 20%[16] of the total annual CO_2 emission, a change to electrical powered cars gives the opportunity for a big reduction in greenhouse gas generation. Currently, two options are under pursuit to power EV, one being fuel cells the other being batteries[17, 18]. Where the first usually suffers from extensive cost and the issue of hydrogen storage the latter suffers from limitation in driving distance. State of the art battery EV show a driving distance of ca. 150 km[19], which is enough for commuter traffic but might not appeal to a broad audience. Once again an increase in specific energy density is a key factor.

Apart from the energy production, the chemical industry is highly depending on oil for the production of basic chemicals which in turn are the building blocks for almost every chemical product e.g. dyes, plastics, and drugs. Currently about 7% of the annual oil consumption is attributed to the chemical industry and a possible oil shortage would have severe ramifications on day to day life. Sustainability should not be limited to the energy and transportation market but must include the chemical industry as well. In this regard carbon has become an attractive material in different research fields for various applications such as batteries[20], supercapacitors (SC)[21], capacitive deionization (CDI)[22], water splitting[23], etc. The production of biomass via CO_2, water and sunlight is part of the natural carbon cycle where fouling produces CO_2 and growth consumes CO_2. If biomass is taken from this cycle to produce carbon materials, the process can be considered CO_2 negative, thus acting as a carbon sink. This offers an effective way to reduce the overall carbon dioxide concentration in the atmosphere and gain valuable products *en passant*.

The thesis at hand deals with the development of functional porous carbons from biomass and their application in energy storage devices such as SC and lithium sulfur batteries (LSB). Two different synthesis approaches will be investigated: a hydrothermal carbonization (HTC), catalyzed by borax with a subsequent CO_2 activation, and an ionothermal carbonization, salt melt assisted, synthesis.

2 Porous Functional Carbons

Carbon has been known to mankind in its natural occurring allotropes (diamond and graphite) since ancient times[24]. Where diamond shows a sp^3 hybridization and is nonconductive graphite consists of a sp^2 hybridized conductive carbon network[25]. Recently, the carbon family has been extended by additional synthesized allotropes e.g. fullerenes[26], carbon nanotubes[27], and graphene[28] (**Fig. 4**). If the carbon material under questions does not show any ordering it is usually referred to as amorphous carbon and shows a mixture of sp^2 and sp^3 hybridization with hetero atoms inside the carbon lattice[29].

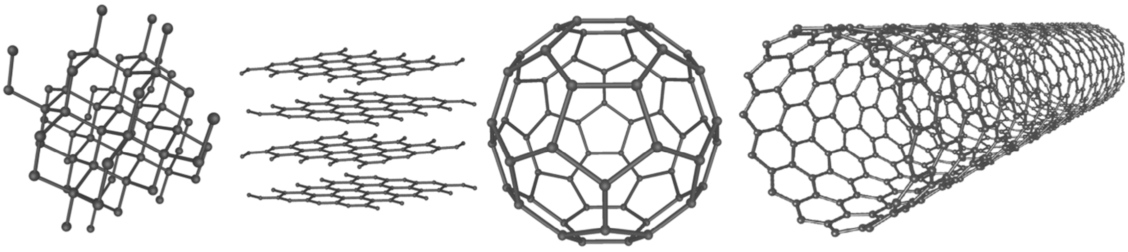

Fig. 4 Different carbon allotropes: diamond, graphite, C_{60} fullerene, carbon nano tube (from left to right; GNU license)

Amorphous carbons are especially interesting since they are usually easy to make and can be tuned to meet the demands of different applications. They have been synthesized from biomass[30], ionic liquids[31], and polymers[32]. Some important properties of amorphous carbons are electrical conductivity, high and tunable surface area, and surface functionalities due to hetero atoms (e.g. amino or keto functions)[33].

Electrical conductivity is very important for electrochemical applications, especially SC where a high conductivity is necessary to support high currents, thus allowing for a high power output. In order to introduce conductivity, usually temperatures in the range of 800 °C up to 3000 °C are chosen to decrease the amount of oxygen atoms and increase the degree of order in the carbon lattice[34].

A high surface area is important for a magnitude of applications but often a distinct porosity is necessary to account for better diffusion rates in electrochemical systems. Surface area can easily be generated by chemical or physical activation with KOH or CO_2 or by template assisted approaches (e.g. silica templates)[35-37]. The first two create surface area at the expense of carbon material and the latter uses a scaffold which has to be removed afterwards. Silica is a very well-studied and often employed template and can be used as nano spheres or more complex structures like SBA-15 (Santa Barbara Amorphous)[38] or MCM-41 (Mobile Crystalline Materials)[39]. A major drawback of silica templates is the scaffold removal in hydrofluoric acid. Apart from the use of very toxic HF, an additional step is necessary to generate the final carbon product[40]. Recently, a more elegant template procedure has been developed by Antonietti *et. al.* Eutectic salt mixtures e.g. LiCl/ZnCl, KCl/ZnCl, were used as a porogen during an iono-thermal synthesis of amorphous carbons[41]. Since the employed ionic liquids are carbonized at temperatures higher than the melting point of the eutectic mixtures, a phase separation will occur creating a porous carbon structure trapping salt cluster inside the carbon matrix. And with the salt removal porous, high surface carbons are obtained. In stark contrast to a silica template, the remaining salt can easily be removed in water avoiding any harsh conditions.

The introduction of heteroatoms is a common tool in the carbon community to achieve different properties of amorphous carbons. Nitrogen is the most prominent dopant used in carbon synthesis. It can be introduced by simply choosing a nitrogen rich carbon precursor (glucosamine[42], chitin[43]), by in situ reactions with nitrogen compounds (amino acids[44], ammonium sulfate[45], ammonia solution[46]) or by post treatment of the carbon material in an ammonia atmosphere at elevated temperature[47]. Nitrogen can be located within the bulk carbon replacing oxygen and thus increasing the conductivity and decreasing the distortion of the overall framework. Furthermore, surface functionalities of different nitrogen states can be found (**Fig. 5**)[33]. Nitrogen functions located at the surface can act as a catalyst in the oxygen reduction reaction or provide an additional faradaic current in so called pseudocapacitors[48].

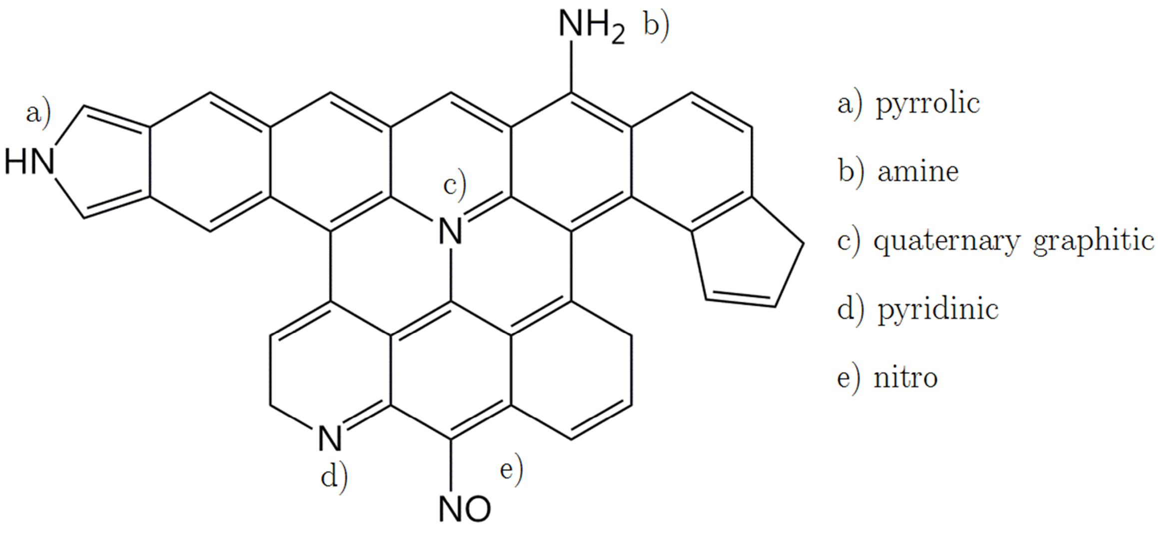

Fig. 5 Possible structure of nitrogen doped carbon

3 Supercapacitors

3.1 Introduction and State of the Art

The earliest design of a capacitor was independently developed by Ewald Georg von Kleist and Pieter van Musschenbroek of Leiden in 1745[49]. They used a glass jar, coated with metal on the inside and outside, filled with water. The device could store energy generated by friction and was essential for early electrical experiments[49]. It was soon proven by Benjamin Franklin that the charge is stored by the metals contrary to the common believe that the water was the charge carrier[50]. The so called Leyden jar (**Fig. 6**) was used for various experiments and helped scientist to unravel the fundamentals of capacitors. The capacitor family has been extended over the years by ceramic, film, and electrolytic capacitors[51].

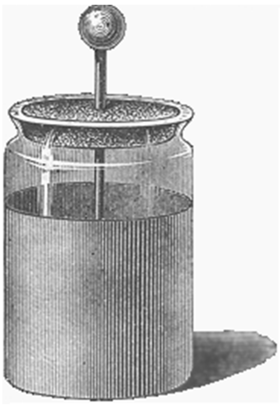

Fig. 6 Drawing of the Leyden jar (GNU license)

After the invention of electrolytic capacitors in 1896[52], the principle of charge storage in the electric double layer between a solid and the electrolyte was born. Since the energy stored in a capacitor is proportional to the surface area, the use of high surface area materials (e.g. activated carbon) should result in a considerable increase of stored energy. It was in the 1950s, when H.I. Becker conducted the first research on carbon based capacitors which were later named **e**lectric **d**ouble **l**ayer **c**apacitors (**EDLC**)[49]. The work of Becker was followed by numerous publications (**Fig. 7**) helping to understand the storage mechanism in this new type of capacitor. After the commercialization by the NEC cooperation in 1978[49], the marketing term supercapacitor was coined for this type of capacitor. They were initially used as backup power supply for **c**omplementary-**m**etal-**o**xide-**s**emiconductor (**CMOS**) computer memories[49].

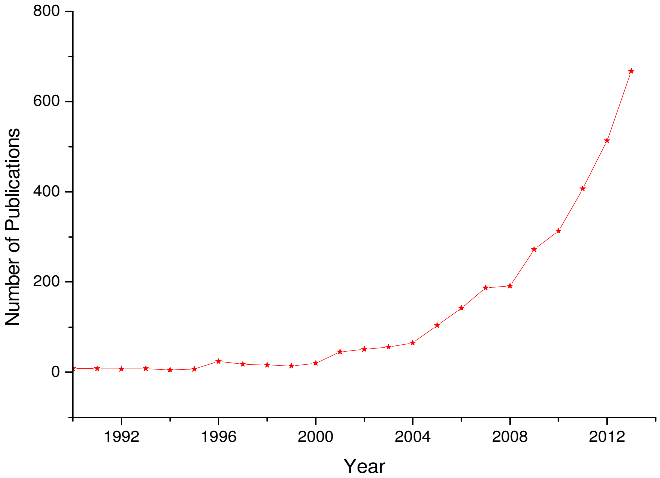

Fig. 7 Number of publications on supercapacitors from 1990 to 2013 (Source: Web of Science)

Current research on SC is devoted to increase the energy density by maintaining its outstanding power density. Graphene has attracted much attention due to its superior conductivity and theoretical surface area of 2630 m^2 g^{-1}[53] and high specific capacitances were reported[54]. Other carbon materials like carbide derived carbons (**CDC**)[55], CNT[56] or carbon aerogels[57] are also under intense scrutiny as electrode material in SC.

Since the energy density of a capacitor is proportional to the square of the voltage and thus limited by the stability window of the electrolyte (ca. 1.2 V[48] for aqueous solutions), organic solutions are often used as an alternative (ca. 2.5 V[58]). Recently ionic liquids (**IL**) have gained much attention as an electrolyte in SC because they offer a voltage window of up to 3.5 V[59] and no additional salts have to be used. Furthermore, are IL nontoxic and nonvolatile making them an ideal choice for future SC[60].

The combination of high surface area carbons with lithium ion battery to a hybrid capacitor (sometimes called lithium ion capacitor) is another elegant option to increase the working voltage to 3.0 V[61]. In that case, the anode will be the battery material and the cathode is consisting of the activate carbon. Since lithium ions are intercalating into the host matrix much more charge can be accumulated in the anode compared to the double layer of the cathode. Therefore, the anode can be designed much smaller than the cathode which results in energy densities of about 14 Wh kg^{-1}[62] without sacrificing power density. Anode materials are usually graphitic carbons[63] or 3D-intercalation compounds like lithium titanate ($Li_4Ti_5O_{12}$)[64].

Another simple way to increase the energy density of SC is offered by so called pseudocapacitors which exploit fast faradaic reactions in addition to the surface charge of SC. Different metal oxides are known to give rise to high pseudocapacitance, e.g. NiO[65], RuO_2[66] and MnO_2[67]. A simple and yet effective way to introduce pseudocapacitance is the doping of carbons with hetero atoms like oxygen, sulfur, or nitrogen[34]. This approach is also advantageous concerning the price and safety of future SC because hetero atoms can be easily introduced and benign precursors can be used.

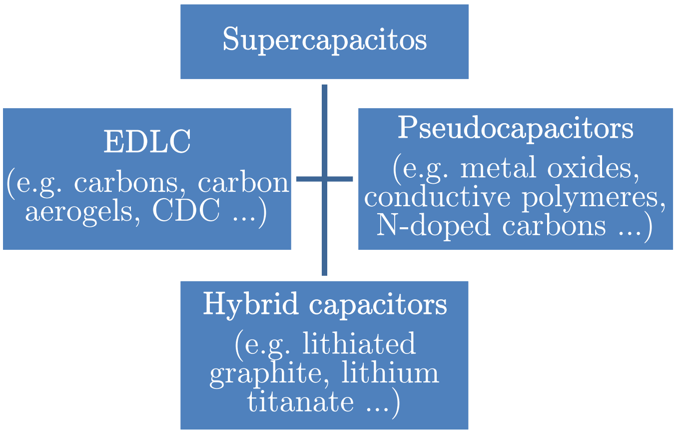

Fig. 8 Schematic of different supercapacitors

Fig. 8 gives an overview of the SC family. In general, an overlay between EDLC and pseudocapacitors is always present since a charged surface will always show a double layer. Therefore, the stored charge of pseudocapacitors can be enhanced by employing high surface area materials.

Nowadays, supercapacitors are regarded as a vital energy storage system and state of the art devices show energy densities of up to 10 Wh kg^{-1}[68]. A major advantage over battery systems are the very short charge time, the long cycle life (> 500,000 cycles), and the low price due to inexpensive carbon materials[69]. This has prompted much interest in SC for various applications, today's usage of supercapacitors has emancipated from its early niche applications. Supercapacitors can be found in digital cameras and cell phones were their high power density is ideally suited to power the flash light or smoothen the high power demand during high current operations (e.g. writing of data)[70]. Furthermore, are SC believed to play a decisive role in the development of EV and HEV. The combination of SC with fuel cells is very attractive for EV where the SC could circumvent for the low power density of fuel cells and break energy can be regained[71]. The concept of recuperation of breaking energy is already successfully used in diesel locomotives and HEV busses and energy savings of around 25% are reported (**Fig. 9**)[72-74]. The SC field has grown into a market worth 500 million Euro (2012) with an expected growth to a multi-billion Euro market by 2020[75].

Fig. 9 EV Bus (capabus) currently tested in Shanghai; large onboard supercapacitors are used as power source; SCs are charged at bus stops and by break energy recuperation (GNU license)

3.2 Fundamentals

3.2.1 Double Layer Model and Energy of SC

A supercapacitor consists of two high surface area carbon electrodes, an electrolyte, and a separator acting as a spacer (**Fig. 10 left**). If a direct voltage is applied to the electrodes, they will be charged as cathode and anode and ions from the electrolyte will compensate the corresponding charge. The energy is thus stored via charge separation of ions at the surface of the electrodes. The phenomenon of surface charge compensation by oppositely charge ions is described by the Stern model (**Fig. 10 right**). It states that solvated ions have a finite size and will move as close to the surface as their own volume allows. This static bilayer is called the Stern layer and is followed by a diffuse layer in which the counter ions are diffusely distributed with higher densities closer to the charged surface. This results in an overall potential curve as shown in **Fig. 10 right** where a linear decrease in the stern layer is followed by an asymptotic decrease in the diffuse layer. Each electrode of the SC shows a double layer and a full cell consists essentially of two capacitors in series. This means that the total capacitance C of a SC can be described by:

$$\frac{1}{C} = \frac{1}{C_{anode}} + \frac{1}{C_{cathode}} \qquad \text{Eq.(1)}$$

If the capacitor is symmetrical the capacitance at the anode and cathode will be equal, hence the capacitance of a single electrode is twice the total capacitance.

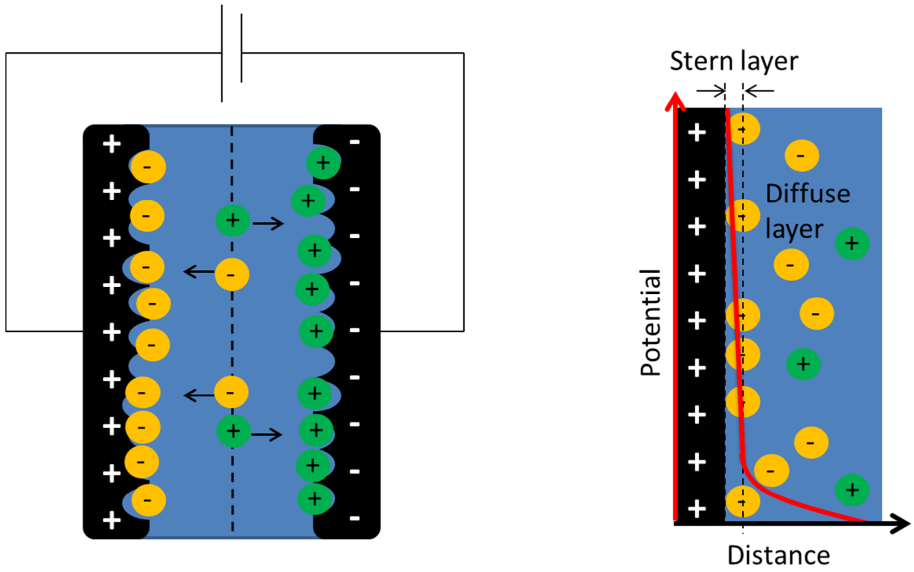

Fig. 10 Left: Schematic representation of a supercapacitor during charge
Right: Stern model of the electric double layer

The amount of charge Q stored in a capacitor is expressed by the capacitance and the voltage U as follows:

$$Q = C \cdot U \qquad \text{Eq.(2)}$$

The capacitance is proportional to the surface area of the plates A, given by the equation:

$$C = \varepsilon_0 \cdot \varepsilon_r \cdot \frac{A}{d} \qquad \text{Eq.(3)}$$

with ε_0, ε_r and d being the vacuum permittivity, permittivity of the electrolyte and the distance between the ions and the surface (thickness of the double layer). From Eq.(3) it is evident that a high surface area carbon should give a high capacitance. In fact a activated carbon with 1000 m^2 g^{-1} should give a specific capacitance of about 1400 F g^{-1} a value which is unrealistically high for an accumulation of surface charge (d: 0.5 nm, ε_0: $8.85 \cdot 10^{-}12$ As V^{-1} m^{-1}, ε_r: 80). This shows that the mechanism of charge storage must be more complex and that the electrochemical active surface area might be smaller than the surface area determined by nitrogen sorption. It was also suggested that the values for ε_r measured on a macroscopic scale might not be the same as in a micro porous carbon material and could be much smaller, nonetheless the storage mechanism is not fully understood[76].

The model used to derive Eq.(3) is based on a plate capacitor with a planar surface area which is a significant deviation from a porous carbon material. Especially micro porous carbons with an average pore size in the range of solvated electrolyte ions or even smaller pores are not applicable to this model. Gogotsi and coworker studied the correlation between capacitance and surface area and especially the pore size of different carbon materials[77]. They used CDCs since they allow a very precise control over pore sizes depending on the chlorination temperature and the used carbide[78]. Their work contradicted the common believe that higher pore sizes are favorable in terms of specific capacitance. Interestingly, the correlation between capacitance and pore size was linear for pores > 2 nm but showed an immense increase for micro pores < 2 nm (**Fig. 11**). The studies of Gogotsi *et. al.* and those of other research groups were later used by Huang *et. al.* to derive a more suitable model for porous carbon materials[79]. They divided the specific capacitance into two regimes with an equation for meso- and microporous carbons:

$$C(meso) = \frac{\varepsilon_0 \cdot \varepsilon_r \cdot A}{b \cdot \ln(b/(b-d))} \qquad \text{Eq.(4)}$$

$$C(micro) = \frac{\varepsilon_0 \cdot \varepsilon_r \cdot A}{b \cdot \ln(b/a_0)} \qquad \text{Eq.(5)}$$

with a_0 being the non-solvated ion radius and b the pore size. Taking the values into account as before and assuming a pore size of 2 nm the specific capacitance would yield 120 F g^{-1} (a_0: 115 pm[80])[1]. Furthermore, the anomalous increase in capacitance for microporous carbons was addressed by Huang[79]. He suggested a deformation or even stripping of the solvation shell to explain the higher capacitance for pores smaller than the size of the solvated electrolyte ions.

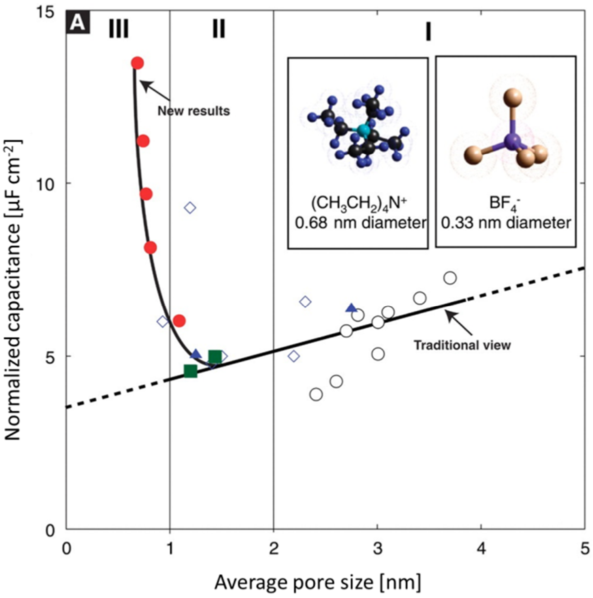

Fig. 11 Correlation between pore size and capacitance for porous carbon materials; adapted from [77]

The electrical energy E of a capacitor is given by the integral of voltage and current I over time t and can be expressed with Eq.(2) as follows:

$$dE = \int U(t) \cdot I(t) \cdot dt \quad \text{with} \quad dQ = I(t) \cdot dt$$

$$dE = \int U(t) \cdot dQ = \frac{1}{C} \int Q \cdot dQ$$

$$E = \frac{1}{2} \cdot \frac{1}{C} \cdot Q^2 = \frac{1}{2} \cdot C \cdot U^2 \qquad \text{Eq.(6)}$$

This shows that an increase in voltage has a great impact on the overall energy of a capacitor and high voltage electrolytes are favorable. The power P of the SC can be derived from the energy with the discharge time t_{dc}:

$$P = \frac{E}{t_{dc}} \qquad \text{Eq.(7)}$$

---

[1] The model was developed for organic electrolytes, based on ammonium salts dissolved in acetonitrile, and might not be entirely accurate for aqueous electrolytes.

3.2.2 Cyclic Voltammetry Response of SC

The Cyclic voltammetry (**CV**) measurement is a common test to determine the performance of a SC. The CV experiment applies a triangular voltage to the device and the current response is measured (**Fig. 12 left**). The voltage is swept between an upper and lower limit which is usually the stability window of the corresponding electrolyte. The scan rate v is basically the derivation of voltage over time (dU/dt) which gives with Eq.(2):

$$\frac{dQ}{dt} = I = C \cdot v \qquad \text{Eq.(8)}$$

An ideal SC should therefore give a rectangular current response (**Fig. 12 right**). Since the electrolyte and the active material have a finite conductivity it causes a resistance inside the SC, the so called electrical series resistance (**ESR**)[1]. The ESR leads to a shifted current curve. A real capacitor shows a behavior somewhere in-between but a trend closer to the ideal case is favorable and speaks for a low ESR and fast ion diffusion inside the pores.

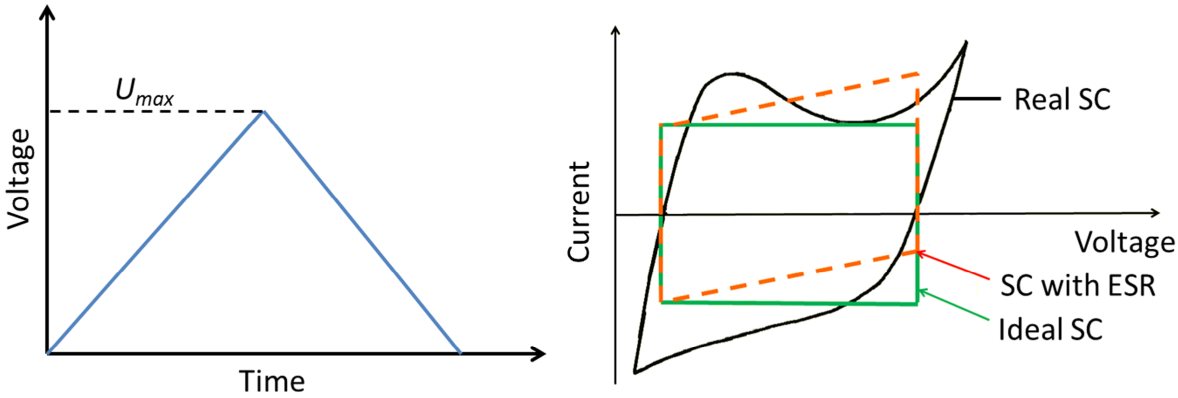

Fig. 12 Left: Presentation of the voltage over time in a CV experiment
Right: Current response in a CV experiment

The specific capacitance C_{sp} can be calculated from the CV as follows:

$$C_{sp} = 2\frac{I}{v \cdot m_e} \qquad \text{Eq.(9)}$$

---

[1] Also other factors can play a role in the ESR (contact resistance, conductivity of current collectors etc.) but their contribution is negligible for SCs.

where v is the scan rate, m_e is the active mass of one electrode and the factor which adjusts for the two electrode measurement. Since the current is not constant in a CV measurement of a real SC, the mean value theorem of the integration is used to extend Eq.(9) to:

$$C = 2\frac{\int IdU}{\Delta U \cdot v \cdot m_e} \qquad \text{Eq.(10)}$$

with ΔU being the applied voltage window.

In case of a constant capacitance, a representation of C over v should ideally give a horizontal line but usually an asymptotic behavior is found (**Fig. 13 left**). With higher scan rates the accessibility of pores by ions becomes sluggish since the time frame is not enough and bottle-neck effects might occur. In addition, the conductivity of the active material plays an important role at higher scan rates. A highly conductive material can support high currents. This will result in a deviation of the CV response with increasing scan rates (**Fig. 13 right**), depending on the pore size and conductivity, the deviation from an ideal behavior can be more or less prominent.

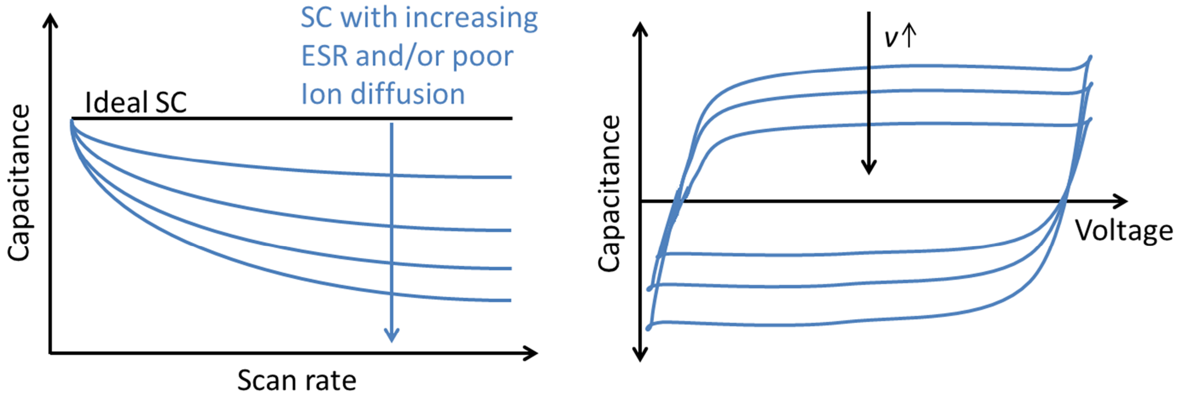

Fig. 13 Left: Capacitance vs. scan rate for an ideal (black) and real SC (blue)
Right: CV response for a real SC with increasing scan rate

3.2.3 Constant Current Behavior of SC

The constant current (CC) experiment is used as a close resemblance to an actual use of a SC. The SC is charged and discharged with a constant current of the same magnitude to a cut-off voltage. Therefore Eq.(2) can be written as:

$$I \cdot t = U \cdot C \qquad \text{Eq.(11)}$$

The voltage will provide a liner curve with a slope given by current over capacitance (I/C). A high capacitance will therefore result in a longer charge/discharge time (**Fig. 14**). The capacitance can either be calculated from the slope or better from the total amount of charge since the slope is not necessarily constant over the whole range. The specific capacitance from a CC measurement using the discharge time t_{dc}, is given by:

$$C_{sp} = 2\frac{I \cdot t_{dc}}{U \cdot m_e} \qquad \text{Eq.(12)}$$

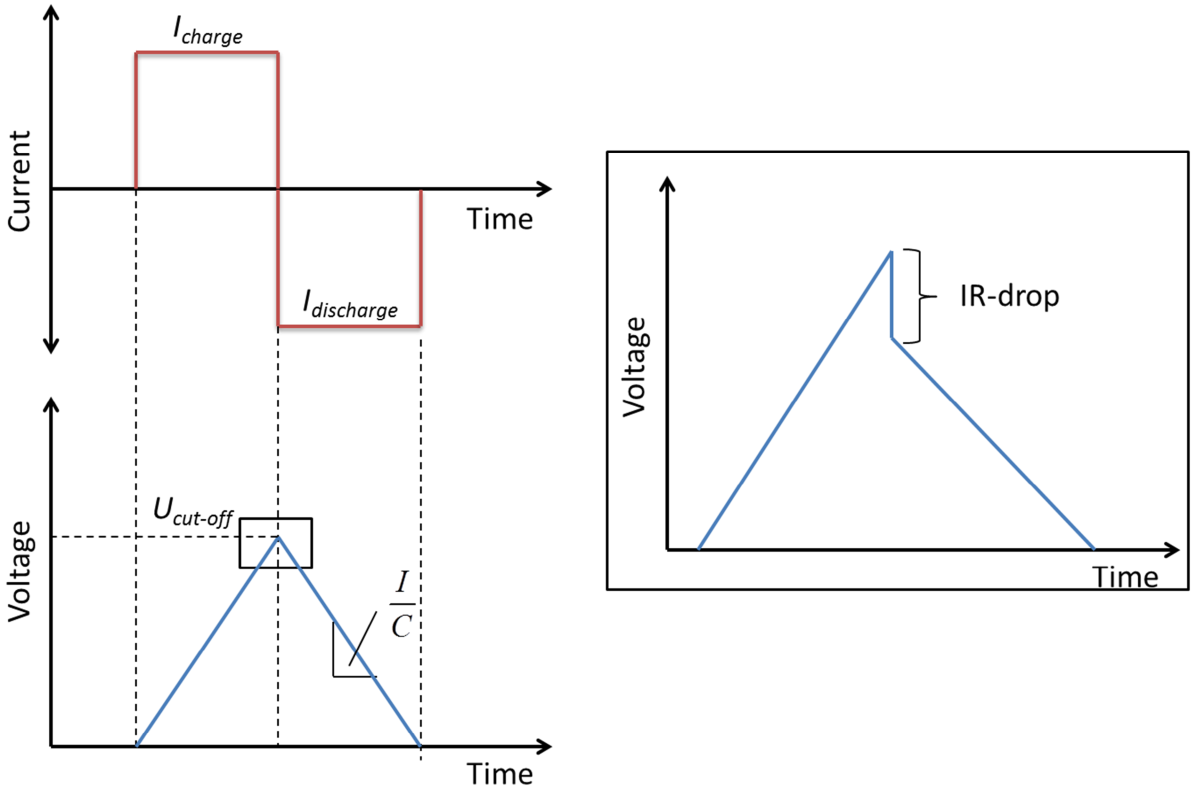

Fig. 14 Schematic representation of the CC measurement (inset is showing the voltage drop)

The CC experiment also offers an elegant way to determine the ESR value of a SC device (inset **Fig. 14**). At the turning point from charge to discharge the voltage will drop according to:

$$U_{\mathrm{drop}} = \left(I_{\mathrm{charge}} + \left|I_{\mathrm{discharge}}\right|\right) \cdot ESR \qquad \text{Eq.(13)}$$

Since I is constant, the height of the IR drop is proportional to the ESR. The IR drop is negligible for small currents. But if the SC is run at high current densities, for high power outputs, the voltage drop will be the limiting factor. For accurate capacitance values, the voltage in Eq.(12) must be taken after the IR drop. The ESR will cause a power loss during discharge which will result in heat generation:

$$P_{\mathrm{loss}} = U_{\mathrm{drop}} \cdot I = ESR \cdot I^2 \qquad \text{Eq.(14)}$$

Furthermore, the maximum power of a capacitor is limited by the ESR value, with $P = U \cdot I$ and $U = U_{\mathrm{max}} - ESR \cdot I$ the power can be written as:

$$P = I \cdot U_{\mathrm{max}} - ESR \cdot I^2 \qquad \text{Eq.(15)}$$

The maximum power P_{max} will be reached for the case $dP/dI = 0$

$$\frac{dP}{dI} = U_{\mathrm{max}} - 2ESR \cdot I = 0 \qquad \text{Eq.(16)}$$

The combination of the Equation Eq.(15) and Eq.(16) gives P_{max} with:

$$P_{\mathrm{max}} = \frac{U_{\mathrm{max}}^2}{4 \cdot ESR} \qquad \text{Eq.(17)}$$

This demonstrates the importance of the ESR in a SC. The ESR value of different materials can be compared given that the same system and electrolyte is used. In that case, the contribution of the electrolyte will be constant and the properties of the material will be the determining factor.

3.2.4 Alternating Voltage Response of SC

Electrical impedance spectroscopy (**EIS**) is used to gain detailed information about a sample. An alternating voltage (AV) is applied to the sample and the alternating current (AC) response is measured (**Fig. 15**). The AV amplitude is usually in the range of 10 mV in order to measure at a steady state and the frequency can range from a few mHz up to some MHz. The AV signal can be written as:

$$U(t) = U_0 \cdot e^{j\cdot(\omega\cdot t+\varphi_U)} \quad with \;\; j^2 = -1 \qquad \text{Eq.(18)}$$

with the voltage amplitude U_0, the phase angle φ_U and the angular frequency ω (given by $2\pi f$ with the frequency f). The AC response will be:

$$I(t) = I_0 \cdot e^{j\cdot(\omega\cdot t+\varphi_I)} \qquad \text{Eq.(19)}$$

The impedance Z can be understood as a frequency depended resistance and is expressed by Ohms law together with Eq.(18) and Eq.(19) as follows:

$$Z(\omega) = \frac{U(t)}{I(t)} = \frac{U_0}{I_0} \cdot \frac{e^{j\cdot(\omega\cdot t+\varphi_U)}}{e^{j\cdot(\omega\cdot t+\varphi_I)}} = Z_0 \cdot e^{j(\varphi_U-\varphi_I)} = Z_0 \cdot e^{j\varphi} \qquad \text{Eq.(20)}$$

with Z_0 being the magnitude and φ being the phase shift between the AV input and the AC response.

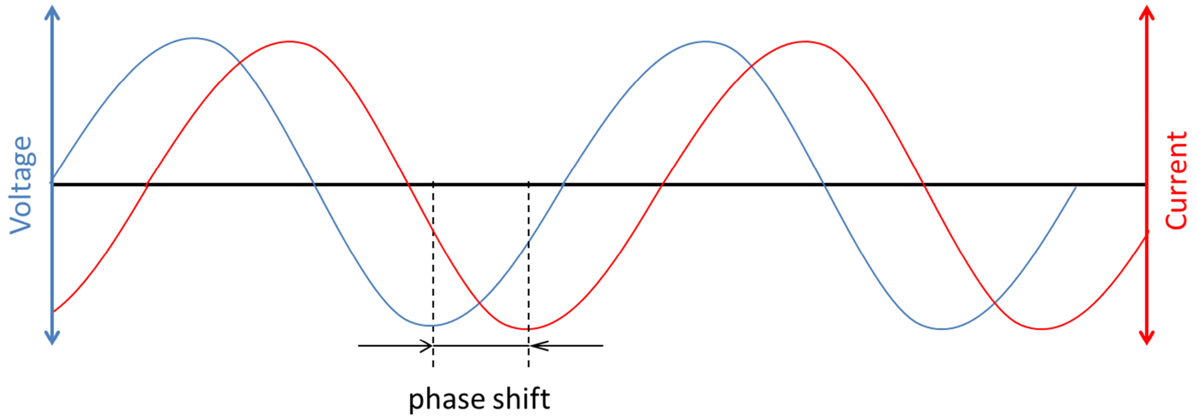

Fig. 15 Sinusoidal AV input and AC response during an EIS experiment

Using the Euler relation, $e^{j\cdot\varphi} = \cos(\varphi) + j\cdot\sin(\varphi)$, Eq.(20) can be separated into the real *Z'* and imaginary *Z''* part:

$$Z(\omega) = \frac{U(t)}{I(t)} = Z_0\cdot\cos(\varphi) + Z_0\cdot j\cdot\sin(\varphi) = Z'(\omega) + j\cdot Z''(\omega) \qquad \text{Eq.(21)}$$

By measuring the current amplitude and the phase shift, both values *Z'* and *Z''* can be accessed.

The representation of *Z* in the complex plane is called Nyquist plot. An ideal resistor with no frequency dependence would be a single point on the real axis. The current of a capacitor can be expressed as $dQ/dt = I = C\cdot dU/dt$ which leads together with Eq.(18) to the following impedance:

$$Z(\omega) = \frac{U(t)}{I(t)} = \frac{U_0\cdot e^{j\cdot(\omega\cdot t+\varphi_U)}}{j\cdot\omega\cdot C\cdot U_0\cdot e^{j\cdot(\omega\cdot t+\varphi_U)}} = \frac{1}{j\cdot\omega\cdot C} \qquad \text{Eq.(22)}$$

The EIS offers an additional way to determine the capacitance. For an ideal capacitor, the phase shift is 90 °, and a vertical line is observed in the Nyquist plot. In combination with a resistor, the line is shifted by the value of the resistor (**Fig. 16 left**). The corresponding equivalent circuit would be a resistor and a capacitor in series. For a supercapacitor a more complex behavior is usually observed with a time constant (semicircle) and a Warburg Impedance (45 ° regime) expressed by the Randles circuit (**Fig. 16 right**)[81].

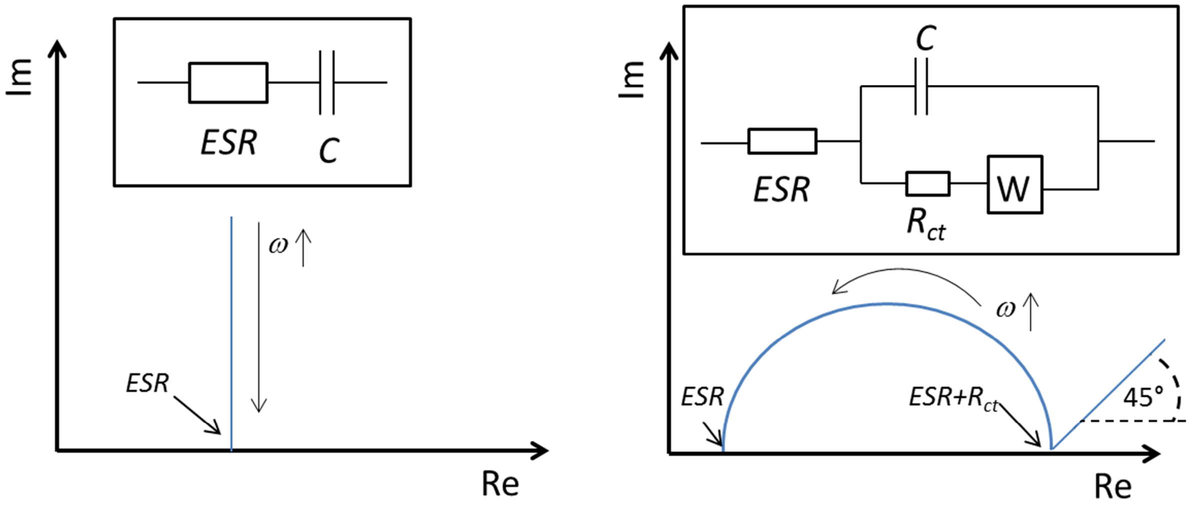

Fig. 16 Left: Nyquist plot and equivalent circuit of a capacitor in series with an ESR
Right: Nyquist plot and equivalent circuit of a Randles circuit with Warburg impedance *W* and charge transfer resistance R_{ct}

The charge transfer resistance can originate from a contact resistance between the active material and the current collector or from a faradaic process (pseudocapacitance) where R_{ct} would translate into the exchange current density of the Tafel plot[81]. In general, a distinction between the double layer capacitance and pseudocapacitance of a porous carbon material is usually not possible.

The Warburg Impedance describes the ion diffusion to a large planar electrode. This is obvious not the case for highly porous carbon electrodes. A more comprehensive model was developed by de Levie[82] and later extended by Keiser[83]. The pores of the activated carbon can be simplified as a parallel connection of capacitors with a pore resistance R_p in series (**Fig. 17**).

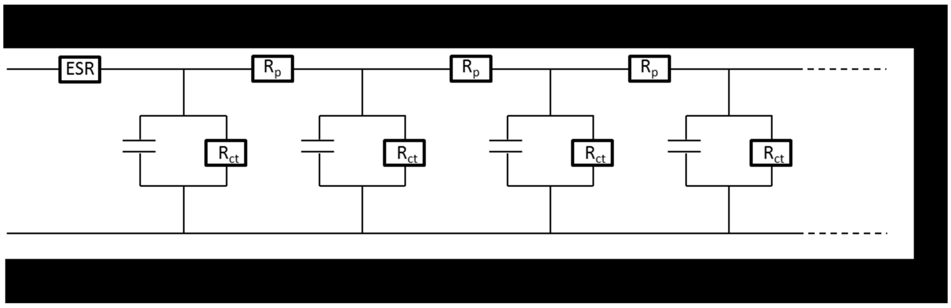

Fig. 17 Ladder model of one pore with multiple time domains (RC elements) and pore resistance *Rp* adapted from [82]

The impedance of one pore is according to de Levie[82]:

$$Z_p = \sqrt{R_p Z_E} \coth\left(l \sqrt{\frac{R_p}{Z_E}} \right) \qquad \text{Eq.(23)}$$

with the electrode/electrolyte interface impedance Z_E and the length of the pore *l*. And with n pores in parallel:

$$Z_n = \frac{Z_p}{n} \qquad \text{Eq.(24)}$$

The corresponding equivalent circuit of a porous electrode is given in **Fig. 18 left**. The Nyquist plot of a real supercapacitor is composed of a time constant and pore diffusion (**Fig. 18 left**). Approaching lower frequencies a transition from a 45 ° angle to a 90 ° angle can be seen. This means that the ion diffusion into the pores is better at lower frequencies. The transition frequency is called knee frequency f_{knee} and can be understood as a threshold value. Two cases can be distinguished[84]:

(1) $f > f_{knee}$; less than 50% of the total capacitance is reached

(2) $f < f_{knee}$; more than 50% of the total capacitance is achieved

Since the total capacitance in an EIS experiment is only reached for very low frequencies (< 1 mHz) the measured knee frequency in an actual test is often not at 50% of the observed capacitance.

The knowledge of the knee frequency of a particular material is very important since it offers a simple way to determine the high power capability of a supercapacitor. The discharge energy efficiency is 50% at f_{knee}. The energy loss is dissipated as heat. Hence, the higher the knee frequency the more the material is suited for high power applications.

A convenient way to determine f_{knee} is given by the complex representation of the capacitance. With Eq.(21) and Eq.(22) the capacitance can be divided into a real C' and imaginary C'' capacitance:

$$Z'(\omega) + j \cdot Z''(\omega) = \frac{1}{j \cdot \omega \cdot C}$$

$$C(\omega) = \frac{1}{\omega \cdot \left(j \cdot Z'(\omega) - Z''(\omega)\right)} = -\frac{j \cdot Z'(\omega) + Z''(\omega)}{\omega \cdot Z_0^2}$$

$$C(\omega) = -\frac{Z''(\omega)}{\omega \cdot Z_0^2} + \frac{Z'(\omega)}{j \cdot \omega \cdot Z_0^2} = C'(\omega) + j \cdot C''(\omega) \qquad \text{Eq.(25)}$$

The above equation shows a maximum for C'' at f_{knee} (**Fig. 18 right**).By the translation of the frequency into the corresponding time, the relaxation time constant τ_0, a more comprehensive representation is given:

$$\tau_0 = \frac{1}{f_{knee}} \qquad \text{Eq.(26)}$$

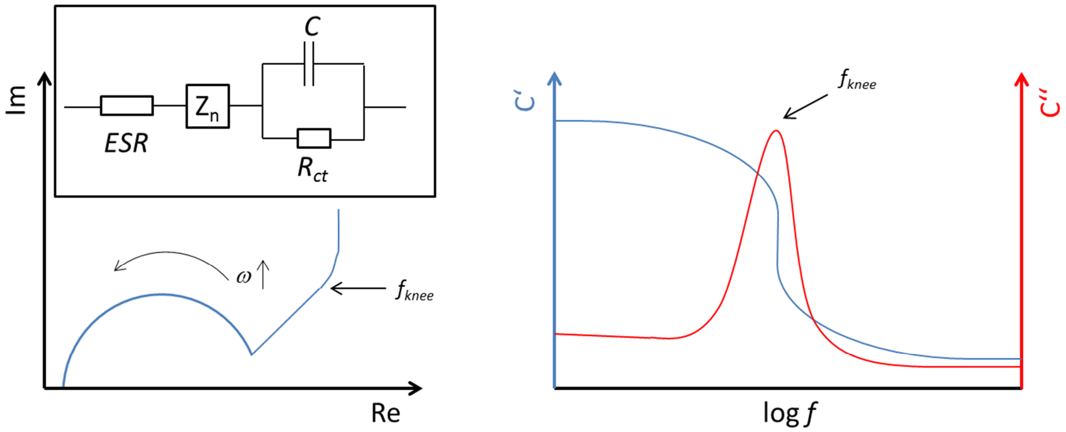

Fig. 18 Left: Nyquist plot and equivalent circuit of a porous carbon supercapacitor
Right: Evolution of C' and C" with C" maximum at C'/2

3.2.5 Test Cells for Supercapacitor Measurements

3.2.5.1 Two Electrode Cells

All two electrode SC tests throughout this thesis, in sulfuric acid, have been done using a Swagelok type cell (**Fig. 19**). The carbon samples were ball milled and mixed with a dispersion of polyvinylidene fluoride (**PvdF**) in acetone to yield a ratio of 95% carbon to 5% of PvdF binder. The dispersion was drop-casted onto platinum discs of 1 cm in diameter serving as a current collector. Two carbon coated discs were sandwiched between a filter paper separator infiltrated with 1 M sulfuric acid electrolyte. The operating voltage window was 1 V.

For the high voltage test the room temperature ionic liquid 1-ethyl-3-methylimidazolium tetrafluoroborate ([EMIM][BF_4]) was chosen due to its reasonable high conductivity (11.5 S cm^{-1}) and good electrochemical stability[85]. In order to avoid a possible oxidation of platinum during cycling, aluminum was chosen as a current collector for the tests in [EMIM][BF_4]. The operating voltage window was 3 V.

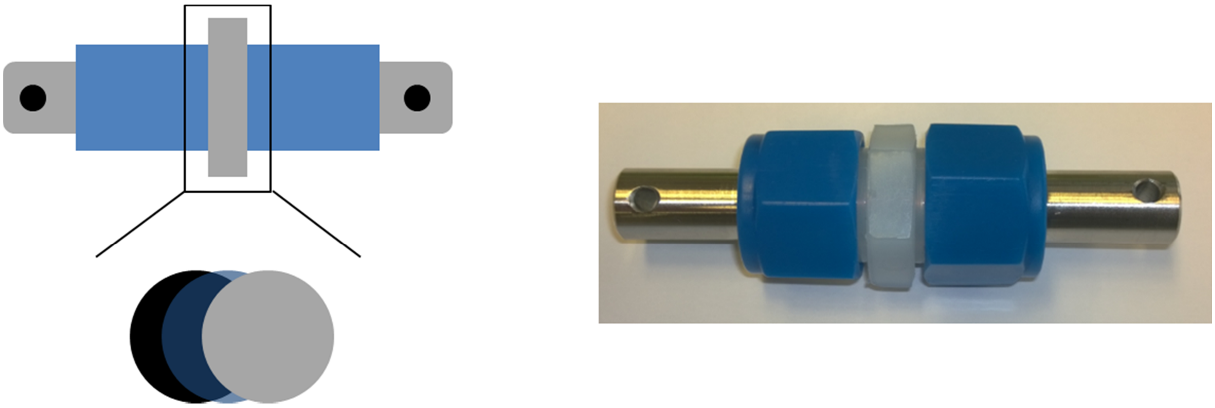

Fig. 19 Left: Schematic representation of a Swagelok type two electrode cell with supercapacitor stack assembly [Pt(carbon)/separator with electrolyte/(carbon)Pt]

Right: Picture of an assembled Swagelok cell

For the test in 1 M sodium chloride solution a homemade cell was used (**Fig. 20 c**). The ball milled material was mixed with a 60 wt.% poly tetra fluoro ethylene (PTFE) dispersion in water to yield a 9:1 ratio (active material : PTFE). Ethanol was added to the mixture until a rubber like mass was achieved (**Fig. 20 b**). The material was subsequently roll pressed to a thickness of 150 µm and dried at 60 °C overnight under vacuum. The sheets were cut into 4 cm times 4 cm pieces and placed onto graphite paper current collectors. Two pieces were sandwiched using a filter paper separator and clamped together. The whole stack was submerged in a 1 M sodium chloride solution serving as the electrolyte. The operating voltage window was 1.2 V.

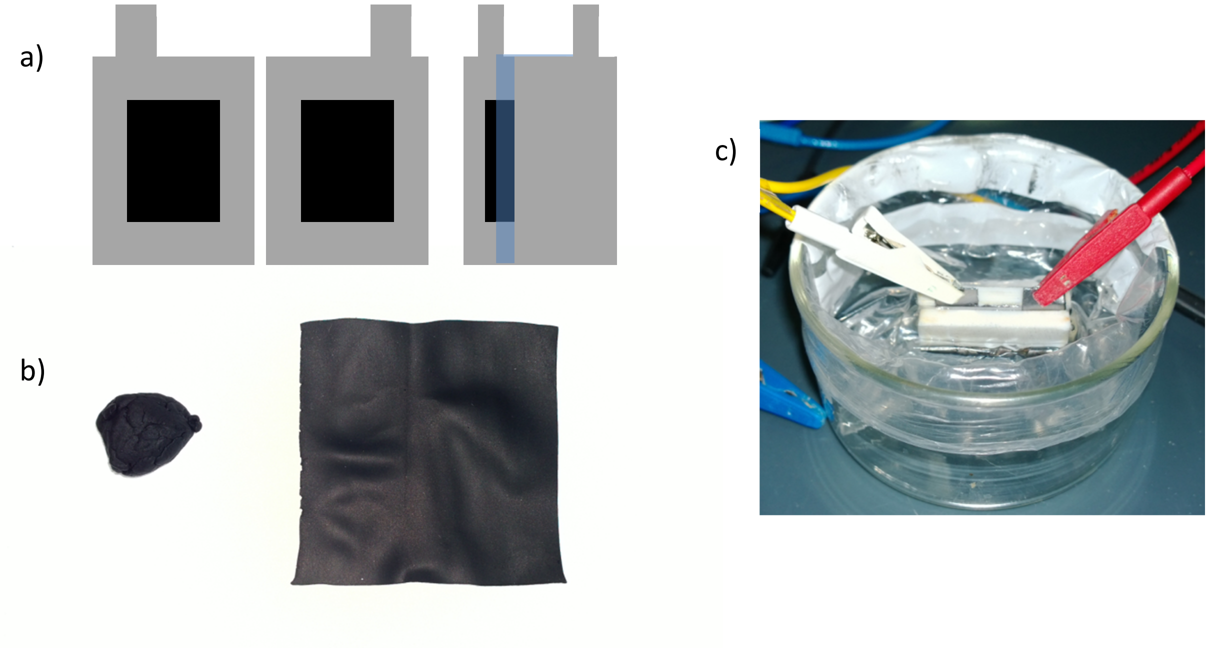

Fig. 20 a) Schematic representation of the cell with carbon sheets placed on graphite foil
b) Rubber like lump of carbon/PTFE and roll pressed carbon sheet
c) Picture of the actual test cell

3.2.5.2 Three Electrode Cell

The three electrode tests were conducted in a setup with a glassy carbon working electrode, a platinum counter electrode, and a saturated silver / silver chloride reference electrode (**Fig. 21**). A 1 M sulfuric acid served as the electrolyte. The active material was ball milled and 5 mg were mixed with 95 µL Nafion (5% solution) and 350 µL of absolute ethanol. 5 µL of this slurry was drop-cast onto the glassy carbon electrode and dried for 10 min at 50 °C. The voltage window was set to -0.2 to 0.8 V vs. Ag/AgCl(sat.).

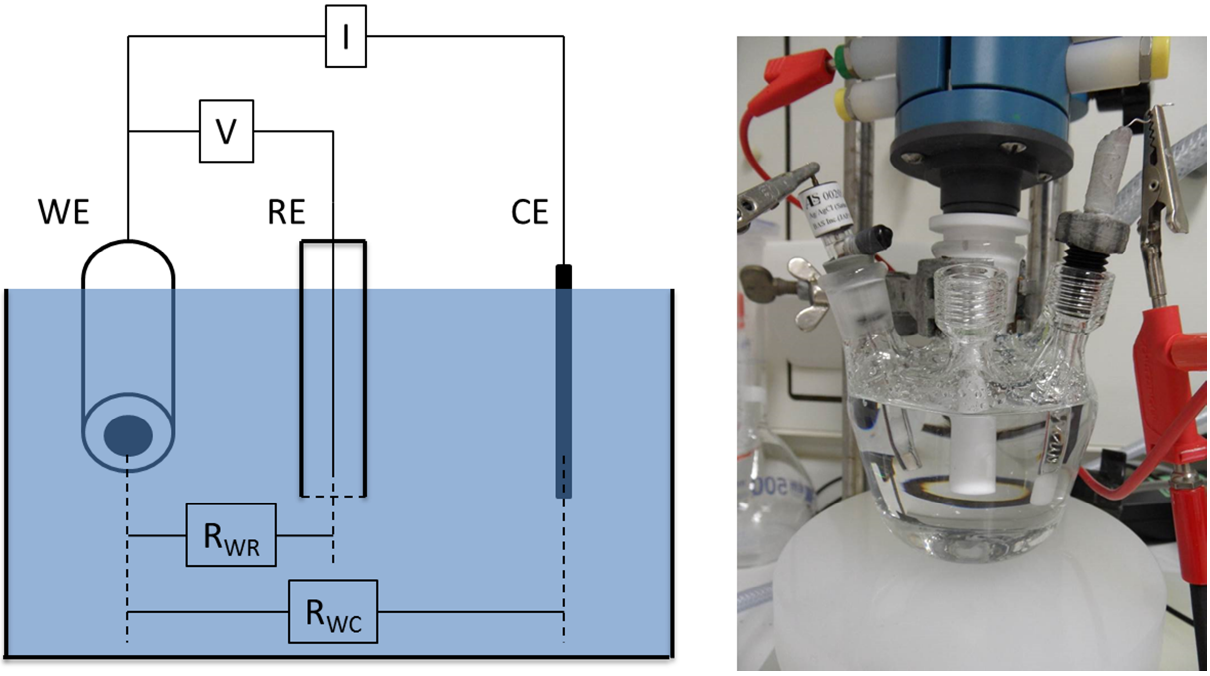

Fig. 21 Left: Schematic representation of the 3-electrode test setup with working (WE), reference (RE) and counter electrode (CE) and electrolytic resistance between working/reference(R_{WR}) and working/counter (R_{WC})

Right: Picture of the actual test cell

4 Lithium Sulfur Batteries

4.1 Introduction and State of the Art

Fig. 22 Reconstruction of the voltaic pile with zinc and silver electrodes (GNU license)

Inspired by the work of Luigi Galvani on animal electricity at the end of the eighteenth century, Volta set out to understand this phenomenon[86]. Volta showed that different metal arranged in a series and separated by cardboard soaked in brine were able to deliver a shock to a person when both terminals were touched. Voltas design from 1800, the so-called voltaic pile (**Fig. 22**), was the first battery ever created[87]. Despite its technology shortcomings it provided a steady current for around one hour and had a tremendous impact on electrochemistry and made early experiments on electrolysis and electrochemical reduction possible. Batteries soon became an important part of day to day life and more well-engineered cells where designed. The first mass produced battery was the Leclanche element developed in 1866[88], which was used to power telegraphy stations and the first telephones. The Leclanche cell was the predecessor to the widely successful primary zinc carbon and alkaline batteries[89].

With the invention of the electric generator in the mid nineteenth century, the demand for a rechargeable type of battery (secondary battery) arouse and was met by the lead acid battery of Gaston Plante. It was mass produced from 1880 onward and served as a power source for the electric starter in cars and is still in use today[90]. This makes the lead acid battery one of the most successful batteries of the 20th century. In fact, the development of new batteries was at a hold but with the higher storage demand for consumer electronics (e.g. cell phones, portable computer etc.), the interest in smaller batteries arose at the end of the 20th century. A system of choice was the lithium battery. The use of metallic lithium is very attractive since it has a low standard electrode potential of -3 V in combination with a low molar mass of 7 g mol^{-1} which in turn yields to a specific capacity of 3.8 Ah g^{-1} and an energy density of 11.4 kWh kg^{-1}. A suitable cathode material is the layered oxide lithium cobalt oxide $LiCoO_2$ which was extensively studied by J. B. Goodenough in the 1980s[91]. The dendritic growth of lithium during charge made the first secondary lithium batteries unsafe to use and severe failures were reported due to short circuits [92].

Already in the mid-1970s J.O. Besenhard demonstrated the intercalation of alkali metals into graphite[93]. Graphite shows a stepwise intercalation of lithium ions with the final product of LiC_6 which has an electrode potential of 0.01 V vs. Li/Li^+ and is ideally suited as anode material. The specific capacity of 372 mAh g^{-1} may be lower than that of metallic lithium but the absence of any lithium dendrite growth on graphite makes it much safer. Unfortunately, was the observed capacity not stable upon prolonged cycling and it was only later discovered that the electrolyte composition is a crucial factor[94]. Finally with the replacement of metallic lithium by graphite, a cell chemistry solely based on intercalation compounds was devised and the term lithium-ion batteries (**LIB**) was used henceforth[95]. LIB are constructed in a discharged state with $LiCoO_2$ and graphite as active materials and have to be charged prior to selling.

LIB were commercialized 1991 by the Sony cooperation and are ubiquitously used in today's consumer electronics[96]. A typical cell consist of graphite and lithium cobalt oxide as anode and cathode respectively. The electrolyte is a mixture of carbonates (e.g. diethylene carbonate and propyl carbonate) and a suitable lithium salt like $LiPF_6$. The cell chemistry of modern LIB is still the same as 24 years ago and cell engineering had the most influence on achieving higher energy densities. Over the years, more and more intercalation materials have been identified as suitable replacement for the expensive $LiCoO_2$[13]. Nonetheless, only one electron can be transferred in an intercalation compound and the increase in energy density is mostly depending on higher intercalation voltages. This has motivated a lot of research on high voltage materials e.g. $LiNi_{0.5}Mn_{1.5}O_4$ (4.7 V vs. Li/Li^+)[97]. A combination with graphite would yield a cell voltage of around 4.5 V and a potential energy density of 200 Wh kg^{-1} which is about 25% higher than that of current LIB. A major drawback of this approach is the need for a stable electrolyte capable of operating at high potentials on the cathode side. State-of-the-art electrolytes show an upper potential limit of around 4.3 V vs. Li/Li^+, and intensive research is focused on developing new electrolytes or additives[20].

Another way of increasing the energy densities is given by increasing the capacity of the electrode materials. This can be done by moving away from the established intercalation cell chemistry to a conversion battery. There is a number of conversion anode materials like silicon[98], tin[99], or lithium manganese nitride (Li_7MnN_4)[100] but a fitting cathode is essential. Sulfur is an attractive option for a lithium battery cathode. It can react with lithium to form lithium sulfide as follows:

$$S_8 + 16Li \longrightarrow 8Li_2S \qquad \text{Eq.(27)}$$

A lithium sulfur battery therefore would give a capacity of 1675 mAh g^{-1} which yields, with a discharge voltage of 2 V, to a total energy density of 3350 Wh kg^{-1}[101]. This is much higher than any known battery concept except for metal-oxygen batteries[102]. LSBs are regarded as a feasible option for electro mobility and a driving range of around 500 km would be possible. Furthermore, sulfur is abundant, easy to exploit, and hence cheap making it an ideal choice for future EVs, HEVs and even load leveling.

A shortcoming of sulfur is its low electrical conductivity of $1 \cdot 10^{-15}$ S m^{-1} which makes for a poor electrode material and a mixing with conductive carbon is necessary for a practical battery[103]. This concept is also known for traditional LIB where the cathode material is mixed with carbon black for a better conductivity. Practical batteries usually consist of about 80% active material. A second disadvantage is the formation of polysulfides Li_2S_n during the discharge of a LSB. Polysulfides with $n \geq 4$ are readily dissolved into the electrolyte and can diffuse to the lithium anode and react directly to the insoluble Li_2S[104]. This shuttle process causes a rapid capacity fading in a LSB. Conversion batteries often suffer from an extensive change in volume during charge and discharge. Silicon and tin show a volume increase of about four times which results in a pulverization of the active material[105, 106]. The density of Li_2S is 1.7 g mL^{-1}[107] and that of sulfur (S_8) around 2 g mL^{-1}[107] which results with Eq.(27) in a volume change of 45%. Although the change is much smaller than that for silicon or tin, it is still detrimental for the overall cell performance. Even though the concept of LSB is known since the 1960s, they were discarded due to their poor electrochemistry and short cycle life[108].

New impulses were given by the research of Linda Nazar *et. al.* in 2009 who demonstrated that sulfur can be confined into the ordered mesoporous carbon **CMK-3** by a simple melt infusion technique (**Fig. 23**)[101]. The confined sulfur is in close contact with the host material which solves the problem of the low electrical conductivity. Furthermore, the confinement is beneficial to trap the as formed polysulfides resulting in a better cycle stability and the high pore volume can account for the volume change during charge and discharge. The polysulfide shuttle is retarded by the sulfur confinement but not completely suppressed[101].

Confining sulfur into carbon hollow spheres is a very attractive approach since it allows high sulfur loadings. Hydrothermal derived carbon hollow spheres have been investigated as sulfur host by Titirici *et. al.* with very promising results[109]. Also other interesting carbon materials have been investigated (e.g. CDC[110], CNT[111]) followed by the research of Nazar.

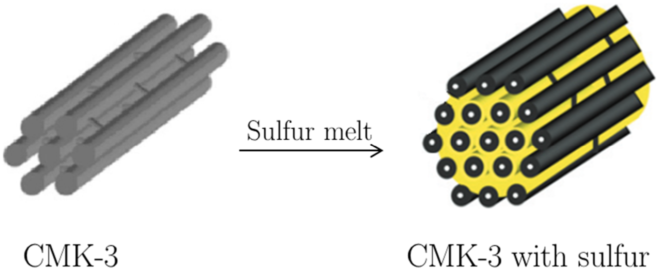

Fig. 23 Schematic illustration for the infiltration of CMK-3 with sulfur via a melt infusion technique[101]

Current research in LSB is devoted to increase the cycle stability by maintaining a high capacity. A classical surface modification by chemical vapor deposition requires high temperatures above 500 ° C[112, 113] which is not suited for sulfur due to its low boiling point of 445 ° C[107]. Low temperature coatings with graphene[114], modified graphene[115], or polyaniline[116] are possible options to enhance the cycle stability. Another option is the direct use of a heteroatom doped carbon hosts which can attract polysulfides e.g. nitrogen doped porous carbons[117].

Other research is focused on the optimization of the electrolyte system for LSB. State of the art electrolytes consist of a 1 M solution of LiTFSI[1] dissolved in a 1:1 mixture of 1,3-dioxolane and dimethoxyethane[118]. No chemical reactions occur between the electrolyte and polysulfides but the high solubility of polysulfides is detrimental to the overall performance[102]. Electrolytes with lower solubility towards polysulfides might enhance the cycle performance but are so far elusive. Set aside from liquid electrolytes, solid electrolytes have attracted some attention since they could suppress the dendrite formation and inhibit the polysulfide shuttle. They usually suffer from a high polarization due to a low conductivity and have to be cycled at elevated temperatures which in turn limits the cycle life [119].

LSB have gained a lot of interest over the last couple of years and are not only the focus of intense fundamental research but have already found their way to commercialization to some extent. Sion Power in cooperation with BASF developed a lithium sulfur cell with an energy density of 350 Wh kg^{-1} which is currently used for space and military applications[120]. Also various research projects are focused on the development of commercialisable LSB, e.g. the MaLiSu[121] and EUROLIS[122] project.

---

[1] lithium bis(trifluoromethylsulfonyl)imide

4.2 Fundamentals of Batteries

4.2.1 Thermodynamics

A battery consists of two redox couples separated from each other (**Fig. 24**). Electrons can flow via an external circuit from the anode to the cathode, thus delivering an useable current by allowing for the redox reaction to take place. For a lithium sulfur battery the separated redox reactions are:

Anode(-): $16Li \longleftrightarrow 16Li^{+} + 16e^{-}$

Cathode(+): $S_8 + 16e^{-} \longleftrightarrow 8S^{2-}$

Overall: $S_8 + 16Li \longrightarrow 8Li_2S$

The oxidation at the anode creates a surplus of electrons in comparison to the cathode where electrons are consumed. The difference in electron density between the anode and the cathode results in a cell voltage that quantifies the Gibbs free energy of the redox reaction, the driving force of the reaction. The active materials are in contact via an electrolyte to allow for ion diffusion from one half-cell to another. A battery acts like a galvanic cell during discharge and like an electrolysis cell during charge. Regardless, the nomenclature is always that of a galvanic cell. The reversible reaction will proceed until the whole cell has reached the thermodynamic equilibrium and both half-cells show the same potential.

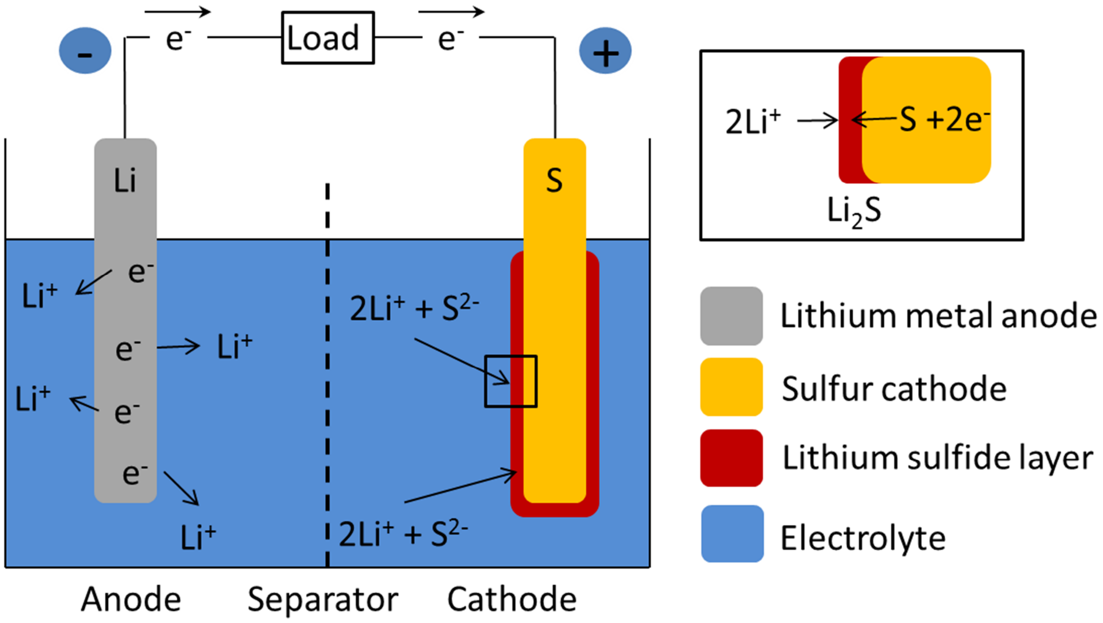

Fig. 24 Simplified representation of a lithium sulfur battery during discharge

The potential difference of two half cells is given by the Nernst equation:

$$E = E_0 - \frac{R \cdot T}{n_e \cdot F} \ln \prod_i a_i^{\upsilon_i} \qquad \text{Eq.(28)}$$

with the equilibrium cell voltage E (also referred to as open circuit voltage (OCV)), the standard cell voltage E_0 (difference between the standard potentials φ_0); the gas constant R, the thermodynamic temperature T, the number of exchange electrons n_e, the activity a, and the stoichiometric coefficient υ. Since the electrolyte is not involved in the overall cell reaction in a LSB (Eq.(27)) the right term of the Nernst equation will be zero and the OCV equals to 2.5 V ($\varphi_0(Li/Li^+)$ = -3 V; $\varphi_0(S^{2-}/S)$ = -0.5 V). For a practical lithium sulfur cell, a terminal cell voltage E_t of around 2.0 V is usually reached. The OCV is lowered during discharge due to an IR-drop[1] which can be significant for organic electrolytes. Furthermore, overpotentials η can play a role since the cell is not operated under open circuit conditions. From the concentration, diffusion, charge transfer, and reaction overpotential the last two will contribute the most in a packed cell. The terminal cell voltage is given by:

$$E_t\left(\begin{smallmatrix}\text{charge}\\ \text{discharge}\end{smallmatrix}\right) = E \pm ESR \cdot |I| \pm \sum_i \eta_i(I) \qquad \text{Eq.(29)}$$

The Nernst equation Eq.(28) can be translated into the Gibbs free energy ΔG with:

$$\Delta G = -n_e FE \text{ and } \Delta G_0 = -n_e FE_0 \qquad \text{Eq.(30)}$$

$$\Delta G = \Delta G_0 + R \cdot T \ln \prod_i a_i^{\upsilon_i} \qquad \text{Eq.(31)}$$

This means the maximum reversible energy delivered by a LSB equals to -4187 Wh kg^{-1} or -3350 Wh kg^{-1} under terminal conditions ($M(S_8)$: 0.256 kg mol^{-1}; F: 26.8 Ah mol^{-1}; n_e: 16; E: 2.5 V; E_t: 2.0 V).

---

[1] The IR-drop, also referred to as voltage drop, is caused by the internal resistance of the cell (resistance of the electrolyte etc.) and depends on the applied current. The voltage drop will result in heat dissipation; see also chapter A 3.2.3 page 16 for more details.

4.2.2 Voltage Profile of Lithium Sulfur Batteries

The thermodynamic cell voltage of a lithium sulfur battery is 2.5 V and should stay constant over the discharge process until all of the sulfur is consumed by the redox reaction (**Fig. 25**). Even if an Ohmic voltage loss and overpotentials are taken into account, the voltage is only lowered by a factor. However, for an actual cell a different behavior is observed and three voltage plateau can be identified during the discharge process. The Gibbs phase rule describes the degrees of freedom F in a given system of a number of components C and phases P.

$$F = C - P + 2; \quad F_{p,T} = C - P \qquad \text{Eq.(32)}$$

There are two components in a LSB and the degree of freedom at constant temperature and pressure will be one for a one phase region and zero for a two phase region. This means that a voltage plateau correspond to a two phase region e.g. sulfur/polysulfide or polysulfide/polysulfide. This shows that the discharge to Li_2S proceeds stepwise via the long chain polysulfides and each polysulfide shows a different Nernst potential[123]. The polysulfides with Li_2S_n ($n \geq 4$) are readily dissolved into the organic electrolyte and will diffuse throughout the cell and can react with the metallic lithium anode to Li_2S. This redox shuttle causes an irreversible capacity loss during the discharge process. On the other hand, the Li_2S layer on the anode is beneficial in suppressing the lithium dendrite formation. The capacity loss is very high for the first few cycles but usually decrees over time once the Li_2S layer becomes thicker on the anode and the electrolyte is saturated with polysulfides.

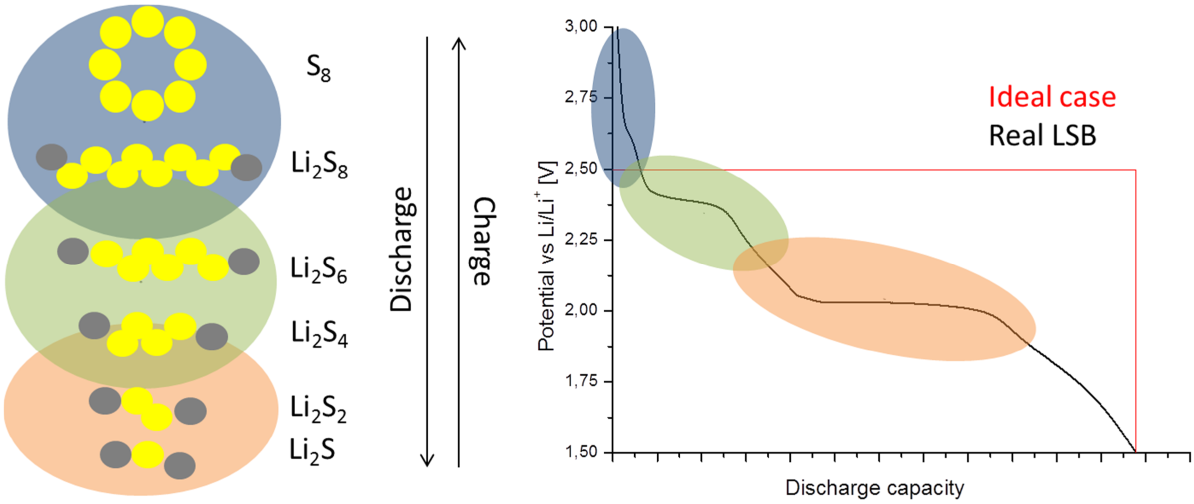

Fig. 25 Voltage profile of a LSB with different 2 phase regions indicated by plateaus

4.2.3 Evaluation of Batteries

The specific capacity Q_s of an active material is determined by Faradays first law as follows:

$$Q = n \cdot n_e \cdot F$$

$$Q_s = \frac{Q}{m} = \frac{n_e \cdot F}{M} \qquad \text{Eq.(33)}$$

with n being the number of moles. The theoretical Q_s for a LSB is 1675 mAh g^{-1} (n_e: 16; F: 26.8 Ah mol^{-1}; $M(S)$: 256 g mol^{-1}). In order to determine the specific capacity of an actual cell the battery is charged and discharged at a constant current and Eq.(33) becomes to:

$$Q_{\text{discharge}} = \frac{I_{\text{discharge}} \cdot t_{\text{discharge}}}{m_e} \qquad \text{Eq.(34)}$$

The capacity is calculated in respect to the mass of sulfur in the active material. The discharge rate, also C rate is given as the fraction between the discharge current and the capacity:

$$C = \frac{I_{\text{discharge}}}{Q_s} \qquad \text{Eq.(35)}$$

A C rate of 1C or C/10 would mean a discharge in one or 10 hours respectively. The energy can be calculated with the average discharge voltage $\overline{U}_{\text{discharge}}$:

$$E = Q_{\text{discharge}} \cdot \overline{U}_{\text{discharge}} \qquad \text{Eq.(36)}$$

Another important factor of a battery is the coulomb efficiency q_{Ah} and the energy efficiency q_{Wh}:

$$q_{Wh} = q_{Ah} \cdot \frac{\overline{U}_{\text{discharge}}}{\overline{U}_{\text{charge}}} \cdot 100\% \qquad \text{Eq.(37)}$$

4.2.4 Test Cells for Battery Evaluation[1]

All battery tests were conducted in a pouch cell setup with lithium metal as counter electrode placed on nickel foil (**Fig. 26**). The sulfur impregnated carbons were mixed with carbon black (printex EX10) and PvdF acting as a conductive support and binder, respectively. The mass ratio was 80:10:10 of active material to carbon black to PvdF. The mixture was mixed with N-methyl-2-pyrrolidone and the slurry was spread onto an aluminum foil. After drying at room temperature, the anode and cathode were sandwiched using a glass fiber separator soaked in electrolyte (1 M LiTFSI in sulfolane). The sandwiched cell was placed in a coffee bag and sealed under vacuum. The whole process was done in a glove box to ensure an absence of water in the cell.

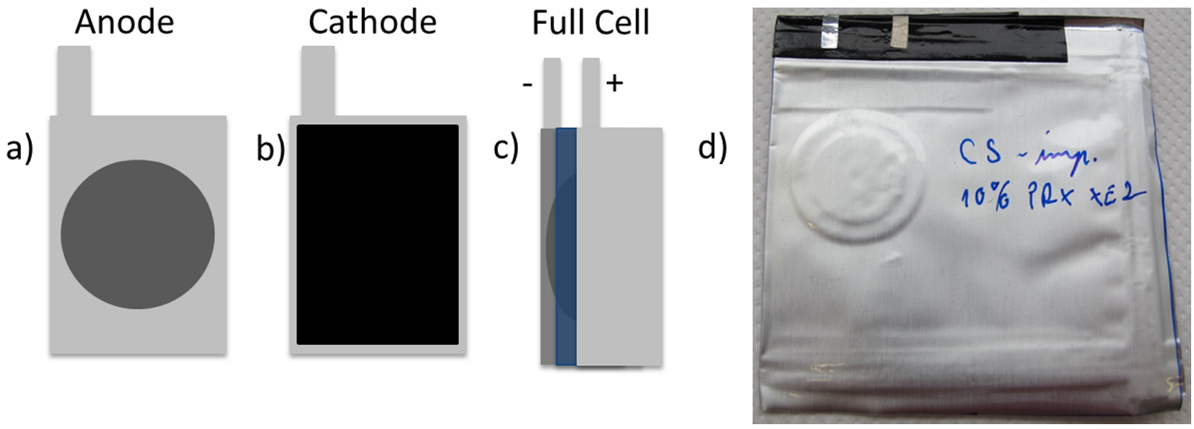

Fig. 26 a) Lithium metal place on a nickel current collector with terminal
b) Carbon coating on aluminum current collector with terminal
c) Sandwiched cell between glass fiber separator soaked in electrolyte
d) Picture of an assembled full cell

---

[1] All battery test presented in this thesis were conducted at the National Institute of Chemistry (NIC) in Ljubljana, Slovenia (Alen Vizintin and Robert Dominko are highly acknowledged).

B Hydrothermal Carbonization

1 Introduction

HTC is a long known process which allows the production of carbon from crude biomass under self-generated pressure inside an autoclave at elevated temperature. Typical synthesis conditions are 200 °C for 20 h with an autogenous pressure of about 10 bar (**Fig. 27**). HTC is sometimes compared to the natural coalification of biomass; shorted from millions of years to a mere day. Since the synthesis is carried out in water even wet, unprocessed biomass can be employed making HTC not only sustainable but cheap by nature.

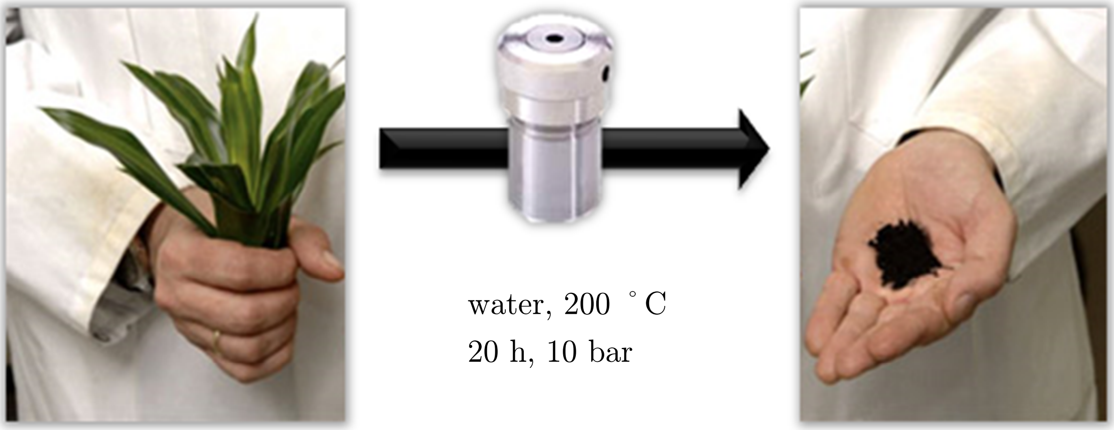

Fig. 27 Simplified scheme for the HTC process

The first scientific work on HTC dates back to the research of Bergius in 1913[124]. Early work focused on understanding the formation of coal from biomass under HTC conditions. HTC was rediscovered about 15 years ago and has become a diverse technique to produce various functional carbons for CO_2 adsorption[125], energy storage[126, 127], catalysis[128], and other fields. The beauty of the process lies not only in its simplicity but in the use of cheap, sustainable carbon precursors which makes HTC a role model of green chemistry.

It was shown by Fellinger *et. al.* that borax acts as a catalyst for the carbon formation leading to smaller primary particles and carbon monoliths[129]. In this work HTC is used for the production of nitrogen doped carbon monoliths from glucose in dilute ammonia solution with the addition of borax. Those monoliths have been activated with CO_2 in order to create a high surface area material suitable for SC applications.

1.1 Basic mechanism of HTC

The HTC process can be simplified by the following equation:

$$C_6H_{12}O_6 \longrightarrow C_6H_2O + 5H_2O \qquad \Delta_R H = -1105\,kJ/mol \qquad \text{Eq.(38)}$$

It is an exothermic polycondensation meaning that once the reaction has started it is self-sustained. Being a bottom up process, the reaction time can be used to control the size of the particles, on the other hand, the polycondensation is a step-growth process and a high conversion is necessary to achieve high yields.

A closer look at the mechanism reveals multiple steps involved (**Fig. 28**). At first, glucose is converted into fructose which is subsequently dehydrated to **h**ydroxy**m**ethyl**f**urfural (**HMF**). It was shown that HMF is in fact the main intermediate if hexoses are used[130]. HMF is consequently further dehydrated and polymerizes into amorphous carbon.

The dehydration of fructose to HMF can either occur via the open chain molecule or from the fructofuranose form. It was demonstrated by M. J. Antal *et. al.* that the reaction proceeds via fructofuranose[131]. This makes the conversion of glucose to fructose the first vital step in this reaction cascade. Since glucose mainly exists in its pyranose form, a direct formation of HMF from glucose is prohibited.

The so called **L**obry de **B**ruyn - **A**lberda van **E**kenstein transformation (**LBAE**) describes the conversion of glucose to fructose. The first step is the intermediate formation of a dienol which tautomerizes to fructose. The LBAE can be catalyzed acidic or basic. It was shown that basic conditions favor the transformation, possibly due to the electronegativity throughout the glucose molecule caused by the hydroxyl functions[132].

The dehydration of fructofuranose to HMF is usually catalyzed by acids but it was shown that basic conditions also allow the formation of HMF. Furthermore, the amount of HMF generated in acidic conditions is roughly the same as in basic conditions if glucose is the biomass under question. On the other hand, the generated amount of fructose is three times higher in basic conditions. This shows that the formation of fructose might be the limiting step of the overall reaction. If fructose is directly used as a carbon precursor the amount of HMF generated is about 1/3 higher under acidic conditions[133, 134].

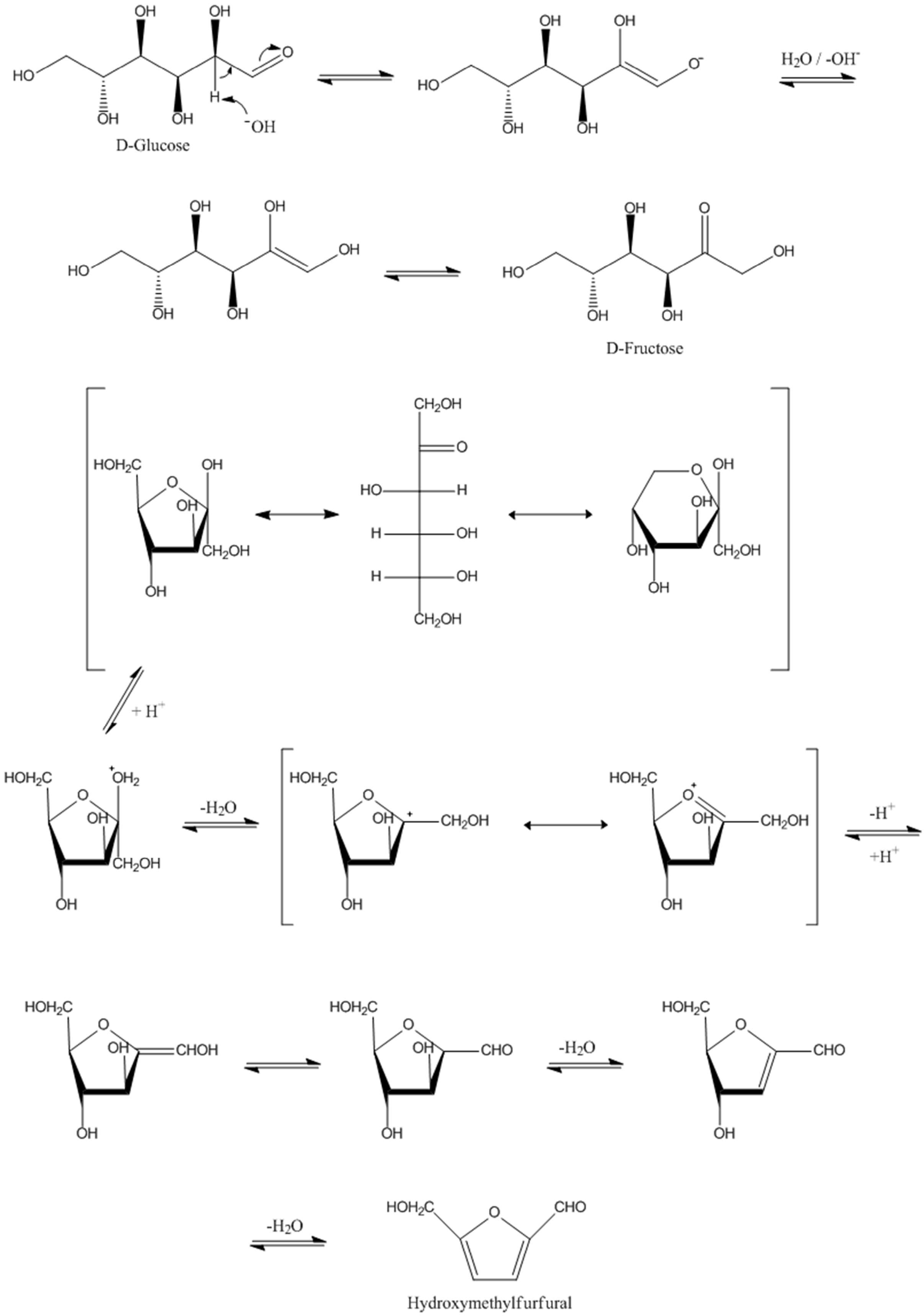

Fig. 28 Reaction scheme of the formation of *D*-glucose to *D*-fructose and subsequent dehydration to hydroxymethylfurfural

The polymerization of HMF under HTC conditions is, up to date, not very well understood. In general, multiple reactions are possible. On one hand, the furan ring can undergo typical furan reactions (electrophilic substitution, [4+2] diels alder addition) or it can react as the 1,4-diketone analog in aldol reactions. On the other hand, the hydroxyl and aldehyde group offer additional reaction pathways for HMF. Nucleophiles can either substitute the hydroxyl group or react with the aldehyde function. All those reactions are possible ways to form insoluble polymers during the HTC process and are partially summarized in **Fig. 29**. The reactions II and III are only involving HMF and its 1,4-diketone isomer and thus offering a way to describe the polymerization of HMF with itself. Nonetheless, the formation of various organic compounds can occur during the HTC treatment of glucose. The generation of formic acid and levulinic acid is well-known to take place during HTC and other intermediates might be involved in the polymerization as well, this leads to a complicated reaction mechanism.

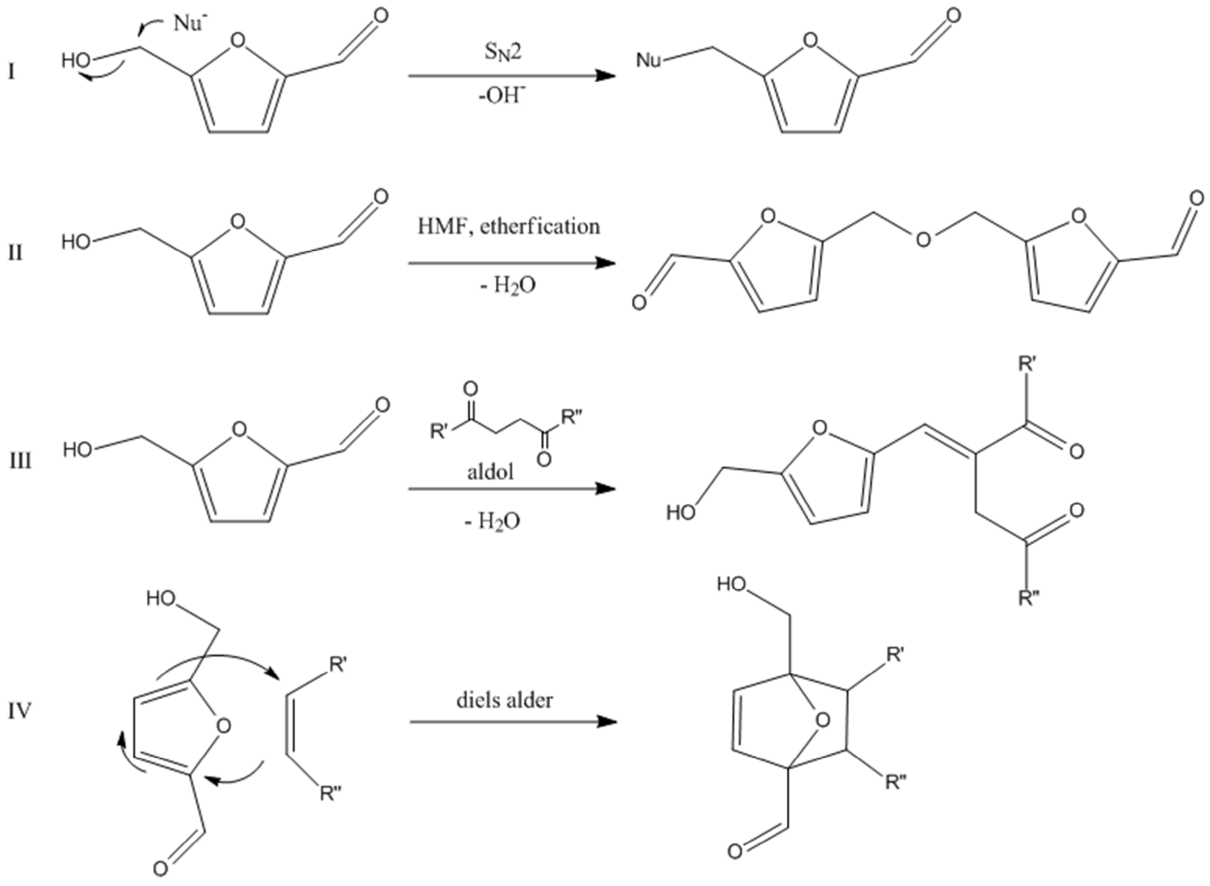

Fig. 29 Excerpt of possible reactions involved in the HTC process; adapted from [135]

1.1.1 Catalytic Effect of Borax

The use of borax is a new concept in the HTC community and was recently developed by T. P. Fellinger *et. al.* It was shown that a small amount of borax can accelerate the carbon formation drastically and carbon monoliths are formed instead of carbon dispersions. Furthermore, much smaller primary particles are formed. Where traditional HTC produces particles in the range of 1 to 10 µm, borax mediated HTC delivers particles below 100 nm[129, 136].

A possible side reaction in the HTC is the reversible acetalization of HMF with the remaining carbohydrates. The acetal function would block further reactions on the aldehyde group, hence lowering the concentration of reactive monomers. Borax is known to complex sugars, in turn offering a competitive reaction to the acetal formation (**Fig. 30**)[135].

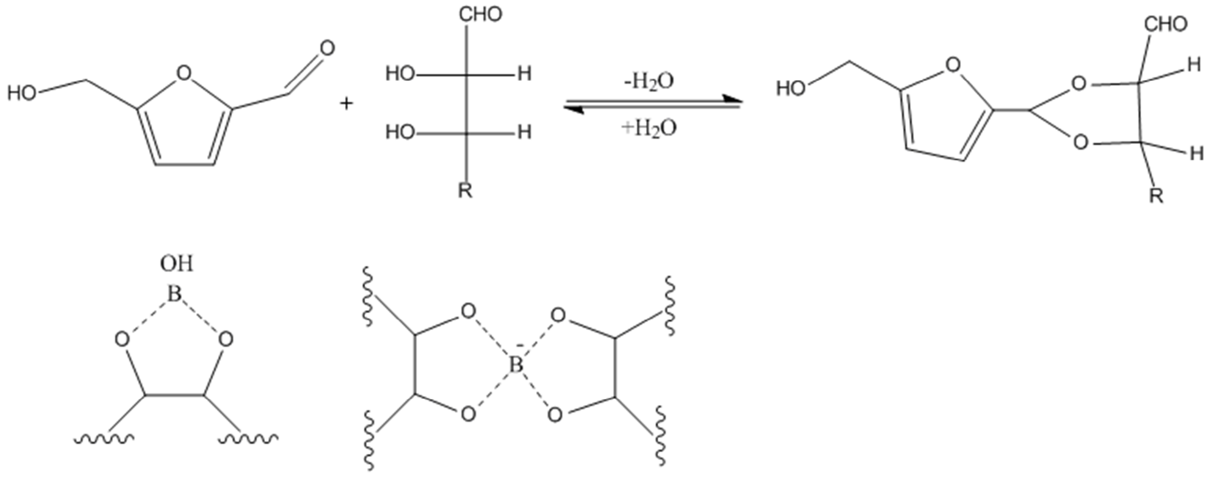

Fig. 30 Top: acetalization of HMF with carbohydrates; adapted from [135]
Bottom: complexation of carbohydrates with borax; adapted from [135]

Set aside from the use of borax as an additive in the HTC process, it was recently shown by Fechler *et. al.* that the use of salt mixtures is not only suitable as a porogen in ionothermal carbonization but also for hydrothermal derived carbons. By employing hypersaline conditions carbon aerogel like structures with up to 650 $m^2 g^{-1}$ were achieved[137].

1.2 Activation of HTC Derived Carbons

Carbon materials produced via hydrothermal treatment usually show a low surface area in the range of ca. 20 m^2 g^{-1} which is unsatisfactory for a lot of electrochemical applications. The surface area and morphology can be tuned by using a hard template (e.g. silica) as a scaffold (**Fig. 31**). Silica can be subjected to high temperatures under inert gas conditions without decomposition. This makes it a good choice for HTC since the amorphous carbons have to be post pyrolysed. It was demonstrated by Titirici *et. al.* that different silica templates are suitable for HTC but they have to fit the surface charge of hydrothermal carbons to be fully incorporated[109, 138]. Anyhow the scaffold removal with hydrofluoric acid is a drawback of silica templates and involves hazardous chemicals such as hydrofluoric acid.

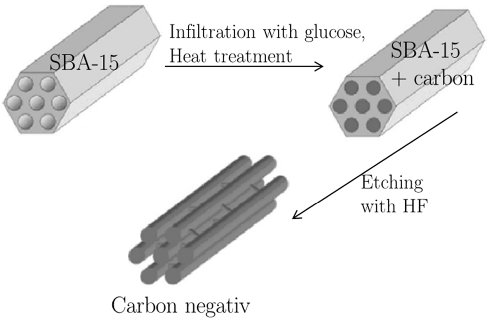

Fig. 31 Example of hard templating with SBA-15

The chemical and physical activation of carbon materials are an alternative to the hard templating approach. The chemical activation is done by mixing already pyrolysed carbons with KOH or NaOH followed by a heat treatment at elevated temperature under inert gas. The alkali hydroxide reacts with carbon producing carbonates:

$$6MOH + 2C \xrightarrow{T, N_2} 2M + 3H_2 + 2M_2CO_3;\ M = K\ or\ Na \qquad \text{Eq.(39)}$$

The carbonates have to be washed out in dilute acid after the activation. The generated pores are usually in the micropore range and surface areas of up to 3000 m^2 g^{-1} can be achieved[139]. The chemical activation proved to be suited for hydrothermal carbons, as was demonstrated by Titirici and Falco, and surface areas of around 3000 m^2 g^{-1} have been reported[140, 141].

The above reaction can be found throughout various papers in the carbon community but a clear mechanism for the chemical activation is still missing[142, 143]. Linares-Solano and co-workers studied the reaction in more detail[144]. They were able to prove the formation of carbonates and the evolution of hydrogen gas. The formation of pure alkali metals on the other hand was not proven. The feasibility of the carbothermal reduction can be estimated from an Ellingham diagram (**Fig. 32**). If the graph for CO or CO$_2$ is more negative than the line for the metal oxide, a carbothermal reduction is possible but can still be hindered due to low kinetics and activation barriers. The carbothermal reduction of sodium oxide would require temperatures higher than 1500 °C which is above the sublimation temperature of Na_2O of 1275 °C[145]. Assuming, the formation of alkali metals allows for a simple explanation of the chemical activation mechanism but is clearly a simplification.

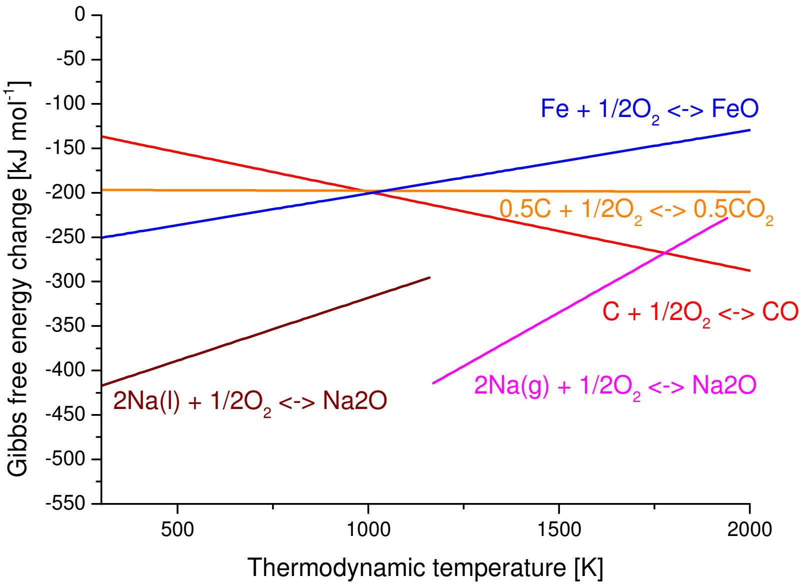

Fig. 32 Ellingham diagram for iron and sodium with carbon monoxide and carbon dioxide formation; All reactions are calculated for one mole of oxygen and assuming temperature independence for the reaction enthalpy and entropy (thermodynamic data were taken from NIST)

The physical activation[1], on the other hand, involves the exposure of the carbon to steam or CO_2 and can be done directly during the pyrolysis. Both reactions produce pores by carbon conversion to carbon monoxide.

$$\text{Steam activation}: H_2O + C \longleftrightarrow CO + H_2 \qquad \text{Eq.(48)}$$

$$\text{Boudouard equilibrium}: CO_2 + C \longleftrightarrow 2CO \qquad \text{Eq.(49)}$$

The reaction of steam with glowing coal is industrially used to produce hydrogen and the equilibrium between carbon dioxide and monoxide is the well-studied Boudouard equilibrium. The CO_2 activation was chosen as the activation process for HTC carbons in this work since it is easy to control and no further washing steps are required.

---

[1] The term physical activation is not very well chosen since it implies a physical process even though it is clearly a chemical reaction. Nonetheless will the term physical activation be used throughout this thesis to be in line with the literature in this field.

2 Hydrothermal Derived Nitrogen Doped Carbon Monoliths and CO_2 Activation

Three different ratios between ammonia and glucose were chosen to produce N-doped carbon monoliths via HTC. The ratio of glucose to ammonia was varied from 0.25 to 0.75 to yield carbogels with different nitrogen contents. The samples will be denoted NC_025, NC_050, and NC_075, whereas NC stands for N-doped carbon. The products were washed in water and ethanol in order to remove any residues and subsequently freeze dried (see page A-5 for details). Freeze drying was chosen since it keeps the gel structure more intact (cryogels) than conventional drying in air (xerogel).

The obtained carbons showed a high nitrogen content of up to 9 wt.% indicating a good uptake of the ammonia during the reaction. In fact, the calculated C/N ratios are close to the measured values via elemental analysis (EA) (**Table 1**). In addition, a reference sample (mass ratio of 0.75) without borax showed a similar nitrogen content indicating an absence of side reactions between ammonia and borax.

All samples showed a carbon content of about 64 wt.% which is a common value for HTC derived carbons[129, 140]. The carbon yield of the samples was around 65% with respect to glucose. In contrast, hydrothermal carbons derived with borax but without ammonia usually show a carbon yield of 80%[129] which shows that the presence of ammonia leads to a slower reaction rate. It was shown in ref. [45] that HTC under basic conditions produces a higher amount of levulinic acid compared to neutral conditions. Very likely the production of different acids (e.g. levulinic acid, acetic acid, and formic acid) is preferred until enough ammonia is neutralized to organic ammonium salts and a certain pH is reached. Once the actual hydrothermal carbon formation starts those salts can be integrated into the carbon material but, nonetheless, longer reaction times are necessary for adequate yields, the reactions were done within 20 h whereas the reaction time in ref. [129] was only 8 h.

Table 1 Elemental analysis of HTC derived N-doped carbons; HTC conditions: 200 °C for 20 h

Sample	Elemental analysis [wt.%]			C/N ratio	
	N	C	H	measured	calculated
NC_025	3.1	64.1	5.3	20.6	20.6
NC_050	6.1	62.2	5.4	10.2	10.3
NC_075	9.0	60.7	5.5	6.7	6.9
Ref_075	9.3	64.2	5.4	6.6	6.9

The surface areas of the freeze dried samples were around 100 $m^2 g^{-1}$ but only 20 $m^2 g^{-1}$ for the reference sample. This effect can be attributed to the much smaller particles produced by the borax route, which are below 100 nm in diameter (**Fig. 33.**), whereas the sample without borax showed particles of >10 µm. Borax proved to be beneficial for the production of nitrogen doped carbogels with small primary particles. The size directing effect of borax was unaffected by the addition of ammonia.

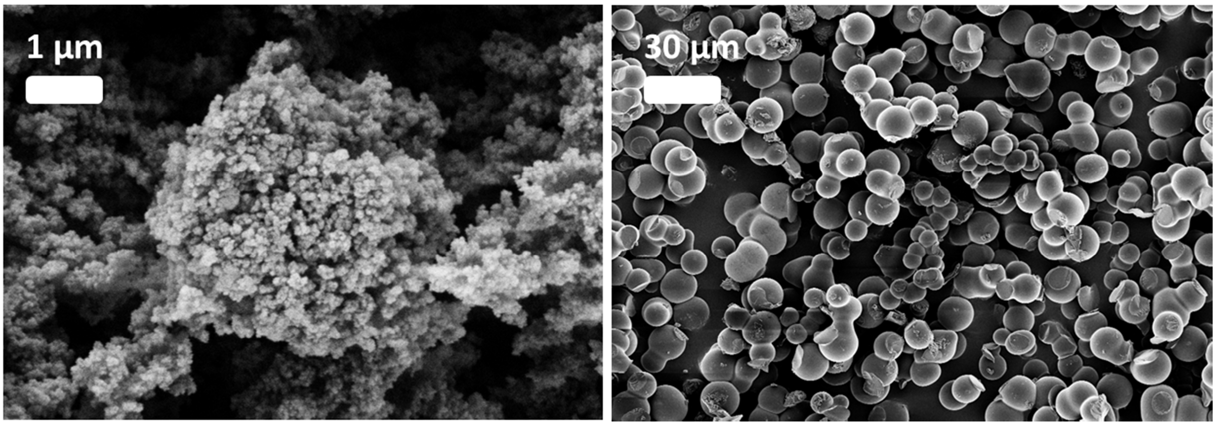

Fig. 33 SEM images of NC_075 (left) and Ref_075 (right)

The HTC treatment at 200 ° C produced amorphous hydrothermal carbons with high oxygen contents which lacked a suitable conductivity for electrochemical applications, therefore, a post pyrolysis at 850 ° C in combination with a CO_2 activation was done (see page A-5 for details). High temperature treatments on porous carbons usually results in a substantial shrinkage of the material, which at the same time, can potentially cause a loss of surface area due to collapsed pores. By way of comparison, the samples were also pyrolysed without any activation. Activated sample names will be extended by the suffix _AC and non-activated by _C.

Where the freeze dried samples showed surface areas around 100 $m^2 g^{-1}$, a decrease to 80 $m^2 g^{-1}$ and 45 $m^2 g^{-1}$ was recorded for NC_075_C and NC_025_C respectively (**Table 2**). This loss in porosity can be attributed to a pore collapse and especially the energetically unfavored micropores can be closed during the carbonization. The same effect can be expected for the activated sample (**Fig. 34**) but the CO_2 activation proved to be beneficial for the generation of micropores. The samples NC_050_AC and NC_075_AC showed a similar surface area of 1020 and 1011 $m^2 g^{-1}$ respectively, whereas NC_025_AC showed 685 $m^2 g^{-1}$. It seems that a higher amount of nitrogen has a positive effect on the overall surface area. This can also be seen from the reference samples where an increase in surface area was found with higher nitrogen ratios (**Table 2**). All samples developed an open aerogel like structure after the carbonization and activation with a visible mesoporosity (**Fig. 34**).

Table 2 N_2 Sorption data for pyrolysed and CO_2 activated N-doped carbons (QSDFT model)

Sample	S_{total} [m^2 g^{-1}]	S_{micro} [m^2 g^{-1}]	S_{meso} [m^2 g^{-1}]	V_{total} [cm^3 g^{-1}]
NC_025_AC	685	622	63	0.32
NC_050_AC	1020	956	64	0.57
NC_075_AC	1011	943	68	0.49
NC_025_C	45	n/a	n/a	0.11
NC_050_C	59	n/a	n/a	0.15
NC_075_C	82	n/a	n/a	0.19

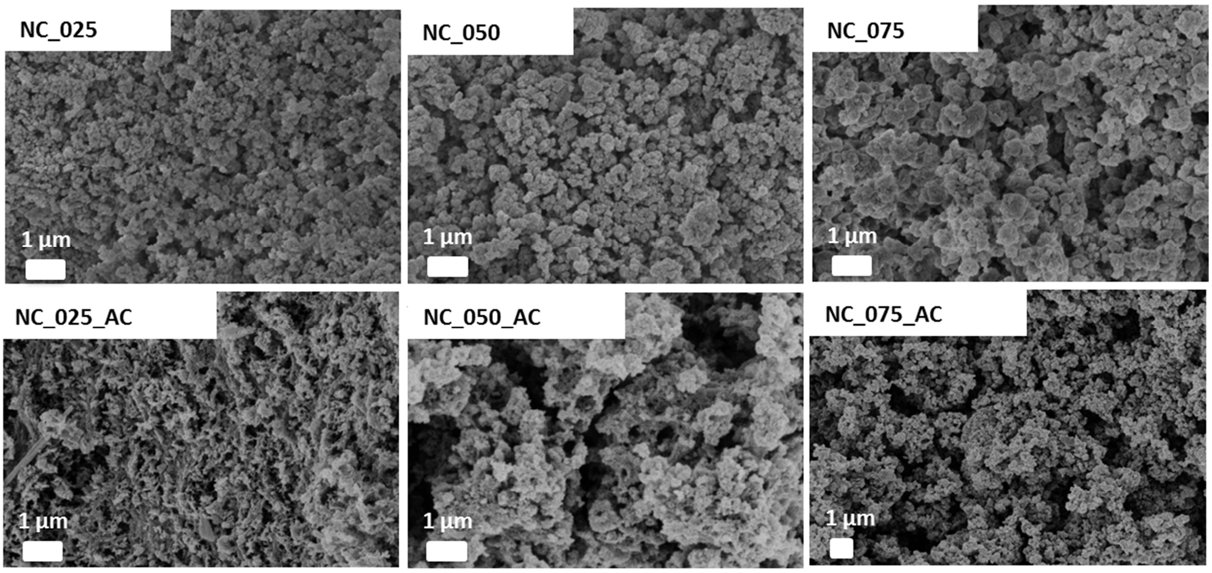

Fig. 34 SEM images of hydrothermaly synthesized N-doped carbons after freeze drying (top) and post carbonized plus CO_2-activated samples (bottom)

From the N_2 sorption experiment, a type I isotherms for NC_025_AC and type II behavior for NC_050_AC and NC_075_AC with a H3 hysteresis loop was observed (**Fig. 35**). All samples demonstrated almost exclusively microporosity with additional mesopores and also macroporosity for NC_050_AC and NC_075_AC. This hierarchical pore structure can be beneficial for an improved ion diffusion to smaller pores under high current conditions assuming long mesopores with micropores longitudinal along the mesopore.

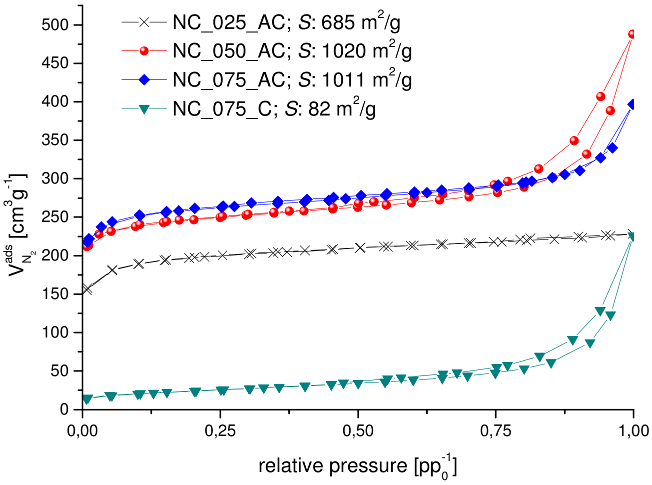

Fig. 35 N_2 adsorption/desorption isotherms for the activated carbon samples and reference sample NC_075_C

The pyrolysis of amorphous nitrogen doped carbons usually results in a loss of nitrogen. This can be explained by the lattice distortion and by the fact that graphite is the most thermodynamic stable carbon allotrope. The more organized the carbon framework becomes the more pronounced is this effect. A pyrolysis thus always comes with a tradeoff and the temperature has to be chosen carefully.

All samples demonstrated an increase of carbon content upon pyrolysis at 850 ° C (**Table 3**). The carbonization is accompanied by a loss of oxygen and nitrogen and especially surface functions like hydroxyl and amino groups are easily lost during high temperature treatments. It can be seen from the reference samples that only 0.9 wt.% and 2.8 wt.% of nitrogen is lost during the carbonization of NC_050_C and NC_075_C, respectively (see also **Table 1**). For NC_025_C an increase of 0.3 wt.% was found.

The activated samples were also analyzed by means of X-ray photoelectron spectroscopy (XPS) in order to elucidate the surface composition (Table 3). A high amount of nitrogen was measured for all samples indicating a high nitrogen density at the carbon surface. Those surface nitrogen functions are believed to play a vital role in pseudocapacitors since they can easily interact with the electrolyte and undergo redox reactions creating a faradaic current in addition to the capacitive current in SC. The deconvolution of the N1s signal showed a distribution between pyridinic, pyrrolic, quaternary, and pyr-N-oxide whereas the latter gave the lowest contribution. For NC_050_C and NC_075_C, a high level of quaternary nitrogen was found (> 40 at.%). This speaks for a good integration of nitrogen atoms into the carbon lattice and will lead to an enhanced conductivity of the carbon material. In addition to nitrogen atoms, also a high level of oxygen atoms were detected which can further contribute to a pseudocapacitance via surface keto and hydroxyl groups.

Table 3 EA results for activate and non-activated samples; XPS data for activate samples

Sample	EA [wt.%]; XPS [at.%]				XPS; deconvolution of N1s [at.%]			
	N	C	O*	H	pyridinic	pyrrolic	quaternary	Pyr-N-oxide
NC_025_AC	3.9 (2.6)	85.5 (88.1)	9.1 (9.3)	1.5	37.2	28.3	24.9	9.7
NC_050_AC	5.9 (3.9)	83.9 (89.2)	8.8 (6.9)	1.4	32.2	16.7	42.9	8.2
NC_075_AC	7.0 (5.3)	80.9 (87.5)	10.7 (7.2)	1.4	34.2	15.2	41.2	9.5
NC_025_C	3.4	82.7	12.3	1.6	n/a	n/a	n/a	n/a
NC_050_C	5.2	79.7	13.4	1.7	n/a	n/a	n/a	n/a
NC_075_C	6.2	73.7	18.3	1.8	n/a	n/a	n/a	n/a

* Calculated from EA as difference

The order of the activated carbons was investigated via **X-ray diffraction (XRD)**. For the as-prepared and freeze dried samples a typical diffraction pattern of amorphous carbon was recorded (**Fig. 36**). After the carbonization, the (002) interlayer stacking peak was shifted to a higher 2 theta value indicating a shrinkage of the carbon lattice distance due to a loss of heteroatoms and starting graphitization. Furthermore, an additional intralayer stacking peak was observed for the carbonized sample, speaking for an ordering during the high temperature treatment and the formation of graphitized domains.

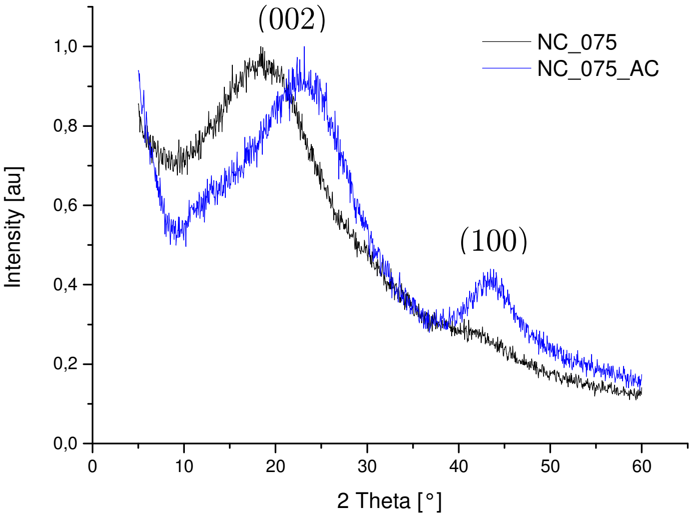

Fig. 36 XRD pattern for hydrothermally derived carbon and activated sample (NC_075/NC_075_AC shown as example)

In conclusion, the HTC proofed to be suited for the production of N-doped carbons with different levels of nitrogen doping by simple variation of the glucose to ammonia ratio. Furthermore, the CO_2 activation was found to be beneficial to develop highly micro porous carbons with surface areas of up to 1020 m^2 g^{-1}. The obtained activated carbon monoliths showed a hierarchical pore structure with contribution from micro and mesopores. Furthermore, the amount of nitrogen in the final carbon was with up to 7 wt.% rather high and only a moderate N-loss of 2 wt.% was observed throughout the high temperature treatment at 850 ° C.

3 SC performance of N-Doped Hydrothermal Carbons

The SC performance of the CO_2 activated N-doped carbons was evaluated by means of CV, CC, and EIS (see A for details). In the CV an almost ideal behavior was observed for NC_025_AC and NC_050_AC whereas NC_075_AC displayed a deviation from a rectangular curve (**Fig. 37 left**). NC_075_AC showed a hump during the forward and backward scan indicating a possible redox process overlapping with the double layer capacitance. The absence of any redox peaks for NC_025_AC and NC_050_AC can be attributed to the lower levels of nitrogen doping and thus lower pseudocapacitance.

Furthermore, from the presentation of C_{sp} over v it can be seen that the specific capacitance reached values as high as 151, 180, and 201 F g^{-1} at 2 mV s^{-1} for NC_025_AC, NC_050_AC, and NC_075_AC respectively (**Fig. 37 right**). With an increase in scan rate to 200 mV s^{-1} a decrease to 59, 61, and 65% of the initial capacitance for NC_025_AC, NC_050_AC, and NC_075_AC was observed respectively. Not only was the highest capacitance recorded for NC_075_AC but also a lower capacitance loss at higher scan rates. The capacitance scaled with the nitrogen amount of the examined samples. However, an increase of 20% was observed from NC_025_AC to NC_050_AC and only an increase of 10% was measured from NC_050_AC to NC_075_AC. Since the surface area of NC_050_AC and NC_075_AC is almost similar the increase can be attributed to the higher nitrogen doping. For NC_025_AC a much smaller surface area was measured compared to the other samples which explains the lower capacitance.

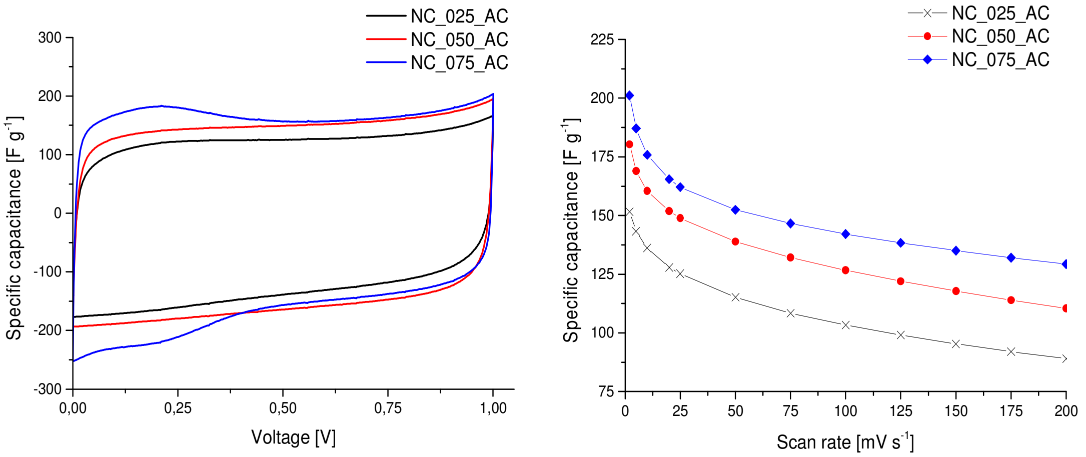

Fig. 37 Left: CV for the activated N-doped carbons at 20 mVs^{-1}
Right: Evolution of the capacitance with increasing scan rates for the activated N-doped carbons

A similar trend was observed in the CC experiment (**Fig. 38 a**). At a current density of 0.2 A g^{-1} capacitance values of 150, 180, and 185 F g^{-1} have been observed for NC_025_AC, NC_050_AC, and NC_075_AC, respectively. All samples showed a good capacity retention at high current densities. Still a rather high remaining capacitance of 63, 69, and 78% of the initial capacitance was observed at 20 A g^{-1} for NC_025_AC, NC_050_AC, and NC_075_AC. NC_075_AC showed only a slight loss of capacitance while NC_050_AC displayed a higher loss. This can be attributed to the higher N-doping for NC_075_AC since both samples have a similar surface area.

In order to evaluate the long term stability of the materials a charge/discharge experiment at 10 A g^{-1} was conducted with 5000 repetitions (**Fig. 38 b**). It can be seen for all carbons that literally no loss in capacitance occurred within the tested 5000 cycles. This speaks for a stable and reversible process. Furthermore, the Coulombic efficiency q_{Ah} (Eq.(42)) is around 99% indicating a very good charge utilization.

$$q_{Ah} = \frac{Q_{\text{discharge}}}{Q_{\text{charge}}} \cdot 100\% = \frac{t_{\text{discharge}}}{t_{\text{charge}}} \cdot 100\% \qquad \text{Eq.(42)}$$

The charge and discharge curves at 0.2 A g^{-1} for NC_025_AC and NC_050_AC displayed a triangular shape, further speaking for an ideal behavior (**Fig. 38 c**). NC_075_AC showed a deviation from the other samples and a change in slope was observed around 0.25 V. This supports the behavior observed in the CV test and can be attributed to a pseudocapacitancitive nature of the sample.

A very useful representation of different materials is given by the Ragone plot. In such a graph, the energy density E_s is plotted against the power density P_s on a logarithmic scale. The graph can be divided into different time zones showing how fast the charge or discharge process would be at the respective combination of E_s and P_s. For the investigated materials, energy densities as high as 20.3, 24.5, 25.3 Wh kg^{-1} were measured for NC_025_AC, NC_050_AC, and NC_075_AC respectively (**Fig. 38 d**). A power density of up to 17.6 kW kg^{-1} was recorded at 20 A g^{-1} while still reaching 15.5 $Whkg^{-1}$ for NC_075_AC. This translates into a discharge time of less than 3.2 s. Furthermore, NC_075_AC showed a lower loss in performance at high current densities compared to the other materials.

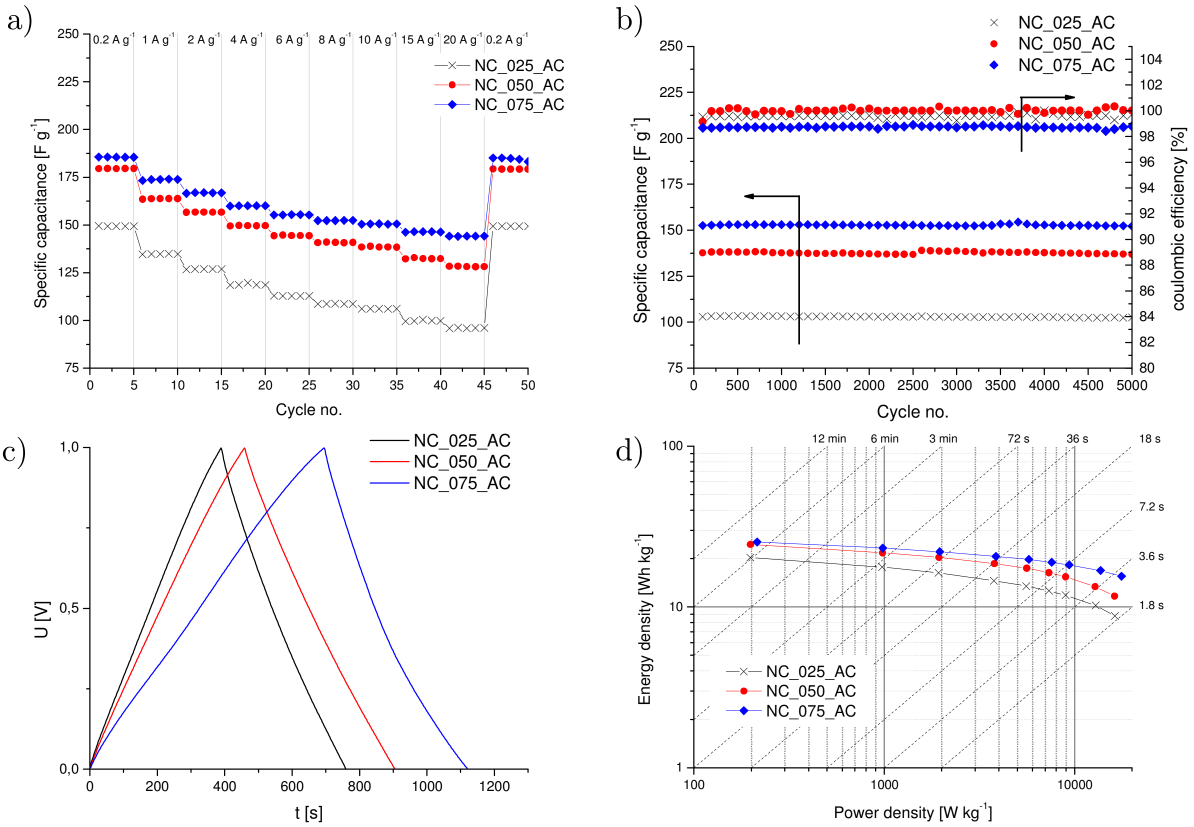

Fig. 38 a) CC results for increasing current densities from 0.2 to 20 Ag^{-1} (ΔU: 1 V)
b) Cycle stability for 5000 cycles at 10 Ag^{-1} (ΔU: 1 V)
c) Charge discharge curve at 0.2 Ag^{-1}
d) Ragone plot

The 3-electrode test for NC_050_AC and NC_075_AC gave capacitance values of 271 F g^{-1} and 264 F g^{-1}, respectively (**Fig. 39**). With increasing current densities, the capacity showed the same behavior as in the two electrode test where NC_075_AC outperforms NC_050_AC. Both materials showed only a low IR drop at 20 A g^{-1} indicating a good conductivity. Interestingly, the measured capacitance in the 3-electrode test is about 1.5 times higher than the actual values derived from the 2-electrode tests. This underlines the importance of SC test in a symmetrical setup to avoid an overestimation of the materials SC performance as was previously discussed by Stoller and Ruoff [146].

Titirici and Falco also employed HTC to produce carbon materials from inexpensive biofuel production waste products (i.e. corncob hydrolysis products)[147]. They achieved high surface areas of up to 2300 m^2 g^{-1} after KOH activation with a nitrogen content of about 1.5 to 1.8 wt.% and an oxygen content of about 17 wt.%. Even though the nitrogen content is lower than in this study the specific capacitance from 3-electrode measurements was already 300 F g^{-1} at 0.25 A g^{-1}. The combination of a high surface area with an appropriate PSD and a high heteroatom content leads to a desirable active material, which shows that a high nitrogen content alone is not necessarily leading to a high specific capacitance.

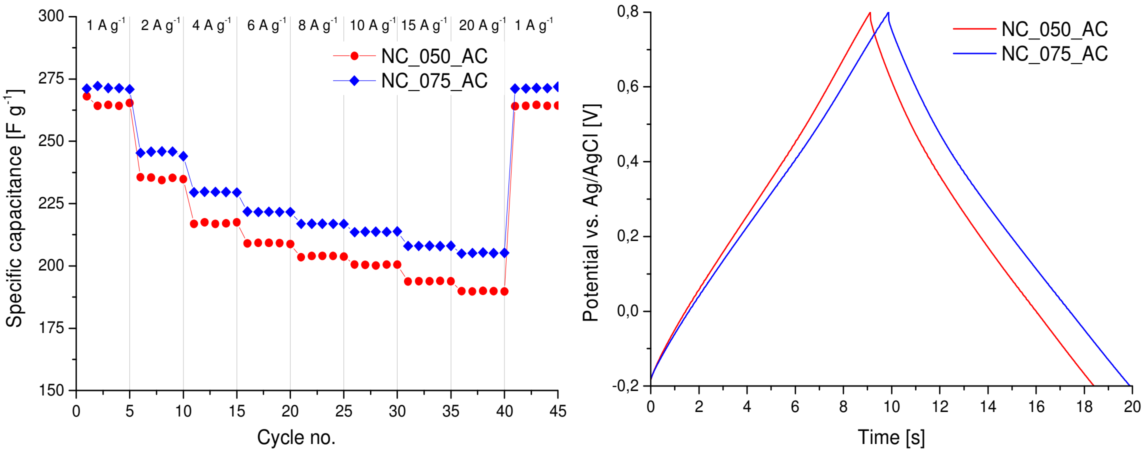

Fig. 39 Left: CC results for increasing current densities from 1 to 20 A g^{-1}; 3-electrode test
Right: Charge discharge curve at 20 A g^{-1}; 3-electrode test

The ESR calculation from the CC measurements showed a strong voltage dependence (**Fig. 40**). The ESR was measured to be 7.2, 5.6 and 5.7 Ω for NC_025_AC, NC_050_AC, and NC_075_AC respectively at 0.2 A g^{-1}. The slightly higher ESR for NC_025_AC can be explained by the lower nitrogen level which results in a lower electric conductivity. On the other hand, with the increase of nitrogen from NC_050_AC to NC_075_AC no impact on the ESR was observed. Apparently a maximum contribution of nitrogen to the conductivity was reached between 5.9 and 7.0 wt.% of nitrogen. The decrease of the ESR with increasing current densities can be explained by a lower electrochemical accessed active surface area and diffusion limitations at higher currents. At lower current densities more pores of the material are accessed by the electrolyte ions. In respect to the equivalent circuit (see **Fig. 18** p. 20) a higher ESR can be expected since each pore contributes to the overall ESR. Also the contribution of smaller pores to the ESR is higher than that of bigger, faster accessible pores.

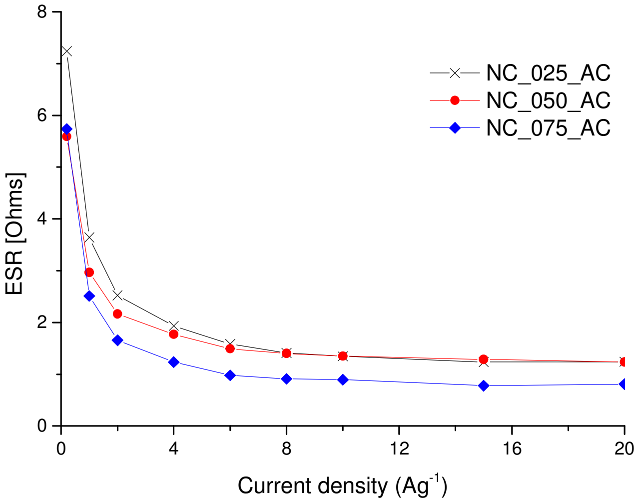

Fig. 40 ESR evolution over current density for the studied N-doped carbons

The impedance study revealed a behavior close to an ideal capacitor for all materials. The carbons showed a time domain in the Nyquist plot indicated by a semicircle at high frequencies (**Fig. 41 left**). The diameter of the semicircle is 0.28, 0.47, and 0.18 Ω for NC_025_AC, NC_050_AC, and NC_075_AC respectively. This low R_{ct} speaks for a fast process as can be expected for the boundary between conductive carbon and the platinum current collector. Nonetheless, the frequency response is better for NC_075_AC (**Fig. 41 right**) which showed higher capacitance at high frequencies compared to the other carbons. The relaxation time constant is mostly depended on the pore structure of the material. Since all investigated carbons are microporous with some mesoporosity a similar τ_0 of around 2.5 s (0.39 Hz) was measured.

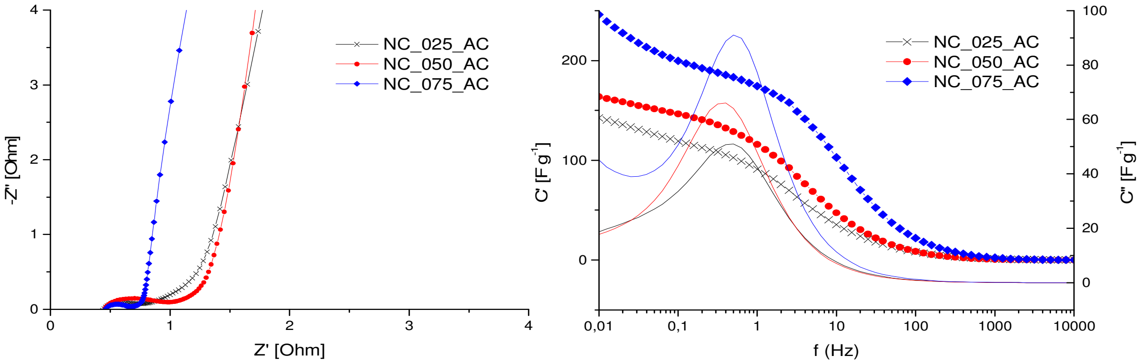

Fig. 41 Left: Nyquist plot of the activated carbon materials
Right: Bode diagram with scatter lines (C') and continuous lines (C'')

In order to find a correlation between the capacitance and other material properties some contributing factors are summarized in **Table 4**.

Table 4 Summary of surface area analysis (QSDFT), EA and XPS for all activated carbon samples with the specific capacitance from CC measurements at 0.2 and 20 Ag^{-1}

Sample	C_{sp} @(0.2 Ag^{-1}) [F g^{-1}]	C_{sp} @(20 Ag^{-1}) [F g^{-1}]	S_{total} [m^2 g^{-1}]	S_{micro} [m^2 g^{-1}]	N [wt.%] [at.%]
NC_025_AC	149	96	685	622	3.9 (2.6)
NC_050_AC	179	128	1020	956	5.9 (3.9)
NC_075_AC	185	144	1011	943	7.0 (5.3)

A correlation between the surface area and the capacitance is most obvious but generally not straight forward. The area determined by N_2 sorption is not strictly related to the electrochemical active surface area which can be much smaller (**Fig. 42 left**). No relation between the S_{total} or S_{micro} versus the capacitance was found.

Since the pseudocapacitance should increase with the amount of surface functions a representation of C_{sp} over the amount of nitrogen is given in **Fig. 42 right**. With an increase in nitrogen a growth in specific capacitance was recorded. This relation is more pronounced at higher current densities, most probably due to a higher relative contribution of surface functions. At lower current densities a wide array of micropores can be accessed which can contribute significantly to the overall capacitance as described in ref. [77]. This effect will become less distinct with an increase in current densities.

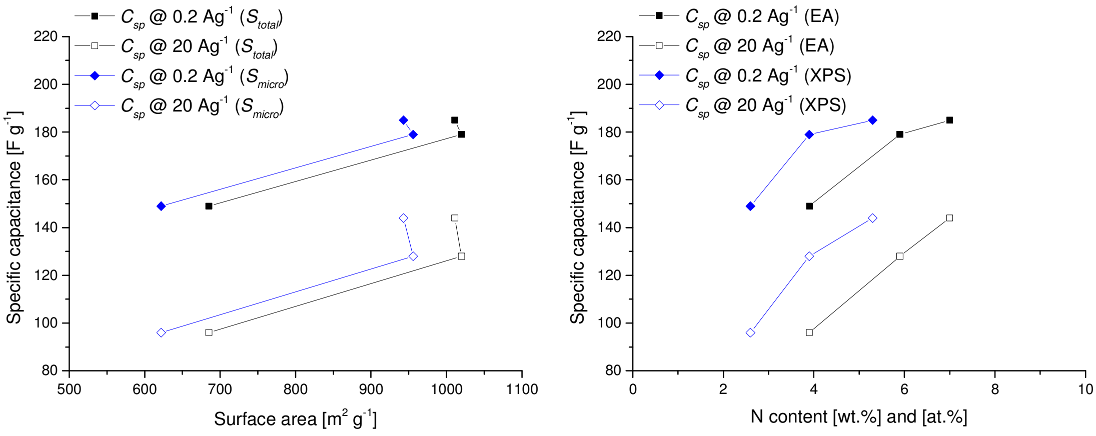

Fig. 42 Left: Specific capacitance over the total and microporous surface area for 0.2 and 20 Ag^{-1}
Right: Specific capacitance over the N content (EA and XPS) for 0.2 and 20 Ag^{-1}

C Ionothermal Carbonization of Biomass via a Salt Melt Approach

1 Introduction

As a versatile alternative to the HTC an ionothermal approach coupled with a salt templating strategy can essentially yield porous, conductive carbons in a one-step synthesis. As mentioned before the salt template allows for the production of porous carbons with only water being used as template removal agent. So far salt templating has been solely used in carbonization reactions of ionic liquids where, depending on the amount and nature of the eutectic, properties like morphology and surface area could be tuned as was demonstrated by Fechler[148].

In order to mimic the HTC process, a solution based synthesis was used. Glucose was dissolved in water together with varying amounts of zinc chloride. The solution was subsequently heated to the final carbonization temperature (800, 900, or 1000 °C) and washed in water to remove any residual amounts of salt (**Fig. 43**). The low boiling point of $ZnCl_2$ of 732 °C makes it an ideal template and a recovery of evaporating $ZnCl_2$ in a gas scrubber would allow for a possible circular process. For the introduction of heteroatoms to the carbon framework glucose was changed to glucoseamine (nitrogen source) or 2-thiophenecarboxylic acid (**TCA**) was dissolved as a sulfur source. Since all educts are dissolved in water, a homogeneous mixing on a molecular scale is achieved.

Finally, the influence of a binary salt mixture namely zinc chloride with cesium acetate was investigated as a possible option to obtain independently tunable porosity. In the following described carbons have been investigated as electrode materials for SC and LSB.

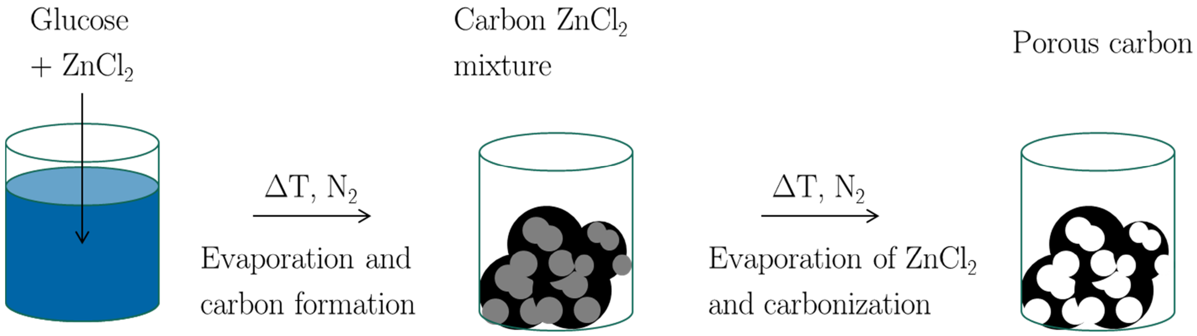

Fig. 43 Schematic of the carbonization process with $ZnCl_2$ as salt template

2 Porous Carbons Derived from Glucose with $ZnCl_2$

The influence of the glucose to $ZnCl_2$ ratio was investigated for a 1:1 and 1:5 mixture with a final carbonization temperature of 800, 900, and 1000 °C (see page A-5 for synthesis details). The samples will be depicted as TC_ratio_temp, e.g. TC_11_1000 describing the sample with a glucose to $ZnCl_2$ ration of 1:1 and a final carbonization temperature of 1000 °C.

The SEM pictures of the carbon samples revealed a strong dependence on the glucose to zinc chloride ratio (**Fig. 44**). For a one to one ratio a rather dense material is obtained with no visible mesoporosity. On the other hand, an increase of $ZnCl_2$ gives a carbon material with an aerogel like morphology and visible mesoporosity is achieved. Smaller fractions of zinc chloride led to smaller agglomerates and thus to a different morphology compared to a higher ratio. Furthermore, the synthesis temperature has no impact on the morphology observed via SEM.

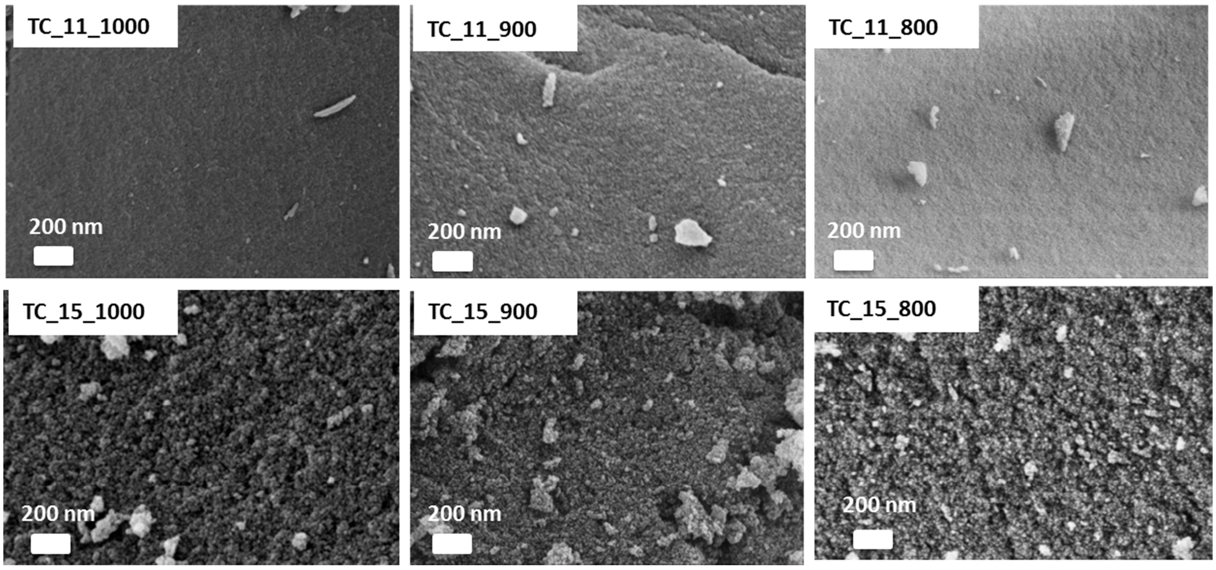

Fig. 44 Top: Glucose:$ZnCl_2$ (1:1) and carbonization temperature of 1000 to 800 °C (left to right)
Bottom: Glucose:$ZnCl_2$ (1:5) and carbonization temperature of 1000 to 800 °C (left to right)

A closer look at the carbon samples produced at 1000 °C, further confirms the importance of the glucose to $ZnCl_2$ ratio (**Fig. 45**). It can be seen from the TEM images that TC_11_1000 developed a continuous microporous structure whereas TC_15_1000 showed a mesoporous framework. Both materials are amorphous carbons and no higher degree of order was observed in the HRTEM images (**Fig. 45 inset**).

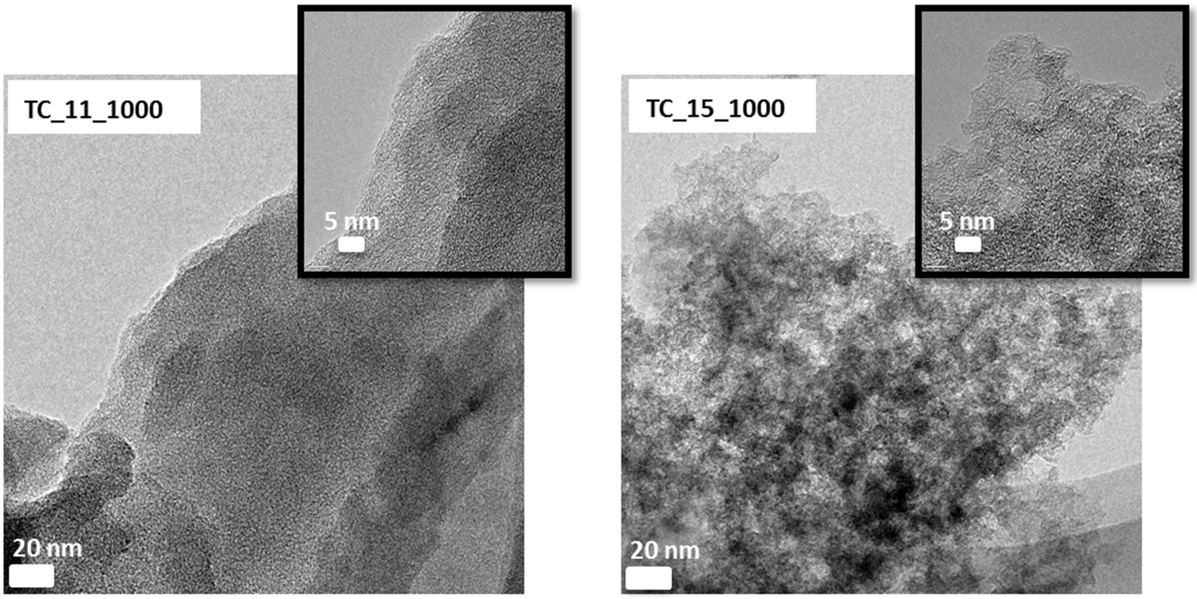

Fig. 45 TEM image of the TC_11_1000 (left) and TC_15_1000 (right) with HRTEM shown as inset

The nitrogen sorption data are in agreement with the conclusions drawn from the SEM and TEM images (**Table 5**). The material can be tuned from a more microporous to a mesoporous carbon by simply adjusting the glucose to $ZnCl_2$ ratio (**Fig. 46**). A 1:1 ratio gave rise to a narrow pore size distribution (**PSD**) with a maximum at 2.4 nm diameter and a big contribution from micropores (**Fig. 46 a, b**). The highest surface area was recorded for TC_11_900 with 1714 m^2 g^{-1} and a contribution from micropores of 1490 m^2g^{-1}. Increasing the zinc chlorid amount led to a hierarchically PSD with only a small contribution from pores below 2 nm (**Fig. 46 c, d**). The mesopore materials showed the highest surface area for TC_15_900 with 1385 m^2 g^{-1} (413 m^2 g^{-1} from micropores). In general, the highest surface areas were observed at 900 °C and lower surface areas at 1000 °C due to a stronger particle shrinkage and pore collapse. On the other hand, the measured pore volume was much higher for the mesoporous samples which showed an aerogel like morphology. For TC_11_900 and TC_15_900 a pore volume of 0.80 and 2.24 cm^3 g^{-1} was measured respectively. The PSD itself was not affected by the carbonization temperature and was kept over the whole tested set of temperatures.

As expected the carbon content increased throughout the carbonization. The oxygen content varied from around 3 wt.% at 1000 °C to ca. 7 wt.% at 800 °C. All characterization data are summarized in **Table 5**.

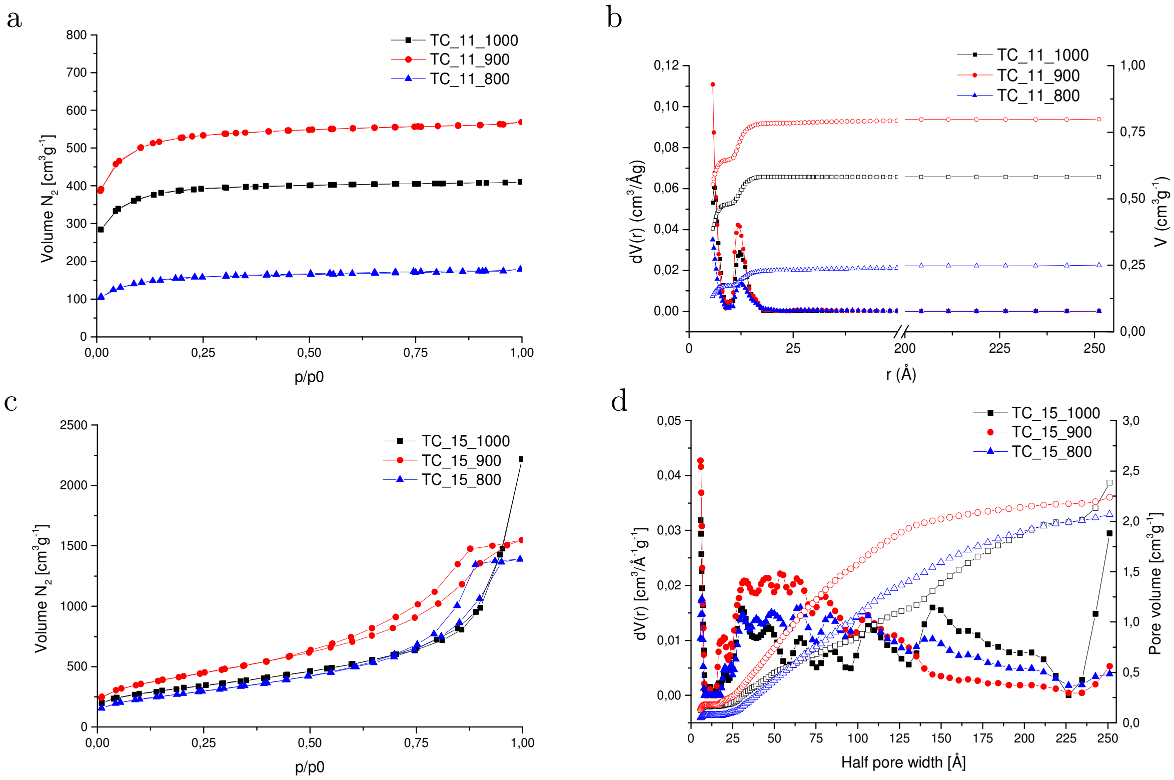

Fig. 46 N_2 isotherms and PSD for microporous (a,b) and mesoporous (c,d) samples; QSDFT model

Table 5 Summary of N_2 sorption values with total and microporous surface area and total pore volume; EA for all samples

Sample	S_{total} [m^2 g^{-1}]	S_{micro} [m^2 g^{-1}]	V_{total} [cm^3 g^{-1}]	C [wt.%]	H [wt.%]	O^* [wt.%]
TC_11_1000	1570	1414	0.58	96.1	1.1	2.8
TC_15_1000	1077	373	2.38	95.3	1.2	3.4
TC_11_900	1714	1490	0.80	94.3	1.2	4.4
TC_15_900	1385	413	2.24	93.2	1.4	5.4
TC_11_800	488	390	0.25	91.0	1.9	7.0
TC_15_800	959	206	2.06	91.1	1.7	7.1

* Calculated from EA as difference

2.1 Mechanistic Considerations on the Carbon Formation from Glucose

The browning reaction of sugar or aqueous sugar solutions is well known and belongs to the non-enzymatic browning reactions i.e. maillard reactions. However, the caramelization is not very well understood and involves a multitude of reactions and chemical compounds. For the reaction to pure carbon, HMF was suggested as a possible building block for the carbon formation. The reaction will occur as described in the previous chapter for the HTC process (see **Fig. 28** and **Fig. 29**). Zinc chloride will act as a catalyst for the dehydration of fructofuranose to HMF due to its Lewis acid character.

The reaction was studied for a solution of glucose and $ZnCl_2$ of a 1:1 ratio. The solution was heated and samples were taken after different times until a solid product was obtained (**Fig. 47**). No visible reaction occurred during the first 40 minutes. With continuous water evaporation, the solution became more viscous and a first browning reaction was observed at around 170 °C, visible by a slight yellowish color. Additional heating led to a darker color and finally to an onsetting carbonization at 280 °C. The carbonization was continued until 350 °C was reached in the reaction chamber. This experiment corresponds to the first step of the thermal carbonization process as was shown in **Fig. 43**. The samples were analyzed by means of Fourier transform infrared spectroscopy (FTIR) and nuclear magnetic resonance spectroscopy (NMR).

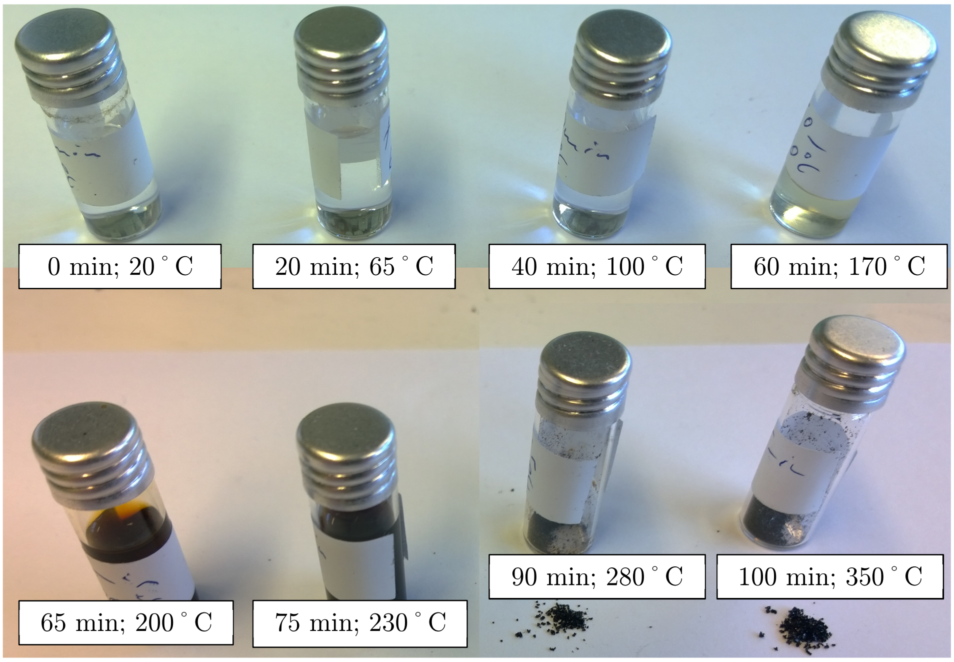

Fig. 47 Image of the taken samples during the thermal carbonization of glucose

FTIR spectroscopy was used to gain insights to the general progression of the reaction (**Fig. 48**). The -OH vibration at ~3300 cm^{-1} can be attributed to the water as well as the hydroxy functions of the glucose. The -OH band diminished with longer reaction times and vanished at t_{100min}, indicating a conversion of the glucose molecule and progressing dehydration. The C-C chain vibration at ~3000 cm^{-1} stayed constant throughout the tested temperature regime and a high amount of saturated carbon groups can be expected at the beginning of the carbonization. The carbonyl function (C=O) at ~1600 cm^{-1} is also visible for the glucose molecule itself (aldehyde and keto function in glucose and fructose respectively) and a sharp increase in intensity is observed to t_{100min}. This can be attributed to an incorporation of carbonyl functions into the carbon framework. The vibration band around 1500 cm^{-1} speaks for an aromatic function. This shows that the formed carbon already has aromatic regions at temperatures of 350 ° C.

Similar observations were independently made by Wohlgemuth[149], Falco[140], and Fellinger[135] for HTC carbons which shows that the reaction, even though not done under hydrothermal conditions, follows a comparable carbonization mechanism.

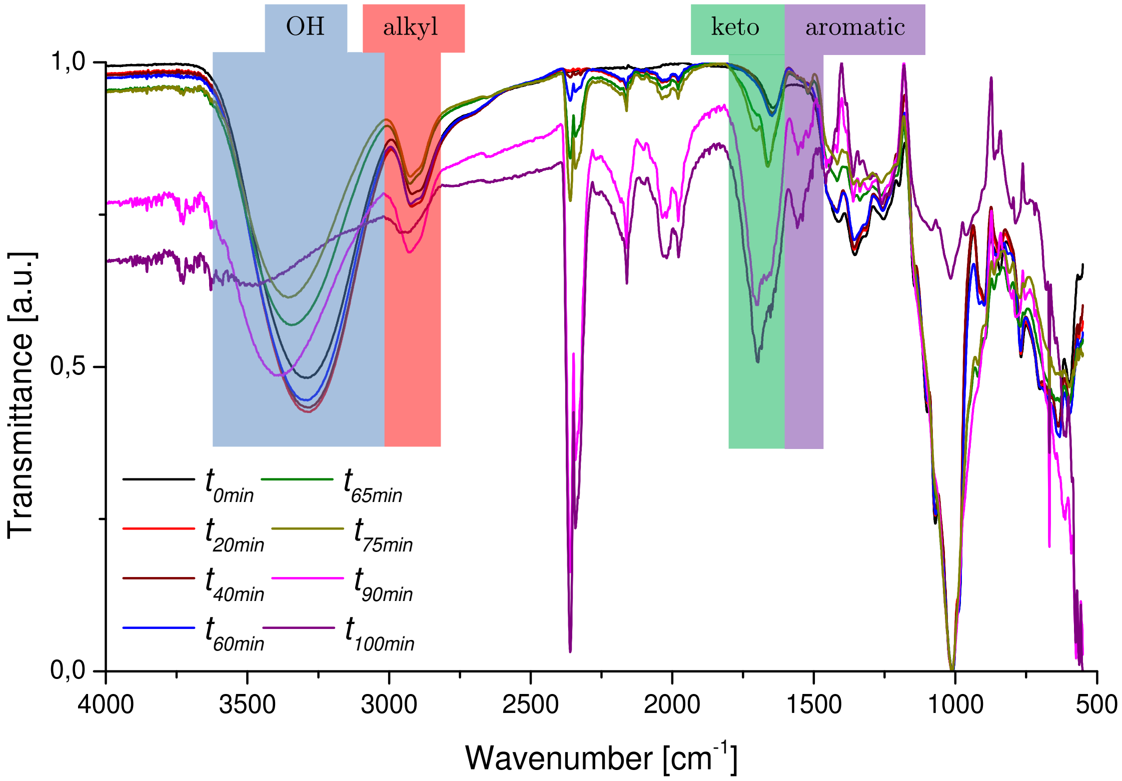

Fig. 48 FTIR-spectrum for samples taken at different times

The NMR spectra of the sample at $t = 65$ min showed a multitude of signals (**Fig. 49 bottom**). In order to get an idea about the composition HMF was used as a reference substance (**Fig. 49 top**). HMF showed signals for the aldehyde function (9.5 ppm), the (H)O-CH2- group (4.7 ppm), and two doublets for the furanic hydrogen atoms (7.5 and 6.7 ppm). The aldehyde and furan signals were also found in the sample taken after 65 min but the (H)O-CH2- signal was strongly overlapped by other signals. Nonetheless, the HMF formation was shown to take place during the reaction and a mechanism comparable to the HTC process can be expected. The samples taken before 65 min did not show any signals assignable to HMF.

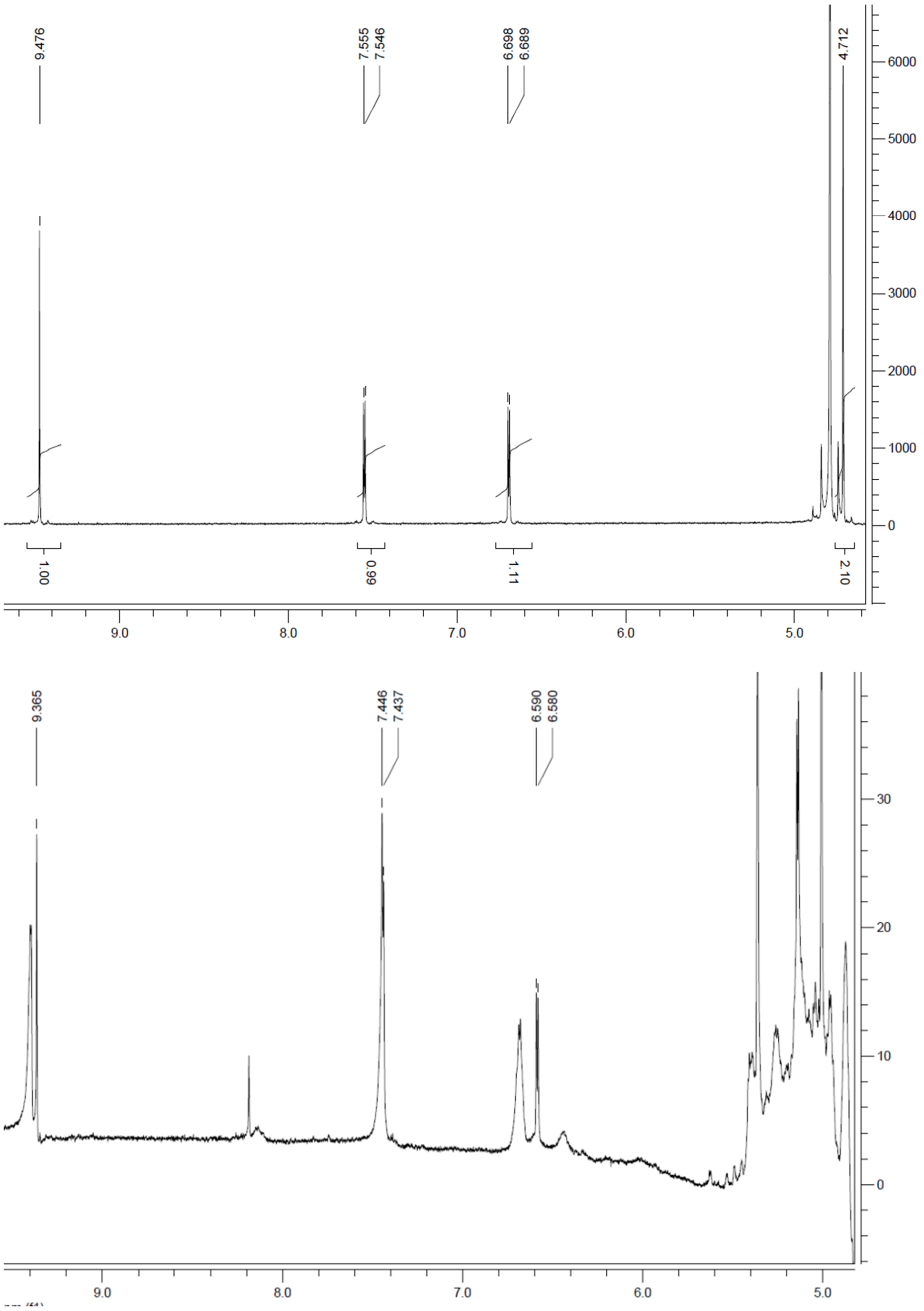

Fig. 49 Top: Reference NMR spectra for HMF
Bottom: Sample after 65 min

2.2 Heteroatom Doping of Ionothermal Derived Carbons

The carbonization of glucose proceeding over HMF can be subject to side reactions with additives. For the sulfur doping 2-**t**hiophene**c**arboxylic **a**cid (**TCA**) was used which can potentially form ester bonds with the hydroxyl function of HMF or undergo a [4+2] cycloaddition. Glucosamine was used as a cheap nitrogen source. Glucosamine is industrially derived from chitin and can be carbonized in a similar fashion to glucose[150]. The samples were produced with a carbohydrate to $ZnCl_2$ ratio of 1:1 and 1:5 and will be depicted as TC_ratio_temperature_heteroatom, e.g. TC_15_1000_N.

The incorporation of nitrogen and/or sulfur into the carbon lattice via glucosamine and TCA was evaluated by means of EA (**Table 6**; p. 64). The glucosamine precursor gave rise to high values of nitrogen doping of up to 6.7 wt.% for TC_15_800_N. The amount of nitrogen is depending on the carbonization temperature and is decreasing with increasing temperature. A similar trend can be observed for sulfur with the highest amount of 2 wt.% at 800 ° C. In general, a doping with sulfur is more likely to give lower doping levels compared to nitrogen. The van-der-Waals radius of sulfur is 180 pm and only 155 pm for graphite which makes it a poor guest in the graphite host lattice. Therefore a loss of sulfur is very likely at elevated temperatures. The co-doping of sulfur and nitrogen was successful and showed a similar behavior with comparable values for nitrogen and slightly lower values for sulfur compared to the single doped samples.

The EA for the nitrogen and nitrogen/sulfur co-doped samples showed a carbon content of around 80 wt.% whereas the sulfur doped samples gave values closer to the non-doped carbons (see also **Table 5**, p. 56). It can be assumed that a residual amount of $ZnCl_2$ remains in the samples. The XRD pattern did not reveal any peaks indicating an absence of crystalline particles. The encapsulation of $ZnCl_2$ cluster is most likely to take place accompanied by the formation of amorphous $ZnCl_2$ and ZnO. Nitrogen is known to complex zinc species, hence a complexation between surface nitrogen and $ZnCl_2$ can take place during the carbonization. This explains the lower carbon content and the absence of XRD peaks.

The thermo gravimetric analysis (TGA) also showed a higher residual mass for the nitrogen and the nitrogen/sulfur doped samples with around 11 wt.% for TC_11_1000_N and 6 wt.% for TC_11_1000_NS (**Fig. 50**). The carbon samples without nitrogen doping showed a lower residual mass of around 2 wt.% which confirms the assumption that nitrogen can act as a complexation agent for zinc species.

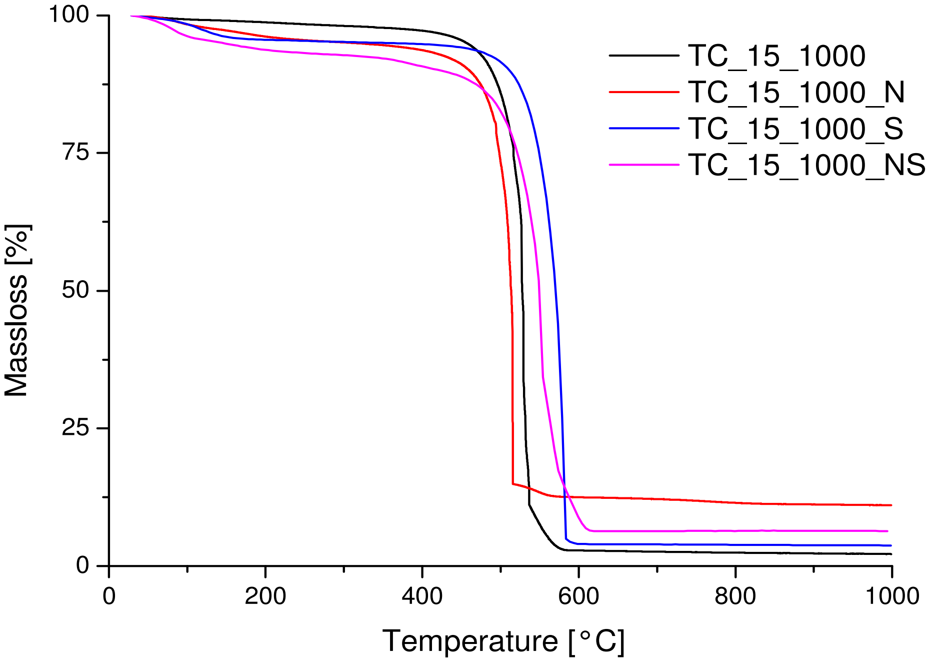

Fig. 50 TGA for various carbon materials synthesized at 1000 ° C with nitrogen, sulfur and nitrogen/sulfur co-doping. Heating rate: 10 K min^{-1}

The morphology of the samples was unaffected by the doping (**Fig. 51**). The carbohydrate to zinc chloride ratio is the determining factor and a lower ratio of 1:1 gives rise to a dense microporous material whereas a 1:5 ratio leads to mesoporous carbons. It has to be mentioned that the herein presented solution based bottom-up process leads to an agglomerate of small primary particles. In contrast, a classical chemical activation of coconut shells with $ZnCl_2$ results in bigger particles or continuous structures and no aerogel-like morphologies are obtained[151-153].

The carbons derived for a 1:5 ratio with sulfur and nitrogen/sulfur doping showed a deviation from the solely nitrogen doped samples. The sulfur doping led to bigger interparticle voids which resulted in higher pore volumes for the S and NS samples. Where TC_15_1000_N gave a V_{total} of 0.83 $cm^3\ g^{-1}$ a pore volume of 1.19 $cm^3\ g^{-1}$ and 1.03 $cm^3\ g^{-1}$ was measured for TC_15_1000_S and TC_15_1000_NS respectively (**Table 6**). This trend remained throughout the examined temperature range. The incorporation of TCA into the carbon material can cause a negative surface charge originated by the carboxy function and therefore leading to a different nucleation. Furthermore, a rupture can occur during the carbonization caused by the decay of TCA and a possible decarboxylation (formation of CO_2) would further widen the pores by a physical activation.

In general, a lower pore volume was observed for the doped samples as compared to the non-doped carbons. The sulfur doped samples showed higher pore volumes than the nitrogen and nitrogen/sulfur co-doped samples which can be explained by the higher residual amount of zinc. The residual zinc contributes to the overall mass, and the coordination of zinc to nitrogen might lead to a blocking of pores.

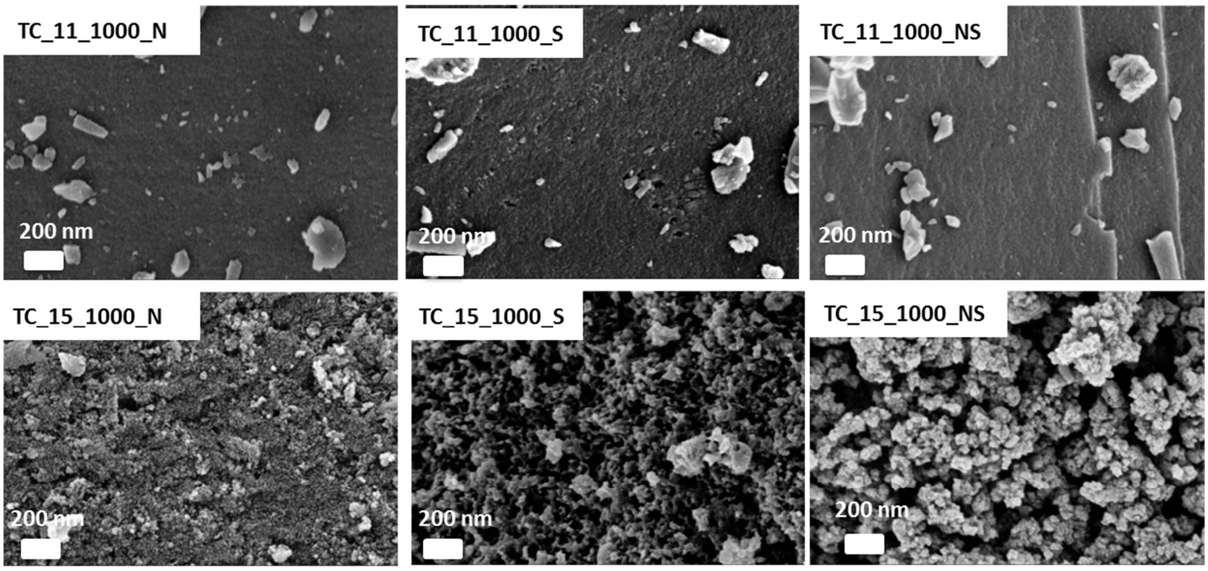

Fig. 51 SEM images of N, S and NS doped samples carbonized at 1000 ° C

The HRTEM investigation of the nitrogen doped carbon sample TC_15_900_N revealed an amorphous carbon structure (**Fig. 52 right**)[1]. The nitrogen doping did not affect the carbon synthesis. Also here an amorphous nature of the carbon was observed and the microscopic structure is similar to those observed for the non-doped carbons before. The nitrogen doping was further investigated by HRTEM coupled with electron energy loss spectroscopy (EELS) (**Fig. 52 left**). EELS spectra have been taken at four different points of the shown section. The measured nitrogen content was as high as 5.2, 5.4, 5.8, and 6.2 wt.% at position 1, 2, 3, and 4 respectively. The nitrogen was evenly distributed over the carbon matrix which was achieved by the solution based synthesis. This finding, in combination with the spherical shaped primary particles observed in the SEM images, speaks for a bottom up sol gel process. The heteroatom doping occurs on a molecular level during the synthesis and sulfur and nitrogen are incorporated into the growing carbon structure.

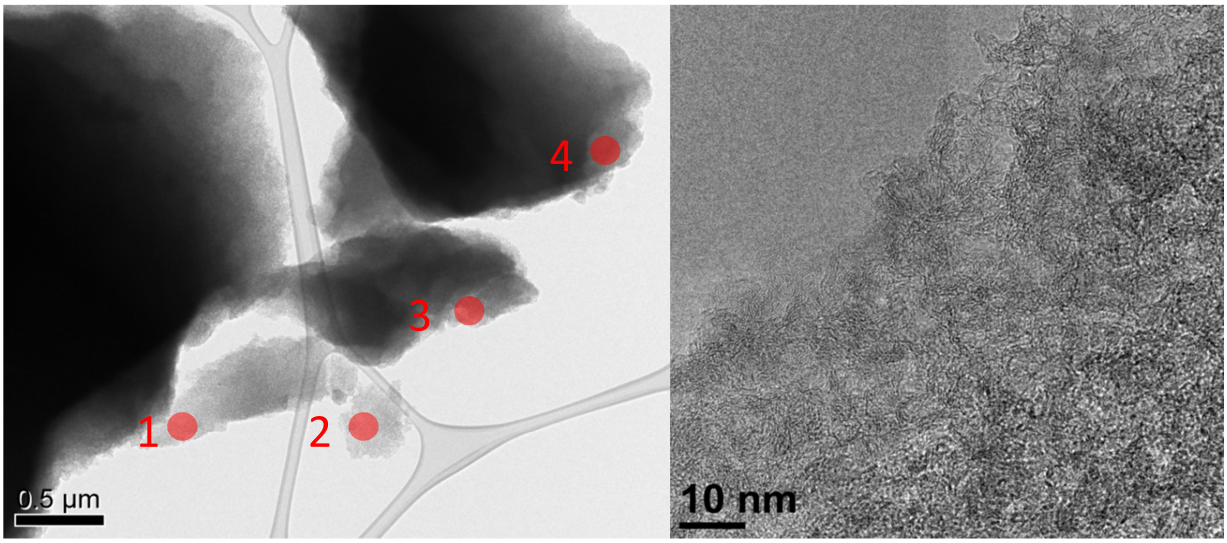

Fig. 52 Left: HRTEM image with indication of EELS spectra locations;
N-content [wt.%]: 5.2 (1), 5.4 (2), 5.8 (3) and 6.2 (4)

Right: HRTEM image of TC_15_900_N

---

[1] Guylhaine Clavel is highly acknowledged for the time consuming HRTEM measurements and especially for the EELS spectra.

Table 6 Summary of N_2 sorption values with total and microporous surface area and total pore volume and EA for N, S and NS doped carbon samples

Sample	N [wt.%]	S [wt.%]	C [wt.%]	H [wt.%]	S_{total} [m^{2}g^{-1}]	S_{micro} [m^{2}g^{-1}]	V_{total} [cm^{3}g^{-1}]
TC_11_1000_N	4.3	n/a	79.0	2.9	950	830	0.43
TC_15_1000_N	4.5	n/a	80.5	1.7	1207	617	0.83
TC_11_900_N	5.4	n/a	77.1	2.9	1147	1000	0.52
TC_15_900_N	5.6	n/a	80.0	2.0	1051	413	0.98
TC_11_800_N	6.5	n/a	80.,1	3.5	1092	964	0.52
TC_15_800_N	6.7	n/a	81.5	2.2	1091	397	1.08
TC_11_1000_S	n/a	1.6	93.0	1.6	1143	926	0.54
TC_15_1000_S	n/a	1.5	94.5	1.4	1505	757	1.19
TC_11_900_S	n/a	2.0	92.1	1.6	1101	937	0.53
TC_15_900_S	n/a	2.0	93.0	1.5	1344	505	1.79
TC_11_800_S	n/a	2.3	89.1	1.8	1281	1026	0.66
TC_15_800_S	n/a	2.5	87.5	1.7	1357	603	1.07
TC_11_1000_NS	4.3	1.2	78.0	3.0	1189	1079	0.49
TC_15_1000_NS	4.8	1.3	79.5	2.1	1132	443	1.03
TC_11_900_NS	5.2	1.5	78.1	2.9	1164	1119	0.46
TC_15_900_NS	5.7	1.5	82.0	2.0	1212	475	1.09
TC_11_800_NS	5.3	1.9	76.1	2.7	1019	887	0.47
TC_15_800_NS	6.5	1.8	82.5	2.0	1165	414	1.17

2.3 Zinc Chloride and Cesium Acetate as a Binary Salt Template

The use of a binary salt template can be very attractive, if both salts contributed to the overall surface area of the carbon and ideally develop pores independently. Cesium acetate was chosen as a secondary salt in combination with zinc chloride and glucosamine as a carbon and nitrogen source. The samples will be denoted as before but with a three digit ratio (glucosamine:$ZnCl_2$:CsAc), e.g. TC_111_900_N.

The obtained surface area for the exclusive use of CsAc was strongly depending on the carbohydrate to salt ratio. TC_101_900_N only gave a specific surface area of 12 m^2 g^{-1} whereas a higher CsAc fraction in TC_105_900_N showed a tremendous increase to 2602 m^2 g^{-1} with a contribution from micropores of 1405 m^2 g^{-1}. The material is highly microporous with an additional hierarchically PSD. The incorporated CsAc will undergo thermal decay accompanied by the formation of Cs_2O and CO_2 (possible physical activation of the carbon material). The filtrate after aqueous washing of the carbon samples showed a basic pH. The samples were therefore washed until neutral to ensure complete removal of residual Cs_2O.

The binary systems of $ZnCl_2$ and CsAc proofed to be beneficial in developing higher pore volumes and specific surface areas than the samples with only $ZnCl_2$ as template. Carbons derived from 1:1 ratio of $ZnCl_2$ and glucosamine with the addition of CsAc showed an increase of surface area from 1147 m^2 g^{-1} to 2513 m^2 g^{-1} for TC_115_900_N (**Fig. 53 a, b**). Compared to TC_105_900_N a slight decrease in surface area was observed. However, the N_2 isotherms showed a rapid uptake at a high relative pressure for TC_115_900_N indicating the development of macroporosity. This pore structure can be beneficial for SC devices since the larger pores should allow for an improved ion diffusion to the smaller pores. The samples produced with a 1:5 ratio of $ZnCl_2$ also showed an improved behavior with the addition of CsAc. The sample TC_15_900_N showed a type IV isotherm with a H2 hysteresis loop and a pore volume of 0.98 cm^3g^{-1} with a mesopore volume contribution of 0.81 cm^3 g^{-1} (**Fig. 53 a, d**). With the addition of CsAc (TC_151_900_N), the total pore volume increased to 1.42 cm^3g^{-1} and the mesopore fraction was measured to be 1.13 cm^3 g^{-1}. The increase in mesoporosity is also visible by a widening of the H2 hysteresis loop. The PSD itself was not affected by the CsAc and showed the same distribution as with the solely $ZnCl_2$ derived samples but with an increase in microporosity. The higher pore volume can be positive for an increased sulfur loading in lithium sulfur batteries.

The elemental analysis for the samples derived with a low glucosamine to cesium acetate ratio showed a nitrogen contented of about 6 wt.% which is roughly the same as for the carbons derived from glucosamine and zinc chloride. With an increase of cesium acetate to a 1:5 ratio the nitrogen content dropped to around 1 wt.%. This shows that the overall carbon contribution by cesium acetate is significant.

Kang Ko Chung *et. al.* demonstrated the use of CsAc as a porogen and solvent for the carbonization of acrodam with surface areas up to 2400 m^2 g^{-1}[154]. A similar dependence concerning the nitrogen content and CsAc to precursor ratio was shown which shows that the observed effect is not limited to a certain precursor.

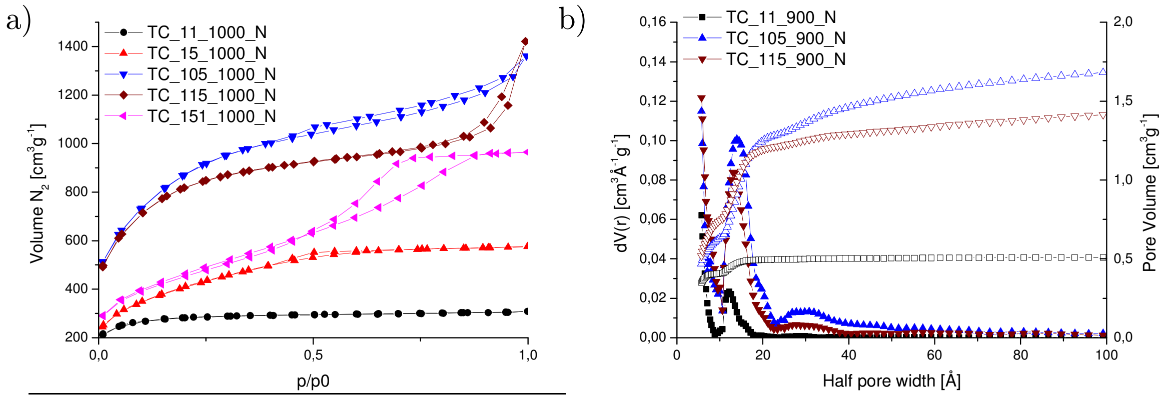

c)

Sample	S_{total} [m^{2}g^{-1}]	S_{micro} [m^{2}g^{-1}]	V_{total} [cm^{3}g^{-1}]	V_{meso} [cm^{3}g^{-1}]
TC_11_900_N	1147	1000	0.52	0.11
TC_15_900_N	1051	413	0.98	0.81
TC_105_900_N	2602	1405	1.85	1.22
TC_115_900_N	2513	1664	1.74	1.00
TC_151_900_N	1507	701	1.42	1.13

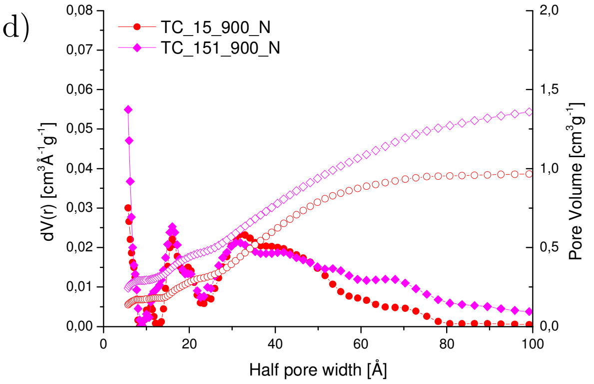

Fig. 53 a) N_2 isotherms for carbons derived from solely $ZnCl_2$ or CsAc and mixtures of both
b) PSD for carbons with 1:1 ratio between glucosamine and $ZnCl_2$ and mixture with CsAc
c) Table of surface area and pore volume for single and binary salt templates
d) PSD for samples with a 1:5 ratio between glucosamine and $ZnCl_2$ and additional CsAc

3 Supercapacitor Performance

3.1 Evaluation in 1 M Sulfuric Acid

For a quick performance comparison of the various doped and non-doped carbon samples, the corresponding Ragone plots are shown in **Fig. 54**. It can be seen that the mesoporous samples had a better performance at higher current densities. Furthermore, the performance for the array of nitrogen doped samples was better compared to the samples with sulfur doping or nitrogen/sulfur co-doping. The loss in energy density was lower and even comparable between meso- and microporous N-doped carbons. The highest energy density of 30 Wh kg^{-1} was observed for both TC_15_900 and TC_15_800_N but where TC_15_800_N retained 15 Wh kg^{-1} at 20 A g^{-1}, TC_15_900 showed a drop to 11 Wh kg^{-1}. However, the performance of the non-doped carbons was comparable to the nitrogen doped samples for a high synthesis temperature of 1000 °C. The N-doping was more beneficial, in case of lower synthesis temperatures.

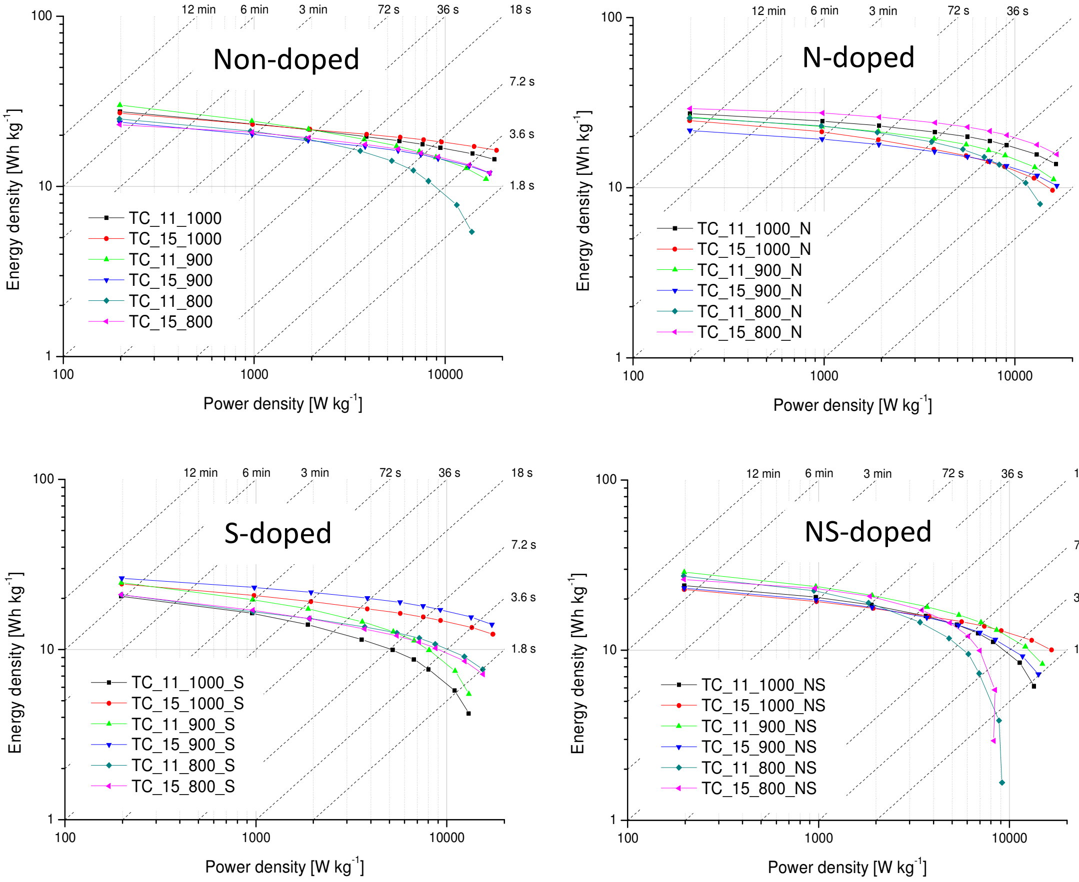

Fig. 54 Ragone plots for non-doped and doped carbon samples

In order to understand the effect of the different heteroatom dopings on the carbon framework, the relaxation time constants and ESRs were compared (**Fig. 55**). In general, the microporous carbons showed higher values for τ_0 compared to the mesoporous samples. Mesopores can be accessed much faster by the electrolyte ions than narrow micropores. Furthermore, a dependence on the synthesis temperature was observed. The increase in τ_0 was true for all samples and can be attributed to the overall conductivity of the samples since the PSD was not changing with temperature. The relaxation time for the mesoporous non-doped samples was very fast and reached the minimum for TC_15_1000 with only 0.6 s. The microporous carbons showed a rapid increase of τ_0 from 900 °C to 800 °C with the exception of the nitrogen doped samples. The incorporation of nitrogen into the carbon lattice proofed to be beneficial for a faster relaxation time constant. Furthermore, the ESR stayed more constant and was below 8 Ω even at a low synthesis temperature of 800 °C whereas the other carbons showed a higher resistance of up to 13 Ω at the same synthesis temperature of 800 °C. The amount of oxygen is increasing with decreasing temperature which results in a lower conductivity. The nitrogen, on the other hand can enhance the conductivity and will replace partially oxygen atoms in the carbon lattice. The low τ_0 in combination with a low ESR makes the nitrogen doping attractive for carbons synthesized at lower temperatures. For a high temperature synthesis the beneficial effect becomes less dominant compared to a simple non-doped carbon.

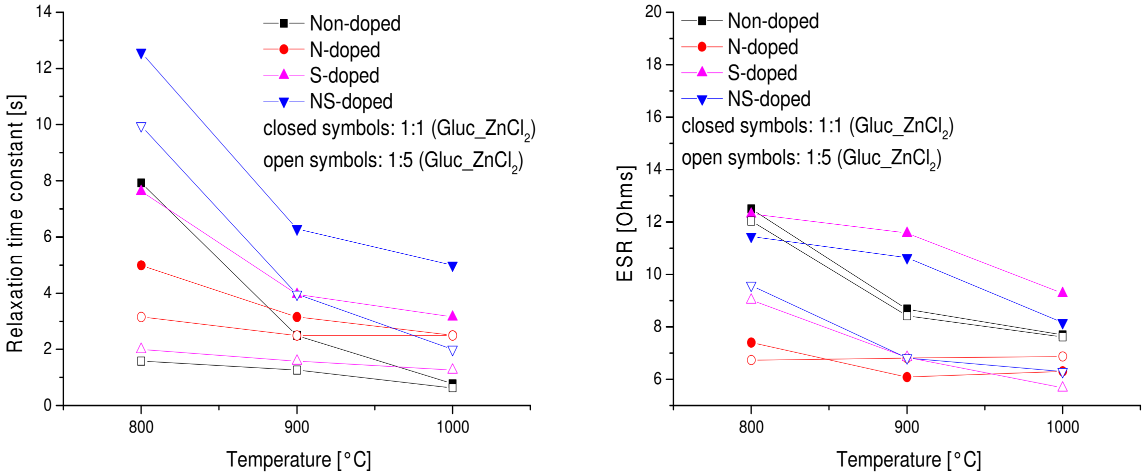

Fig. 55 Left: Relaxation time constant for all carbon samples derived at 800, 900 and 1000 °C
Right: ESR for all carbon samples derived at 800, 900 and 1000 °C taken at 0.2 A g^{-1}

The representation of the specific capacitance over the total surface area (**Fig. 56 left**) as well as over the microporous surface area (**Fig. 56 right**) gave no visible dependency. In general, nitrogen or oxygen functions, if located at the surface area, can contribute to the overall pseudocapacitance. The doping with nitrogen did not increase the capacitance beyond the capacitance already achieved for non-doped samples. It was shown in various works that an increase in nitrogen content is often leading to a higher capacitance but a direct comparison with non-doped samples is usually not made[155-157]. Even though nitrogen is contributing to the pseudocapacitance other heteroatoms will do so as well and oxygen functions might have the same impact as nitrogen functions.

On the other hand, the nitrogen located in the bulk material was beneficial for a lower, and synthesis temperature stable, ESR. This shows that the common believe that nitrogen is increasing the total capacitance by an additional pseudocapacitance might not be completely true. Rather is the combination of a pseudocapacitance and a lower ESR leading to a better high current behavior for nitrogen doped carbons produced at lower temperatures. On the other hand, the sulfur and oxygen containing samples gave similar values as the nitrogen doped carbons, if derived at higher carbonization temperatures showing that nitrogen functions are not superior over oxygen functions in terms of redox activity and thus pseudocapacitance.

Even though the results obtained for the doped and non-doped carbon samples in this work do not indicate an enhanced capacitance with higher nitrogen content, a generalization is not possible. A thorough study with various nitrogen doped carbons in conjunction with XPS may help to understand the storage mechanism more clearly but is still missing.

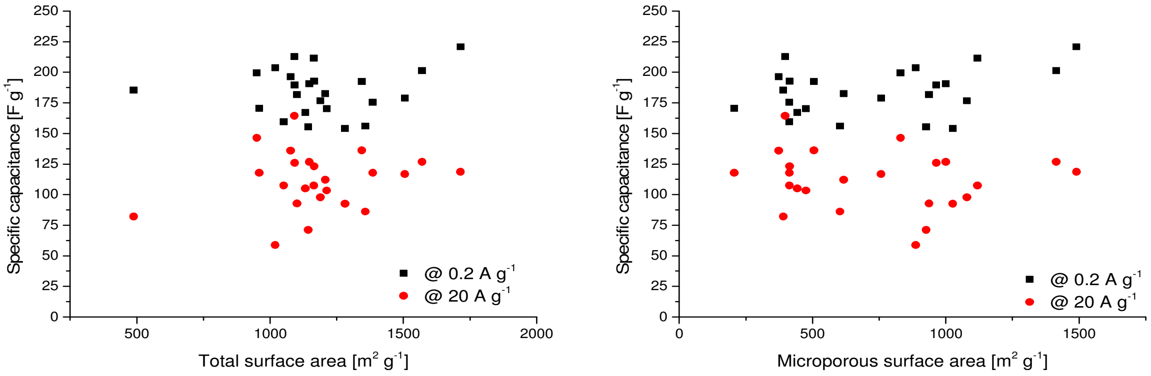

Fig. 56 Left: Specific capacitance taken at 0.2 and 20 A g-1 vs. mesoporous surface area
Right: Specific capacitance taken at 0.2 and 20 A g-1 vs. microporous surface area

3.2 Evaluation in [EMIM][BF_4]

For the tests in [EMIM][BF_4], the mesoporous samples derived at 900 °C with nitrogen, sulfur, and nitrogen/sulfur doping have been selected. Due to the size of the imidazolium cation, the use of carbons with bigger pores is more suitable than microporous carbons.

The CC test revealed a high capacitance of 152 F g^{-1} for TC_15_900_S at 0.25 A g^{-1} followed by a rapid decrease to 93 F g^{-1} at 2 A g^{-1} (61% retention) (**Fig. 57 left**). The non-doped carbon and the nitrogen doped sample showed a more moderate decrease to 74% and 70% of their initial capacitance respectively. On the other hand, the initial capacitance was about 40 F g^{-1} lower than that for TC_15_900_S. The co-doped carbon showed a capacitance behavior close to that of the purely sulfur doped carbon but with a lower initial capacitance. The better capacitance retention for the nitrogen and non-doped carbon sample hints to a higher conductivity of those carbons. Furthermore, the pore structure might be better suited for the ions of the ionic liquid. It was demonstrated by Marcilla *et. al* that carbons with pores close to the ion size of the IL give higher capacitances and show a better capacitance retention[158]. From the Ragone plot, a high loss in energy density is visible for the TC_15_900_S from 180 Wh kg^{-1} to 41 Wh kg^{-1} further speaking for a low conductivity (**Fig. 57 right**). The decrease for TC_15_900_NS is much more pronounced and only 0.5 Wh kg^{-1} were measured at 2 A g^{-1} which speaks for a very high ESR. The co-doping of nitrogen and sulfur is not beneficial in terms of combining an enhanced conductivity with a higher accessible surface area.

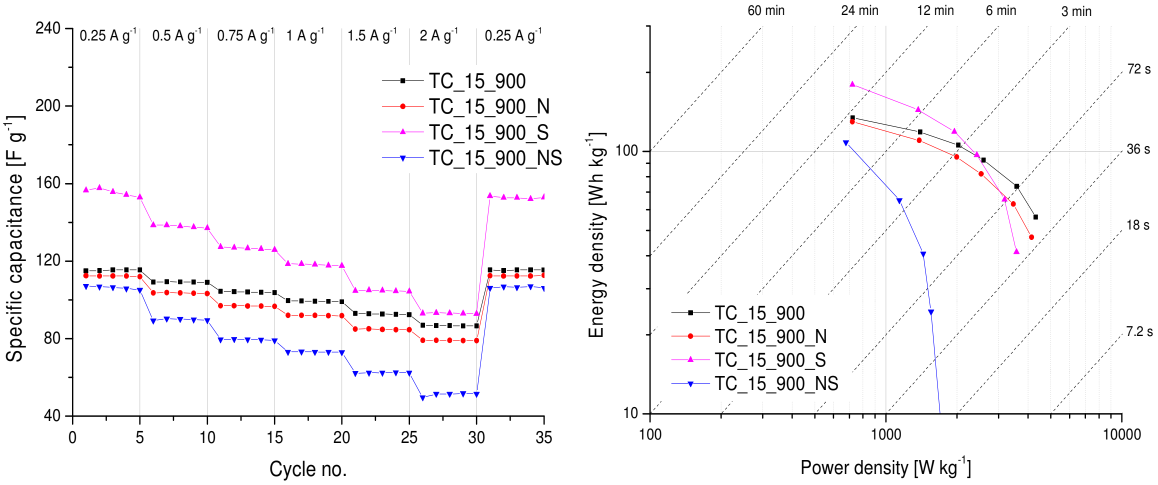

Fig. 57 Left: CC results for increasing current densities from 0.25 to 2 A g^{-1} (ΔU: 3 V)
Right: Ragone plot for non-doped and doped mesoporous carbons

The ESR is much higher than the values measured in acidic medium due to the lower conductivity of [EMIM][BF_4] compared to sulfuric acid (**Fig. 58 left**). Nonetheless, the total ESR will be a combination of the conductivity of the electrolyte and the active material. The ESR was constant over the tested range of current densities in contrast to the high dependency measured in sulfuric acid so far. This can be explained by the complete electrolytic nature of ILs which leads to a better mass transport. If the active surface area stays constant even at elevated current densities, no change in ESR will be observed. The ESR for TC_15_900, TC_15_900_N, and TC_15_900_S is with 75, 110, and 133 **Ω** much smaller than the 300 **Ω** measured for TC_15_900_NS. The high ESR will cause a significant voltage drop at higher current densities which in turn lowers the capacitance and energy density significantly (**Fig. 58 right**). The IR drop at 0.25 A g^{-1} is around 340 mV for TC_15_900_NS whereas the other carbons demonstrated a moderate loss of ca. 125 mV. At a current density of 1 A g^{-1} already 1.46 V are lost due to the high ESR of TC_15_900_NS. A voltage loss of 50% translates into an energy loss of 75% (Eq.(7)) which was confirmed during the CC test (**Fig. 57 right**). The other carbon materials showed a behavior according to their measured ESR and the low difference in series resistance had a more pronounced impact at 1 A g^{-1} where the IR-drop was 0.41, 0.47, and 0.59 V for TC_15_900, TC_15_900_N, and TC_15_900_S respectively. The loss in performance for TC_15_900_S was due to its slightly higher ESR compared to the non-doped and nitrogen doped sample.

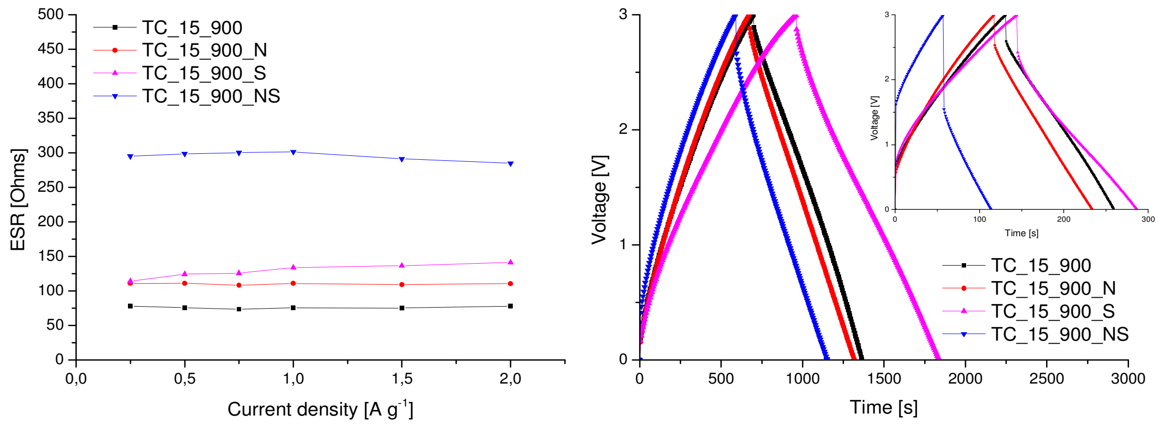

Fig. 58 Left: Evolution of the ESR with increasing current densities
Right: Voltage profile at 0.25 A g^{-1} and 1 A g^{-1} (inset)

The behavior observed by the experiments at constant current was confirmed by the impedance study of the carbon samples (**Fig. 59 left**). A large charge transfer resistance of 160 Ω was measured for TC_15_900_NS which can originate from a low interaction between the IL and the carbon material. The high R_{ct} reflects in a poor frequency behavior and a low slope was observed for TC_15_900_NS (**Fig. 59 right**). On the other hand, TC_15_900_N and TC_15_900_S showed a better frequency response and a relaxation time constant of 50 s was measured whereas TC_15_900_NS showed no maximum for C'' in the measured frequency range (0.01 Hz to 1 MHz). The maximum capacitance is therefore only reached at very low frequencies in turn long charging times. The loss in performance for TC_15_900_S at higher current densities cannot be explained by an unfavorable pore structure which would give a higher τ_0 compared to the nitrogen and non-doped sample. Hence the higher ESR is the main factor contributing to the capacitance behavior as observed before. In general, the use of IL as electrolyte is more suited at lower current densities where high energy densities can be reached. Nonetheless, the maximum energy density of 180 Wh kg^{-1} observed for TC_15_900_S was reached in only 15 min charging time which is much faster than comparable battery systems where charging times of 1 h and more are usually required[159].

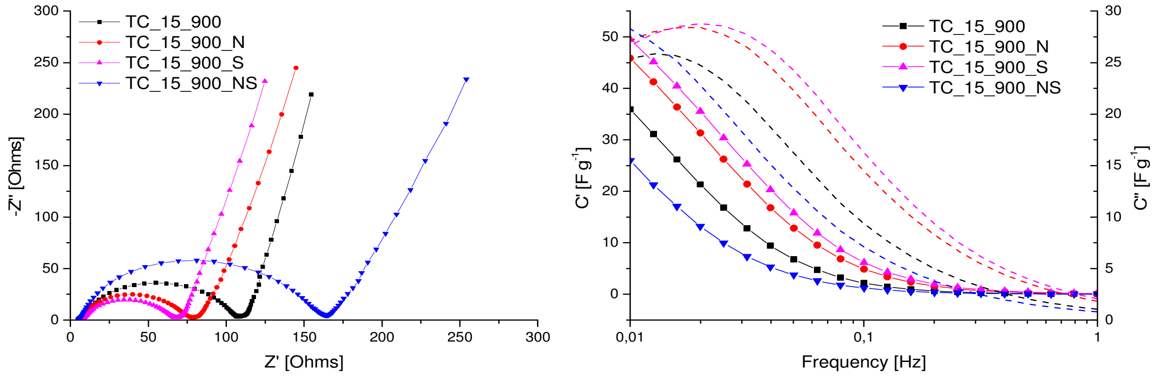

Fig. 59 Left: Nyquist plot for the different doped carbons
Right: Bode diagramm with real (scattered) and imaginary (dotted) capacitance

3.3 Evaluation of Carbons Derived From the Binary Salt System Zinc Chloride and Cesium Acetate

The porous carbons presented in **chapter C 2.3** have been evaluated as possible active materials in supercapacitors. From the cyclic voltammetry tests, a low capacitance of 117 F g^{-1} was measured for TC_101_900_N followed by a rapid decrease to 20 F g^{-1} which is in accordance with the rather low surface area of 12 m^2 g^{-1} (**Fig. 60 left**). With an increase in CsAc during the synthesis, much higher surface areas were obtained which resulted in a higher capacitance. TC_105_900_N showed a capacitance of 242 F g^{-1} and the highest specific capacitance was recorded for TC_115_900_N with impressive 300 F g^{-1}. The combination of CsAc with $ZnCl_2$ was very beneficial in developing a hierarchical pore structure which allows for a fast ion diffusion. The capacitance retention at 200 mV s^{-1} was still 63% for TC_115_900_N further speaking for an easily accessible pore structure by ion diffusion.

The cyclic voltammogram demonstrated an ideal rectangular shape for all samples with variations in the current response (**Fig. 60 right**). The carbon samples TC_105_900_N and TC_115_900_N showed a very fast response which can be attributed to a good conductivity and ion diffusion. Furthermore, a peak was observed for TC_105_900_N during the cyclic voltammetry. This speaks for a pseudocapacitive contribution to the overall capacitance of the porous carbons.

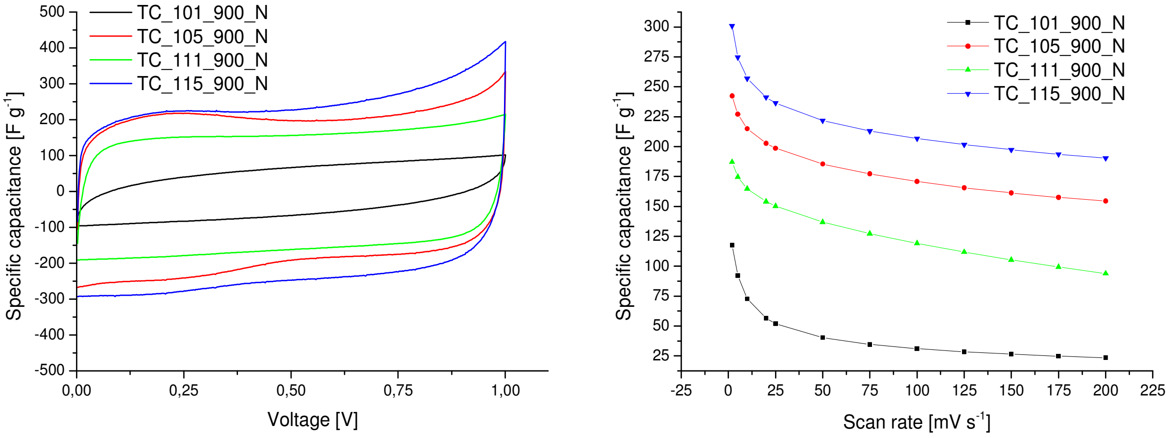

Fig. 60 Left: Cyclic voltammetry response at 20 mV s^{-1} for binary salt templated carbons
Right: Specific capacitance over scan rate for binary salt templated carbons

The constant current experiment confirmed the results from the cyclic voltammetry (**Fig. 61 left**). A high capacitance of 305 F g^{-1} was measured for TC_115_900_N and even at a high current density of 20 A g^{-1} still 196 F g^{-1} were recorded. The capacitance retention with 64% was roughly in the same range as during the cyclic voltammetry. The retention for TC_105_900_N and TC_111_900_N was 74% and 70% respectively. The capacitance loss from 0.2 A g^{-1} to 1 A g^{-1} was less pronounced resulting in a better capacitance retention. The initial capacitance of 216 F g^{-1} and 185 F g^{-1} for TC_105_900_N and TC_111_900_N respectively was much lower than the capacitance measured for TC_115_900_N. The capacitance for TC_101_900_N was quite low with 115 F g^{-1} and a rapid drop to 17 F g^{-1} was observed which reflects the low surface area.

From the Ragone plot, an almost vertical line is recorded for TC_115_900_N and TC_105_900_N with 42 Wh kg^{-1} and 28 Wh kg^{-1} respectively (**Fig. 61 right**). The high energy density was very stable for TC_115_900_N and still reached 24 Wh kg^{-1} at high current densities with a power density of 18 kW kg^{-1}. The addition of a small amount of $ZnCl_2$ is highly favorable for a better developed pore structure, e.g. transport pores with adjacent micropores. TC_111_900_N showed a deviating behavior from TC_115_900_N and TC_105_900_N which speaks for a less good ion diffusion into the carbon structure.

Similar high capacitances were observed by Kang Ko Chung *et. al.* for the CsAc acrodam system, in case of high fractions of CsAc[154].

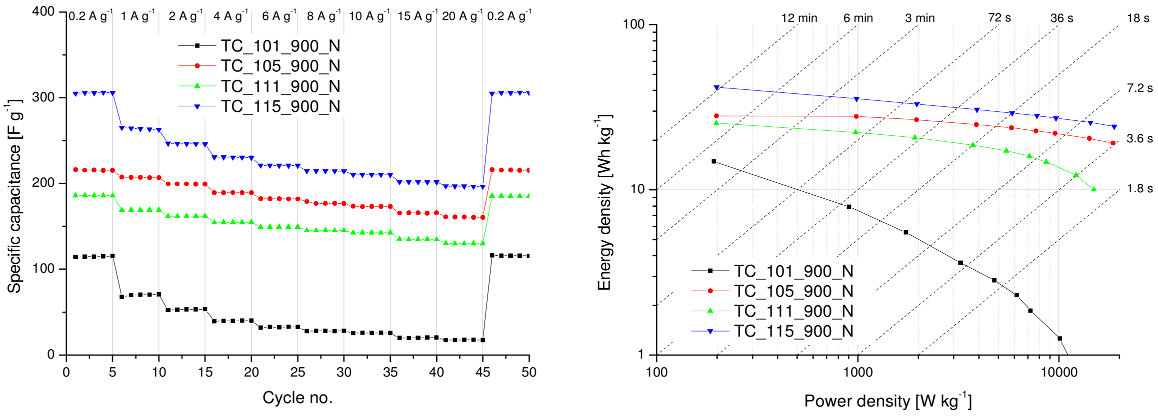

Fig. 61 Left: Specific capacitance with increasing current densities
Right: Ragone plote for binary salt templated carbons

The carbon materials demonstrated a quick transition into an ideal behavior during the EIS measurements (**Fig. 62 left**). TC_115_900_N and TC_111_900_N showed a similar Nyquist curve whereas TC_105_900_N showed a less steep slope. This demonstrates the importance of $ZnCl_2$ as an additional porogen for CsAc in developing an easily accessible pore structure. This finding was further confirmed by the representation of C' and C'' in the Bode diagram (**Fig. 62 right**). No maximum was observed for TC_101_900_N. The relaxation time constants for TC_111_900_N and TC_115_900_N were 1.26 s and 0.79 s respectively. TC_105_900_N, on the other hand, had a τ_0 of 3.97 s. This longer relaxation time can be attributed to a more sluggish ion diffusion into the porous carbon framework.

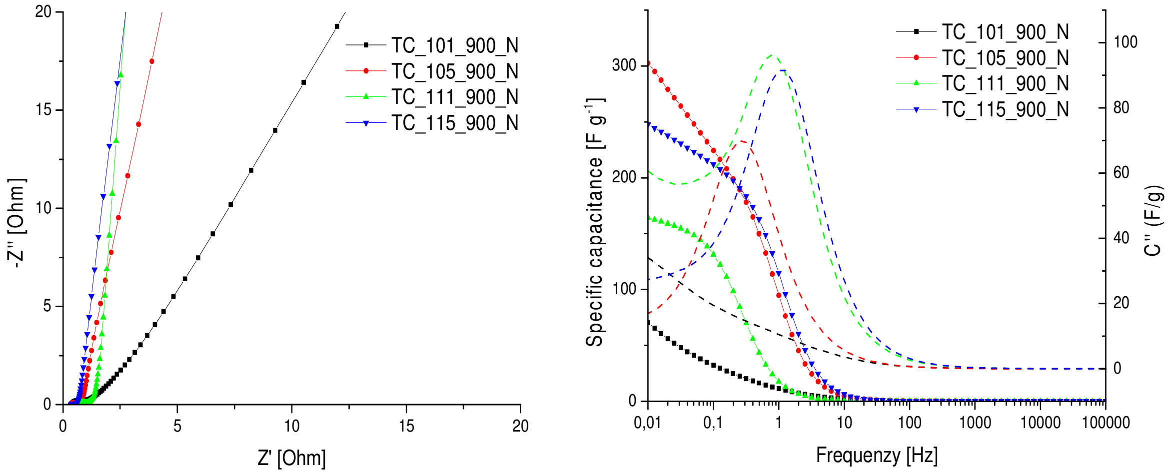

Fig. 62 Left: Nyquist diagram for binary salt templated carbons
Right: Bode diagramm with real (scattered) and imaginary (dotted) capacitance

Interestingly, the highest capacitance was observed for the samples derived at a high glucosamine to CsAc ratio. Those carbons only showed a nitrogen content of about 1 wt.% which is much smaller than the 6 wt.% observed for TC_111_900_N. This further confirms the observation made before - that an oxygen doping in amorphous carbons is comparable to a nitrogen doping in terms of pseudocapacitance. The increase in capacitance must originate from the larger surface area and thus larger electrochemical accessible surface area. This shows that the impact of a carefully controlled surface morphology can out weight a heteroatom doping.

Since the carbon sample TC_115_900_N showed good capacitive properties, further tests at very high current densities of 50 and 100 A g^{-1} were conducted (**Fig. 63 left**). The capacitance was still 196 and 180 F g^{-1} at 50 and 100 A g^{-1} respectively. TC_115_900_N demonstrated very good high rate capabilities and even at 100 A g^{-1} an energy density of 13 Wh kg^{-1} was measured. The power density was 72 kW kg^{-1} which translates into a charge or discharge time of a mere 0.65 s. This time is close to the relaxation time constant of 0.79 s which means that roughly 50% of the capacitance is still employed at a current density of 100 A g^{-1}.

The carbon material was also checked for its properties in [EMIM][BF_4] for a high voltage supercapacitor (**Fig. 63 right**). The capacitance was rather low with ca. 70 F g^{-1} at 0.25 A g^{-1} and showed a rapid decrease to 40 F g^{-1} at 2 A g^{-1}. The pore structure of the material is highly microporous which is not suited for the bulky IL [EMIM][BF_4]. Even though the carbon showed a very good behavior under aqueous conditions, a simple correlation to a non-aqueous medium is not possible.

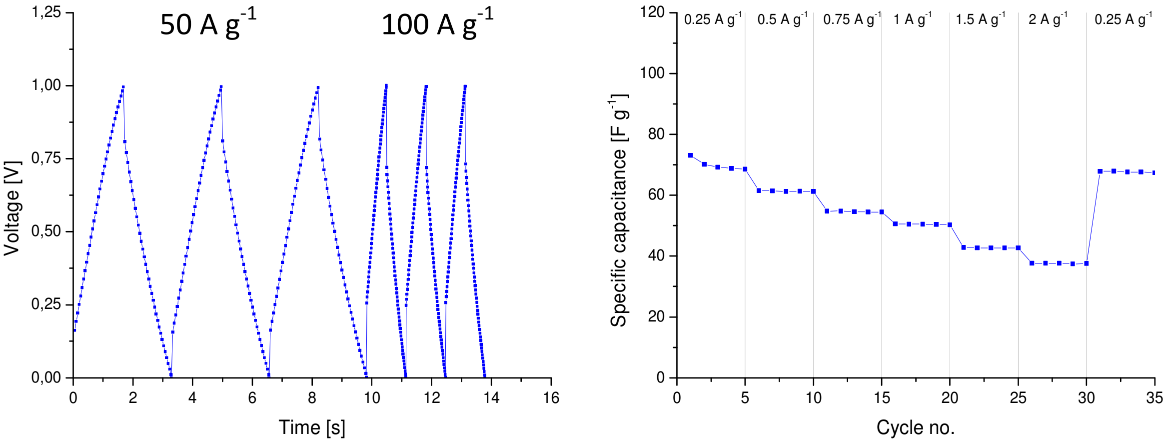

Fig. 63 Left: Voltage profile for TC_115_900_N at 50 and 100 A g^{-1} in 1 M H_2SO_4
Right: Specific capacitance at different current densities for TC_115_900_N in [EMIM][BF_4]

3.4 Evaluation in 1 M Sodium Chloride Solution

The microporous carbons synthesized at 900 ° C have been used for tests in 1 M sodium chloride solution in order to elucidate a possible correlation between SC performance and heteroatom doping[1]. It was demonstrated, in a theoretical and experimental way, by Presser *et. al.* that microporous carbons are better suited for capacitive deionization of sodium chloride solutions[160]. Since the CDI is essentially a capacitive process, a correlation to SC can be made and hence microporous samples have been selected.

The samples were cycled at different current densities from 0.3 A g^{-1} up to 10 A g^{-1} with exception of TC_105_900_N where the current densities are doubled. The voltage profiles showed an almost ideal behavior (**Fig. 64**). TC_105_900_N showed a deviation for the charge branch at 0.6 A g^{-1} but followed an ideal behavior for higher current densities. All investigated carbon samples demonstrated a moderate voltage drop of about 100 mV and 200 mV at 4 A g^{-1} and 10 A g^{-1} respectively.

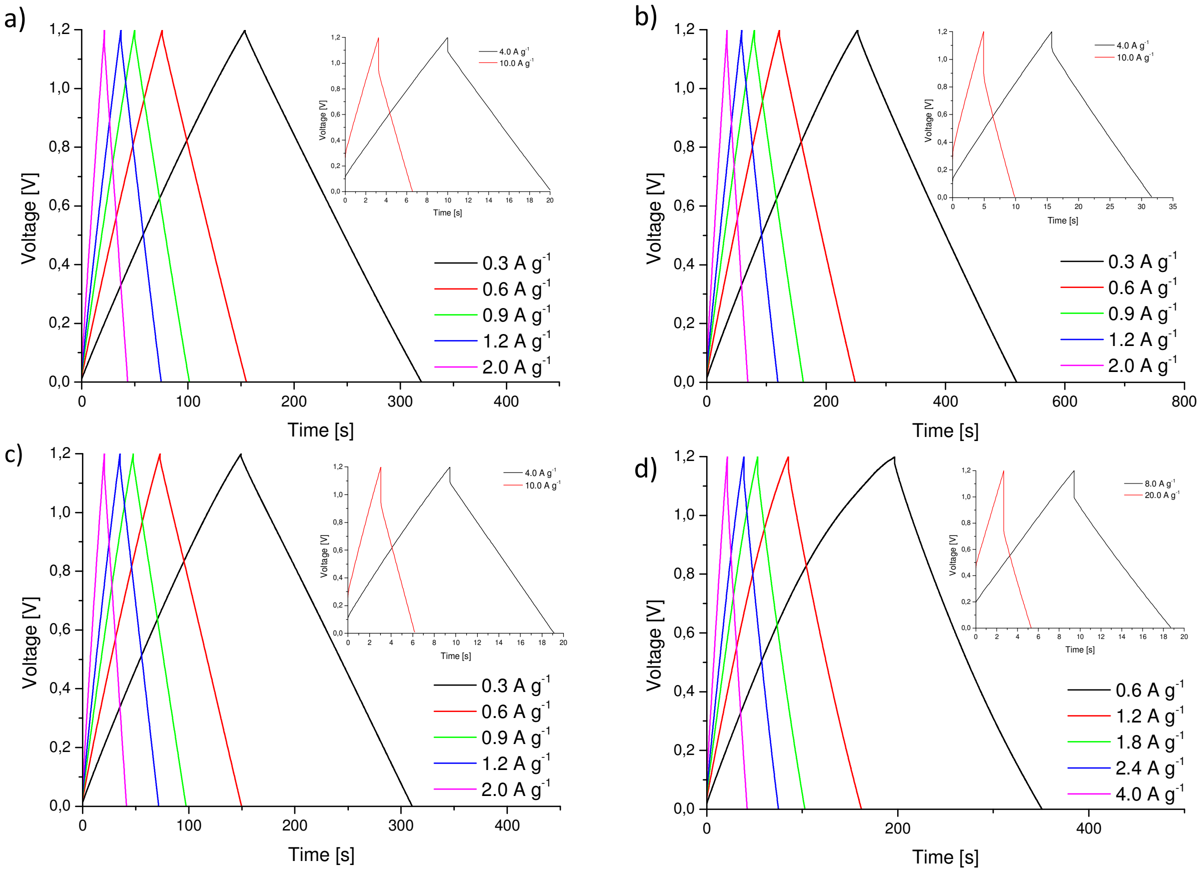

Fig. 64 Voltage profile at different current densities for TC_11_900(a), TC_11_900_N(b), TC_11_900_S(c) and TC_105_900_N(d)

---

[1] Gerard Sans Palacios (INM Leibniz; Saarbruecken, Germany) is highly acknowledged for conducting the SC tests in 1 M sodium chloride solution.

The capacitance was as high as 102, 90, and 84 F g^{-1} for TC_11_900_N, TC_11_900, and TC_11_900_S respectively (**Fig. 65 right**). The nitrogen doping seems to be beneficial for a higher capacitance, especially when taking into account that the specific surface area of TC_11_900_N is 1150 m^2 g^{-1} whereas TC_11_900 showed 1715 m^2 g^{-1}. Interestingly, the performance of TC_11_900 in 1 M sulfuric acid was much better than that of TC_11_900_N. A simple correlation between different electrolyte systems is not possible; rather have the carbons to be task specific. The capacitance of TC_105_900_N was 203 F g^{-1} which is an extremely high value under neutral conditions. Comparable studies of symmetrical SC conducted by Frackowiak and Beguin showed 180 F g^{-1}[161] and 140 F g^{-1}[162] respectively.

The high capacitance of TC_105_900_N leads to a high energy density of 40 Wh kg^{-1} with a good high current behavior up to 8 A g^{-1} (**Fig. 65 left**). For a current density of 20 A g^{-1}, a rapid loss in performance was observed and only 8 Wh kg^{-1} were delivered. Nonetheless, a power density of up to 10 kW kg^{-1} was achieved which is rather high considering the lower conductivity of the sodium chloride solution compared to sulfuric acid($\kappa_{1\,M\,NaCl}$: 74 mS cm^{-1}; $\kappa_{1\,M\,H2SO4}$: 366 mS cm^{-1}[163]).

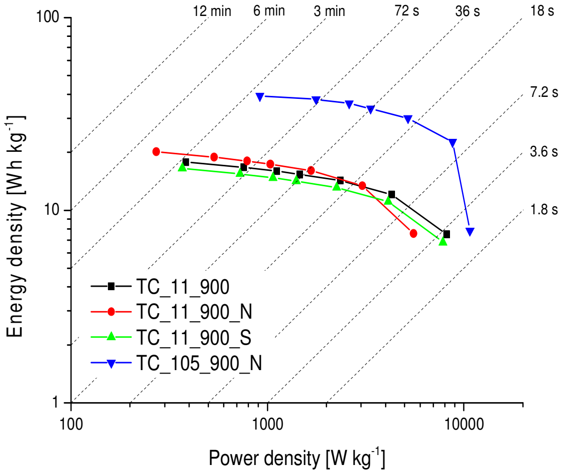

I [mA] C_{sp} [F g^{-1}]	15	100	200	500
TC_11_900	90	79	73	60
TC_11_900_N	102	89	81	63
TC_11_900_S	84	72	67	54
TC_105_900_N	203	182	163	115

Fig. 65 Left: Ragone plot for different heteroatom doped carbon samples
Right: Table with specific capacitane at different currents

4 Lithium Sulfur Battery Performance

4.1 Electrochemical Evaluation

The sample TC_15_1000 was infiltrated with sulfur by a melt infusion technique at 150 ° C with different sulfur loadings of 40, 50, 60, and 70 wt.% to get an idea about the maximum sulfur loading. The samples are denoted as TC_15_1000/S-40 and so on. The recorded XRD of the samples revealed a successful infiltration up to 60 wt.% (**Fig. 66 left**). Multiple peaks were measured for TC_15_1000/S-70 which are related to a deposition of crystalline sulfur on the surface of the carbon. TC_15_1000 is a mesoporous sample with a high pore volume of 2.4 cm^3 g^{-1} considering a total loading with sulfur 1 g of sample could hold about 4.8 g of sulfur or 83 wt.% (*ρ(S)*: 2 g cm^{-3}). In order to get an idea about the loading preferences, the samples were investigated by N_2 sorption (**Fig. 66 right**). The total pore volume decreased to 0.95 cm^3 g^{-1} from TC_15_1000 to TC_15_1000/S-40. Taking the mass of sulfur into account TC_15_1000/S-40 has 0.6 g carbon (1.44 cm^3) and the volume of sulfur is 0.2 cm^3. This shows that the pore volume is lower than the expected value of 1.2 cm^3 g^{-1} and smaller pores might be blocked but not accessed by the sulfur. The PSD of the samples showed a rapid loss of microporosity but a moderate decrease of mesopores. For the electrochemical characterization, a mass loading of 50 wt.% was used and the samples were checked by XRD to ensure a successful infiltration with sulfur.

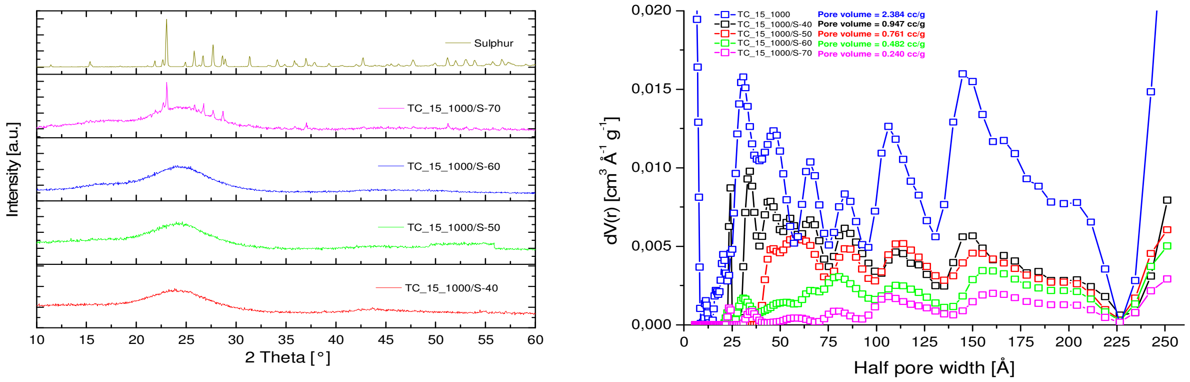

Fig. 66 Left: XRD pattern for pure sulfur and sulfur loaded samples from 40 to 70 wt.%
Right: PSD for non-loaded and loaded carbon TC_15_1000

The battery performance of a microporous sample (TC_11_1000) was checked against the mesoporous sample (TC_15_1000) without any heteroatom doping to investigate the influence of the pore structure. From the cycle test at C/10, a rapid loss in capacity was observed for TC_11_1000. The initial capacity of 838 mAh g^{-1} decreased within the first 25 cycles to 383 mAh g^{-1} and stayed around 330 mAh g^{-1} from the 50th cycle onwards. The rapid capacity decay indicated a poor confinement of polysulfides inside the microporous structure of TC_11_1000. For TC_15_1000, a much slower decrease was observed. The starting capacity of 956 mAh g^{-1} only decreased to 643 mAh g^{-1} for the 25th cycle. The final discharge capacity for TC_11_1000 and TC_15_1000 was measured to be 327 mAh g^{-1} and 377 mAh g^{-1} respectively. The initial superior performance of TC_15_1000 was equaled out over the course of 100 cycles. Even though the mesoporous carbon host demonstrated a better sulfur confinement, a portion of polysulfides will be dissolved each cycle and more and more active material is lost due to the shuttle process. This eventually leads to an equilibrium once the lithium anode is covered with Li_2S. For the subsequent investigation of heteroatom doped samples, mesoporous carbon samples have been selected.

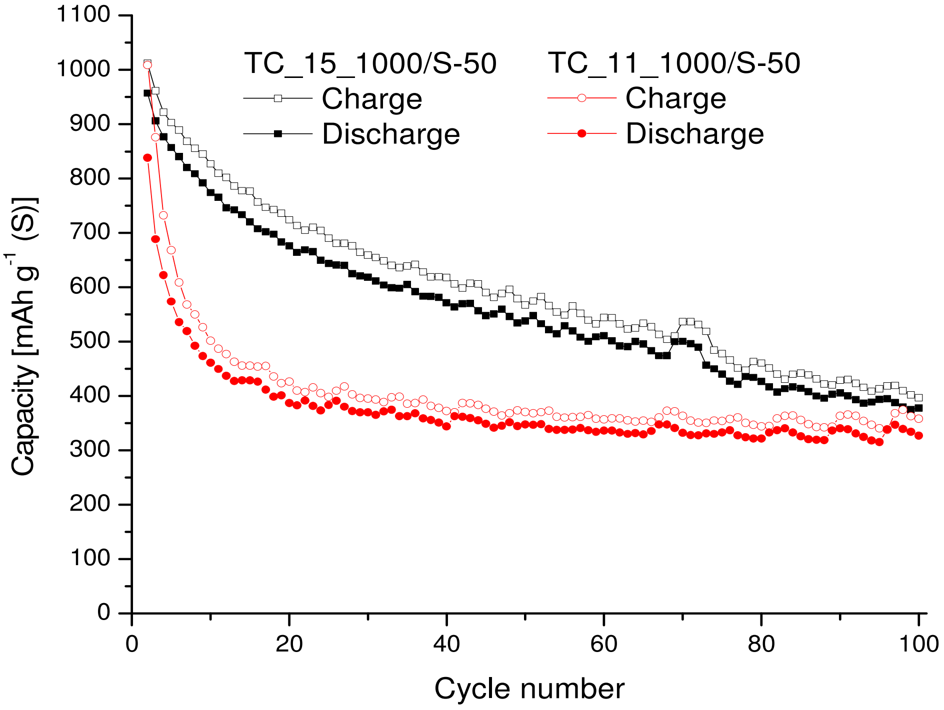

Fig. 67 Cycle performance of TC_11_1000/S-50 and TC_15_1000/S-50 at C/10

The cycle performance of the non-doped sample TC_15_1000 was checked against TC_15_900_N, TC_15_900_S, and TC_15_900_NS for a charge and discharge rate of C/10 (**Fig. 68**). All samples showed a loss in capacity with a similar slope. The highest capacity was recorded for TC_15_900_S with 1290 mAh g^{-1} for the first cycle which decreased to 753 mAh g^{-1} at the 50th cycle. The formation of S-S bonds during the discharge to the polysulfides might be a reason for the enhanced cycle stability compared to TC_15_1000. Furthermore, a positive zeta potential of 9 mV was recorded and an additional electrostatic attraction of the polysulfides to the carbon is possible. The N doped carbon sample TC_15_900_N showed a more rapid capacity fading compared to the other samples but a more steady capacity was recorded compared to TC_15_1000. For the co-doped sample TC_15_900_NS a behavior in between N and S doped was observed. The capacity was higher than that for TC_15_900_N and the capacity loss was less pronounced than that for TC_15_900_S. The coulombic efficiency was around 94% for all samples but slightly higher for TC_15_900_N with 97%. The nitrogen doping can increase the conductivity of the sample and therefore a better charge propagation can lead to a better efficiency.

The results obtained are comparable to those reported for silica template carbons (e.g. CMK-3). Interestingly is the initial capacity varying to some extent but the fading behavior itself is quite similar throughout the literature. Trapping sulfur inside an ordered mesoporous carbon is suppressing the polysulfide shuttle but not cancelling it completely[101, 114, 117, 164].

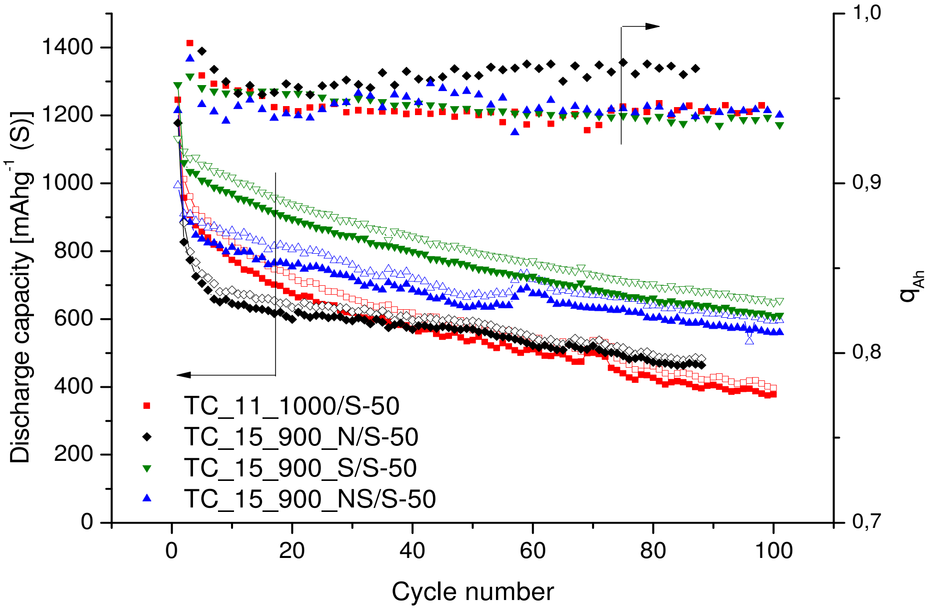

Fig. 68 Comparison of the charge and discharge capacity for N, S and NS doped mesoporous carbons in contrast to a non-doped sample. C/10; S loading 50 wt.%

The nitrogen doped and the non-doped sample was further investigated in respect to their charge and discharge behavior (**Fig. 69 left**). The voltage profile showed the typical behavior with two distinct plateaus at around 2.4 V and 2 V. The plateau regions become smaller with prolonged cycling due to a loss in active sulfur. However, the voltage of the plateau regions is different for TC_15_1000 and TC_15_900_N. A higher voltage was observed for TC_15_900_N which reflects in a higher average discharge voltage (**Fig. 69 right**). The energy efficiency is above 100% for both samples for the first cycle since the test starts with a discharge and a big portion of active material is not recovered during the subsequent charge. The average charge and discharge voltage was more stable for TC_15_900_N and higher energy efficiency were measured. The non-doped carbon showed a loss of 52% in energy density from the 5th to 80th cycle whereas TC_15_900_N only demonstrated a loss of 34%. Considering a higher conductivity for the nitrogen doped sample, a lower IR drop can be expected which explains the better average voltage. This, in combination with a better capacity retention, makes a nitrogen doped carbon host beneficial for the overall performance in a lithium sulfur battery.

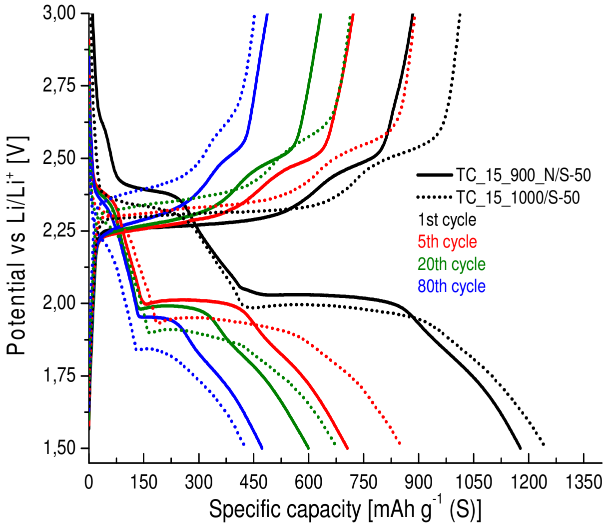

	Average U_t [V]		Energy [Wh kg^{-1} (S)]		q_{Wh} [%]
Cycle	Ch.	Disch.	Ch.	Disch.	
1	2.38	2.03	2408	2525	105
	2.35	2.08	2081	2445	117
5	2.40	1.92	2137	1651	77
	2.36	1.97	1708	1386	81
20	2.43	1.89	1734	1281	73
	2.37	1.95	1503	1165	78
80	2.47	1.85	1116	791	70
	2.38	1.94	1163	913	79

Fig. 69 Left: Voltage profile for TC_15_1000/S-50 (dotted) and TC_15_900_N/S-50 (continuous) for 1st, 5th, 20th and 80th cycle with the charge and discharge branch

Right: Table of charge and discharge properties (terminal voltage, energy density, energy efficiency) for TC_15_1000/S-50 (black) and TC_15_900_N/S-50 (blue)

4.2 UV/Vis Absorption Test of Polysulfides

In order to get a better understanding of the polysulfide adsorption capabilities of the tested carbons a simple UV/Vis absorption test was performed[1](test details are given on page A-6). It was demonstrated in different publications that different polysulfides show different absorption maxima in the UV/Vis range of the electromagnetic spectra[165, 166]. This allows to evaluate the polysulfide adsorption behavior by simply measuring the absorption of the material, while dispersed in a polysulfide solution.

The non-doped carbon sample TC_15_1000 showed only an absorption of the long chain polysulfide Li_2S_8 (**Table 7**). The sulfur doped carbon on the other hand showed in addition to the Li_2S_8 absorption also an absorption for Li_2S_6. The electrochemical performance of the two materials showed a similar fading behavior but TC_15_900_S outperformed TC_15_1000 in terms of cycle stability (**Fig. 68**). The better adsorption of long chain polysulfides for TC_15_900_S correlates well with the results obtained from the actual electrochemical investigation.

The nitrogen doping extended the adsorption to the shorter Li_2S_4 polysulfide while maintaining the adsorption of the long chain polysulfides. The sample TC_15_900_NS showed an absorption behavior in-between the solely nitrogen or sulfur doped sample. Even though TC_15_900_N showed a good coulombic and energy efficiency the initial capacity drop was higher than that for the other samples. The overall adsorption of long to short chain polysulfides seems not to correlate directly with the initial capacity. A closer look at the discharge mechanism of LSB might help to understand this effect.

The discharge mechanism of sulfur to lithium sulfide was studied by a multitude of researchers over the last 30 years[104, 167, 168]. Nonetheless, the exact mechanism is still not completely understood. Recently Dominko *et. al.* were able to study the mechanism in more detail by using a homemade pouch cell capable of UV/Vis measurements in operando[166]. It was shown that long chained polysulfides (Li_2S_8, Li_2S_6) are formed in large quantities during the first discharge step. A longer discharge leads to a depletion of long chain polsulfides and the subsequent formation of mid and short chain polysulfides. While the long chain polysulfides are readily dissolved in the electrolyte, polysulfides with the composition Li_2S_n ($n \leq 4$) are less soluble and can precipitate during the discharge process[169].

Assuming a complete conversion of sulfur to Li_2S_8 and Li_2S_6 in the first step, and the precipitation of Li_2S_4, would speak for the importance of the adsorption of long chain polysulfides. As long as Li_2S_4 precipitate inside the porous carbon material it can be subject to a further discharge to Li_2S. A simple precipitation inside the electrolyte

---

[1] Jiawen Ren is highly acknowledged for synthesizing the polysulfides and conducting the UV/VIS absorption test.

solution or inside the separator would prohibit a further discharge due to a lack in contact with the current collector. Furthermore is the shuttle mechanism suppressed to some extent if the long chain polysulfides are not migrating to the lithium anode.

TC_15_900_N demonstrated an adsorption for the long chain polysulfides Li_2S_8 and Li_2S_6 in the same order as TC_15_900_S but the initial capacity fading during the first 20th cycles was much higher for TC_15_900_N. A possible explanation might be the higher pore volume for TC_15_900_S which can lead to a better trapping of the as formed polysulfides in the first place and suppresses a release all together. Furthermore, the surface area is higher for TC_15_900_S and more sulfur molecules will be in direct contact with the surface of the material. The presented absorption test provides a quick reference point for future experiments. It has to be mentioned that the tests were done in THF and might not be completely applicable to an arbitrary electrolyte system.

Table 7 Polysulfide adsorption and physical properties of carbon samples

Sample	N_2 sorption data			Polysulfide adsorption [mM g^{-1}]		
	V_t [cm^3 g^{-1}]	V_{micro} [cm^3 g^{-1}]	S_t [m^2 g^{-1}]	Li_2S_8	Li_2S_6	Li_2S_4
TC_15_1000	2.38	0.18	1077	3.1	0.5	< 0.1
TC_15_900_S	1.79	0.22	1344	3.2	2.3	< 0.2
TC_15_900_N	0.98	0.17	1051	3.2	2.4	2.2
TC_15_900_NS	1.09	0.21	1212	2.5	2.0	1.7

D Summary and Conclusion

The general motivation for the thesis at hand was the ever growing demand for more energy of our modern society. Especially the high dependence on fossil fuel for our day to day life as a convenient energy and gasoline source has become more and more a major burden. A different path may have spared mankind a lot of hurdles to begin with but a green and sustainable thinking has entered the mind of people around the world. The demand for more energy is nowadays accompanied by the call for sustainability, eco-friendly and green processes. The work carried out in this thesis was aimed at the development of valuable carbon materials from cheap and sustainable biomass precursors. The as prepared carbon materials have been evaluated for their use in energy storage applications such as **s**uper**c**apacitors (**SC**) and **l**ithium **s**ulfur **b**atteries (**LSB**).

The part B of the thesis was devoted to the **h**ydro**t**hermal **c**arbonization (**HTC**) process, since it offers a simple yet green approach towards carbon materials. The borax mediated synthesis approach of Fellinger *et. al.*[129] was used as a reference point. The synthesis was successful extended by the use of dilute ammonia solution as reaction media and nitrogen source. Carbon materials with small primary particles (below 100 nm) and adjustable nitrogen content (depending on the ammonia concentration) have been hydrothermal synthesized using glucose as a convenient carbon source. The nitrogen content was as high as 9 wt.%.

Electrochemical applications usually require a high electrical conductivity in order to support high currents, especially SC needs highly conductive material to be suited for high power applications. Furthermore is a high surface area necessary to accumulate enough surface charge to reach a decent energy density. The HTC carbons showed a low surface area of about 100 m^2 g^{-1}. In order to extent the surface area and introduce conductivity to the material a carbonization at 850 °C under nitrogen was chosen followed by CO_2 activation in the same temperature step. The CO_2 activation proofed to be suited to develop microporous carbons with some mesoporosity and surface areas of up to 1000 m^2 g^{-1}. The nitrogen content after the carbonization was still as high as 7.0 wt.% with a high amount of surface nitrogen functions of 5.3 wt.% as determined by means of XPS.

Nitrogen functions can contribute to the overall capacitance of a SC by so called pseudocapacitance, which is attributed to fast faradaic reactions at the surface of the material. The HTC carbons after CO_2 activation showed a capacitance of 150 F g^{-1} up to 185 F g^{-1} for the nitrogen level of 3.9 and 7.0 wt.% respectively. The capacitance measured under a high current density of 20 A g^{-1} was found to be 144 F g^{-1} leading to a high power density of 17.6 kW kg^{-1} and an energy density of 25.3 Wh kg^{-1}. The capacitance was increasing with higher nitrogen content and correlated with the nitrogen amount, determined via EA and XPS.

In general was the borax catalyzed hydrothermal process found to be suited, in combination with ammonia solutions, to develop nitrogen doped carbon materials. The subsequent CO_2 activation led to porous materials. Nonetheless, the activation is detrimental in terms of yield since it develops pores at the expense of carbon material. Furthermore are basic conditions not favorable for the HTC process since longer reaction times are required to achieve high carbon yields. In order to overcome as mentions drawbacks a salt template assisted approach was studied as surrogate for the HTC process in part C of this thesis.

Salt templates are known as a versatile scaffold for the carbonization of ionic liquids and different morphologies can be achieved by simply varying the salt mixture and the amount of the salt template (work of Fechler *et. al.*[148]). This concept was the starting point for the synthesis described in part C of this thesis.

Glucose was again chosen as a cheap and sustainable carbon precursor. The synthesis was meant to resemble the HTC process therefore glucose was dissolved together with $ZnCl_2$ in water. It was shown that the synthesis of the carbon material takes place before the $ZnCl_2$ is evaporated. The mechanism was proposed to be similar to that found for the HTC process. Indeed showed FTIR and NMR studies, on samples taken during the synthesis, close similarities to those obtained for the HTC process. The NMR results revealed the presence of hydroxymethylfurfural at temperatures of 200 ° C, which is believed to be the main building block of the carbons derived from HTC.

Different carbonization temperature of 800, 900 and 1000 ° C were chosen to study the process. It was found that the ratio between glucose and $ZnCl_2$ is the main factor influencing the carbon morphology. Lower ratios of 1:1 gave rise to a microporous material whereas a 1:5 ratio led to an aerogel like mesoporous material. The surface area and pore volume was as high as 1700 m^2 g^{-1} and 2.4 cm^3 g^{-1} respectively.

In order to extent the synthesis to functional carbons, beyond oxygen functionalities, concepts known from the HTC were adapted to the presented process. The nitrogen doping was achieved by using glucosamine instead of glucose. Nitrogen levels of up to 6.7 wt.% were measured by EA but the surface area and pore volume decreased to 1000 m^2 g^{-1} and 1.0 cm^3 g^{-1}. Even though XRD studies did not reveal any diffraction pattern, a residual mass of about 10 wt.% was determined via TGA. Nitrogen is well known to coordinate zinc species which is a possible explanation for the residual mass and lower pore volume.

The doping was not limited to nitrogen and it was demonstrated that sulfur can be introduced by adding 2-thiophenecarboxylic acid (TCA) to the starting solution. TCA can react with HMF via a [4+2] cycloaddition or by an ester formation. The sulfur doping was as high as 2.5 wt.% and also a combination of nitrogen and sulfur was possible with a nitrogen and sulfur content of 6.5 wt.% and 1.9 wt.% respectively. Since the process is solution based a bottom up sol gel route can be expected. Indeed small, spherical primary particles were observed and the nitrogen doping was found to be evenly distributed over the carbon framework as determined by HRTEM/EELS.

In addition to $ZnCl_2$ template cesium acetate (CsAc) was also evaluated since it is known to give rise to high surface areas. By using solely CsAc as template, surface areas up to 2600 m^2 g^{-1} were achieved (1:5 ratio of glucosamine to CsAc). The nitrogen doping on the other hand was only about 1 wt.% which shows that the overall carbon contribution by the CsAc itself is quite significant. Combining CsAc with $ZnCl_2$ was also a viable approach to tune the porosity of the carbon materials in respect to their application.

The as described set of carbon materials was used for supercapacitor applications in different electrolyte solutions. The evaluation in 1 M sulfuric acid gave the best performance for a plain carbon without additional doping. This contradicts the common believe that a nitrogen doping is necessary for a high pseudocapacity. Apparently, oxygen functions are not inferior in terms of redox activity. Nonetheless, the nitrogen doping was found to be beneficial at higher current densities were the higher conductivity leads to a better performance. The oberservations made here are limited to the synthesized range of carbons and further research is necessary to gain more insights into the charge storage mechanism in pseudocapacitors.

Further tests in ionic liquids gave very high energy densities of up to 180 Wh kg^{-1} due to the larger voltage window. The carbons selected for the test in IL were all mesoporous to account for the larger ion size. The voltage loss for the select carbons was rather low with the exception of the nitrogen/sulfur co-doped sample. It was demonstrated before that pores close to the ion size of the IL show the best SC performance but also transport pores are important for a fast ion diffusion.

The carbon samples derived from the binary salt template of $ZnCl_2$ and CsAc fulfilled this requirement and gave a high capacitance of ca. 300 F g^{-1} in sulfuric acid. On the other hand, for the test in a neutral 1 M sodium chloride solution the carbon synthesized exclusively with glucosamine and CsAc (1:5) gave the highest capacitance of about 200 F g^{-1} which is a very high value for a neutral electrolyte. The high capacitance in 1 M sodium chloride also hints at a possible implementation as electrode material for the capacitive deionization process. In general was no correlation found, between different electrolyte systems and the SC performance. Each system required a task specific porous carbon (i.e. were one carbon showed a good performance under aqueous conditions it was not suited for IL etc.).

The mesoporous carbons synthesized at 900 ° C were evaluated as cathode material for LSB in order to investigate the influence of heteroatoms on the battery performance. LSB usually show a rapid capacity fading due to the polysulfide shuttle mechanism and carbon hosts with a high attraction to polysulfides are necessary. The sulfur doping was demonstrated to be well suited as cathode material. A simple -S-S- bond might be a possible explanation for the better cycle stability of sulfur doped carbons. The nitrogen doped carbon was investigated in more detail and showed an enhanced energy efficiency and energy density compared to the non-doped carbon. The energy loss was 52% for the non-doped sample and only 34% for the nitrogen doped sample. The energy density after 80 cycles was around 900 Wh kg^{-1} for the nitrogen doped sample. Even though the polysulfide shuttle can be suppressed to some extend by different heteroatom dopings further research is needed to identify a suitable cathode material. A combined approach involving a sulfur doped carbon in combination with an additional surface or separator modification could lead to a further suppression of the shuttle mechanism.

In summary the work done in this thesis extends the carbon tool box by a simple one-step synthesis exploiting known principles from the hydrothermal carbonization and salt templates. The presented process is very versatile for the development of different porosities and heteroatom dopings. The scalability of the process was already tested and quantities up to 0.5 kg have been produced for prototype 18650 LSB cells (not shown in the thesis). The used $ZnCl_2$ can potentially be recovered during the synthesis and therefore be recycled, hence leading to a cost effective process were only glucose is consumed.

E References

1. Knothe, G., *Historical Perspectives on Vegetable Oil-Based Diesel Fuels* Inform, 2001. **12**.
2. Steve Janisse, S.J., *Prof. Ferdinand Porsche Created the First Functional Hybrid Car* Porsche press release, 2011.
3. Kettering, C.F., *Engine-starting device*. 1915, Google Patents.
4. Petroleum, B., *Statistical Review of World Energy 2013*. 2013.
5. Bharat Raj Singh, O.S., *Global Trends of Fossil Fuel Reserves and Climate Change in the 21st Century* 2009.
6. Administrator, O.o.t.M., *Deepwater Horizon Marine Casualty Investigation Report*. 2011.
7. Center, C.D.I.A., *CO2 emission*. 2014.
8. Agency, U.E.P., *Inventory of U.S. Greenhouse Gas Emissions and Sinks: 1990-2011*. 2011.
9. Green, D., *Solar Energy Facts – Solar Energy Storage enables CSP and PV on the grid*. Renewable Green Energy Power, 2012.
10. Cimuca, G.O., et al., *Control and Performance Evaluation of a Flywheel Energy-Storage System Associated to a Variable-Speed Wind Generator*. Industrial Electronics, IEEE Transactions on, 2006. **53**(4): p. 1074-1085.
11. Deane, J.P., B.P. Ó Gallachóir, and E.J. McKeogh, *Techno-economic review of existing and new pumped hydro energy storage plant*. Renewable and Sustainable Energy Reviews, 2010. **14**(4): p. 1293-1302.
12. Ibrahim, H., A. Ilinca, and J. Perron, *Energy storage systems—Characteristics and comparisons*. Renewable and Sustainable Energy Reviews, 2008. **12**(5): p. 1221-1250.
13. Tarascon, J.M. and M. Armand, *Issues and challenges facing rechargeable lithium batteries*. Nature, 2001. **414**(6861): p. 359-367.
14. Eurostat, *Versorgung, Umwandlung, Verbrauch - Elektrizität - jährliche Daten , Zeitreihe Nettoerzeugung der Pumpspeicherkraftwerke von hauptsächlich als Energieerzeuger tätigen Unternehmen*. 2013.
15. caranddriver.com, *Decade in Review: Electric Cars* 2009.
16. Bettina Kampman, B.B., *Cool cars, fancy fuels*. 2005.
17. Energy, U.S.D.o., *Fuel Cells for Transportation*. 2013.
18. Urken, R.K., *Tesla Debacle Highlights Need For New EV Battery Technology*. Forbes, 2013.
19. Thomas Franke, J.F.K., *What drives range preferences in electric vehicle users?* Transport Policy, 2013.
20. Goodenough, J.B. and Y. Kim, *Challenges for Rechargeable Li Batteries†*. Chemistry of Materials, 2009. **22**(3): p. 587-603.
21. Pandolfo, A.G. and A.F. Hollenkamp, *Carbon properties and their role in supercapacitors*. Journal of Power Sources, 2006. **157**(1): p. 11-27.
22. Oren, Y., *Capacitive deionization (CDI) for desalination and water treatment — past, present and future (a review)*. Desalination, 2008. **228**(1–3): p. 10-29.
23. deKrafft, K.E., et al., *Electrochemical Water Oxidation with Carbon-Grafted Iridium Complexes*. ACS Applied Materials & Interfaces, 2012. **4**(2): p. 608-613.
24. Weeks, M.E., *Discovery of the Elements*. Journal of Chemical Education, 1968.
25. Erwin Riedel, C.J., *Anorganische Chemie*. 2007.
26. Taylor, R. and D.R.M. Walton, *The chemistry of fullerenes*. Nature, 1993. **363**(6431): p. 685-693.
27. Thostenson, E.T., Z. Ren, and T.-W. Chou, *Advances in the science and technology of carbon nanotubes and their composites: a review*. Composites Science and Technology, 2001. **61**(13): p. 1899-1912.

28. Geim, A.K. and K.S. Novoselov, *The rise of graphene.* Nat Mater, 2007. **6**(3): p. 183-191.
29. Robertson, J., *Amorphous carbon.* Advances in Physics, 1986. **35**(4): p. 317-374.
30. Chen, Y., et al., *Application studies of activated carbon derived from rice husks produced by chemical-thermal process—A review.* Advances in Colloid and Interface Science, 2011. **163**(1): p. 39-52.
31. Fellinger, T.-P., et al., *25th Anniversary Article: "Cooking Carbon with Salt": Carbon Materials and Carbonaceous Frameworks from Ionic Liquids and Poly(ionic liquid)s.* Advanced Materials, 2013. **25**(41): p. 5838-5855.
32. Lee, J., J. Kim, and T. Hyeon, *Recent Progress in the Synthesis of Porous Carbon Materials.* Advanced Materials, 2006. **18**(16): p. 2073-2094.
33. Paraknowitsch, J.P. and A. Thomas, *Functional Carbon Materials From Ionic Liquid Precursors.* Macromolecular Chemistry and Physics, 2012. **213**(10-11): p. 1132-1145.
34. Frackowiak, E. and F. Béguin, *Carbon materials for the electrochemical storage of energy in capacitors.* Carbon, 2001. **39**(6): p. 937-950.
35. Molina-Sabio, M., et al., *Effect of steam and carbon dioxide activation in the micropore size distribution of activated carbon.* Carbon, 1996. **34**(4): p. 505-509.
36. Yoon, S.-H., et al., *KOH activation of carbon nanofibers.* Carbon, 2004. **42**(8–9): p. 1723-1729.
37. Davis, M.E., *Ordered porous materials for emerging applications.* Nature, 2002. **417**(6891): p. 813-821.
38. Kruk, M., et al., *Characterization of the Porous Structure of SBA-15.* Chemistry of Materials, 2000. **12**(7): p. 1961-1968.
39. Chen, C.-Y., H.-X. Li, and M.E. Davis, *Studies on mesoporous materials: I. Synthesis and characterization of MCM-41.* Microporous Materials, 1993. **2**(1): p. 17-26.
40. Zhou, H., et al., *Electrochemical capacitance of self-ordered mesoporous carbon.* Journal of Power Sources, 2003. **122**(2): p. 219-223.
41. Liu, X., N. Fechler, and M. Antonietti, *Salt melt synthesis of ceramics, semiconductors and carbon nanostructures.* Chemical Society Reviews, 2013. **42**(21): p. 8237-8265.
42. Torregrosa-Maciá, R., J.M. Martín-Martínez, and M.C. Mittelmeijer-Hazeleger, *Porous texture of activated carbons modified with carbohydrates.* Carbon, 1997. **35**(4): p. 447-453.
43. White, R.J., M. Antonietti, and M.-M. Titirici, *Naturally inspired nitrogen doped porous carbon.* Journal of Materials Chemistry, 2009. **19**(45): p. 8645-8650.
44. Wohlgemuth, S.-A., et al., *A one-pot hydrothermal synthesis of tunable dual heteroatom-doped carbon microspheres.* Green Chemistry, 2012. **14**(3): p. 741-749.
45. Latham, K.G., et al., *Nitrogen Doping of Hydrochars Produced Hydrothermal Treatment of Sucrose in H2O, H2SO4, and NaOH.* ACS Sustainable Chemistry & Engineering, 2013.
46. Zhang, D., et al., *Hydrothermal synthesis of highly nitrogen-doped carbon powder.* Applied Surface Science, 2012. **258**(7): p. 2510-2514.
47. Świetlik, U., et al., *High temperature ammonia treatment of pitch particulates and fibers for nitrogen enriched microporous carbons.* Fuel Processing Technology, 2014. **119**(0): p. 211-217.
48. Frackowiak, E., *Carbon materials for supercapacitor application.* Physical Chemistry Chemical Physics, 2007. **9**(15): p. 1774-1785.
49. Miller, J., *A Brief History of Supercapacitors.* 2007.
50. Cohen, B., *Benjamin Franklin's Science.* 1996.
51. M. Jayalakshmi, K.B., *Simple Capacitors to Supercapacitors - An Overview.* 2008.
52. Pollack, C., *Elektrischen Flüssigkeitskondensators mit Aluminiumelektroden Patentnummer 92564.* Kaiserliches Patentamt, Deutschland, 1896.

53. Peigney, A., et al., *Specific surface area of carbon nanotubes and bundles of carbon nanotubes.* Carbon, 2001. **39**(4): p. 507-514.
54. Wang, Y., et al., *Supercapacitor Devices Based on Graphene Materials.* The Journal of Physical Chemistry C, 2009. **113**(30): p. 13103-13107.
55. Chmiola, J., et al., *Monolithic Carbide-Derived Carbon Films for Micro-Supercapacitors.* Science, 2010. **328**(5977): p. 480-483.
56. Futaba, D.N., et al., *Shape-engineerable and highly densely packed single-walled carbon nanotubes and their application as super-capacitor electrodes.* Nat Mater, 2006. **5**(12): p. 987-994.
57. Pröbstle, H., C. Schmitt, and J. Fricke, *Button cell supercapacitors with monolithic carbon aerogels.* Journal of Power Sources, 2002. **105**(2): p. 189-194.
58. Simon, P. and Y. Gogotsi, *Materials for electrochemical capacitors.* Nat Mater, 2008. **7**(11): p. 845-854.
59. Balducci, A., et al., *High temperature carbon–carbon supercapacitor using ionic liquid as electrolyte.* Journal of Power Sources, 2007. **165**(2): p. 922-927.
60. Earle Martyn, J. and R. Seddon Kenneth, *Ionic Liquids: Green Solvents for the Future*, in *Clean Solvents*. 2002, American Chemical Society. p. 10-25.
61. Liu, C., et al., *Advanced Materials for Energy Storage.* Advanced Materials, 2010. **22**(8): p. E28-E62.
62. Congress, G.C., *FDK To Begin Mass Production of High-Capacity Li-Ion Capacitors; Automotive and Renewable Energy Applications.* 2009.
63. Khomenko, V., E. Raymundo-Piñero, and F. Béguin, *High-energy density graphite/AC capacitor in organic electrolyte.* Journal of Power Sources, 2008. **177**(2): p. 643-651.
64. Amatucci, G.G., et al., *An Asymmetric Hybrid Nonaqueous Energy Storage Cell.* Journal of The Electrochemical Society, 2001. **148**(8): p. A930-A939.
65. Wang, H., et al., *Ni(OH)2 Nanoplates Grown on Graphene as Advanced Electrochemical Pseudocapacitor Materials.* Journal of the American Chemical Society, 2010. **132**(21): p. 7472-7477.
66. Nam, H.-S., et al., *Electrochemical capacitance of nanoporous hydrous RuO2 templated by anionic surfactant.* Electrochimica Acta, 2011. **56**(18): p. 6459-6463.
67. Broughton, J.N. and M.J. Brett, *Variations in MnO2 electrodeposition for electrochemical capacitors.* Electrochimica Acta, 2005. **50**(24): p. 4814-4819.
68. Skeleton, *SkelCap.* 2014.
69. Du Pasquier, A., et al., *A comparative study of Li-ion battery, supercapacitor and nonaqueous asymmetric hybrid devices for automotive applications.* Journal of Power Sources, 2003. **115**(1): p. 171-178.
70. Kötz, R. and M. Carlen, *Principles and applications of electrochemical capacitors.* Electrochimica Acta, 2000. **45**(15–16): p. 2483-2498.
71. Rodatz, P., et al., *Optimal power management of an experimental fuel cell/supercapacitor-powered hybrid vehicle.* Control Engineering Practice, 2005. **13**(1): p. 41-53.
72. Nürnberg, V.V.-A., *Der Ultracapbus.* 2014.
73. Hamilton, T., *Next Stop: Ultracapacitor Buses.* http://www.technologyreview.com, 2009.
74. Fröhlich, M., *Energy Storage on Board of Rail Vehicles The Climate is Right for Trains.* BOMBARDIER, 2010.
75. Media, M.R., *Ultracapacitor Market Forecast 2015-2020.* 2012.
76. Beguin, F. and E. Frackowiak, *Supercapacitors Materials, Systems, and Applications.* 2013.
77. Chmiola, J., et al., *Anomalous increase in carbon capacitance at pore sizes less than 1 nanometer.* Science, 2006. **313**(5794): p. 1760-1763.
78. Gogotsi, Y., et al., *Nanoporous carbide-derived carbon with tunable pore size.* Nat Mater, 2003. **2**(9): p. 591-594.

79. Huang, J., B.G. Sumpter, and V. Meunier, *Theoretical model for nanoporous carbon supercapacitors.* Angewandte Chemie International Edition, 2008. **47**(3): p. 520-524.
80. Conway, B.E. and B. Conway, *Ionic hydration in chemistry and biophysics.* Vol. 741. 1981: Elsevier Amsterdam.
81. Conway, B.E., *Electrochemical Supercapacitors Scientific Fundamentals and Technological Applications.* 1999.
82. de Levie, R., *On porous electrodes in electrolyte solutions—IV.* Electrochimica Acta, 1964. **9**(9): p. 1231-1245.
83. Keiser, H., K.D. Beccu, and M.A. Gutjahr, *Abschätzung der porenstruktur poröser elektroden aus impedanzmessungen.* Electrochimica Acta, 1976. **21**(8): p. 539-543.
84. Taberna, P.L., P. Simon, and J.F. Fauvarque *Electrochemical Characteristics and Impedance Spectroscopy Studies of Carbon-Carbon Supercapacitors.* Journal of The Electrochemical Society, 2003. **150**(3): p. A292-A300.
85. Zhang, S., et al., *Physical properties of ionic liquids: database and evaluation.* Journal of physical and chemical reference data, 2006. **35**(4): p. 1475-1517.
86. Piccolino, M., *Animal electricity and the birth of electrophysiology: the legacy of Luigi Galvani.* Brain Research Bulletin, 1998. **46**(5): p. 381-407.
87. Mertens, J., *Shocks and Sparks: The Voltaic Pile as a Demonstration Device.* Isis, 1998. **89**(2): p. 300-311.
88. Leclanché, G., *Französisches Patent Nr. 71 865.* 1866.
89. Kurzweil, P., *History — Electrochemistry Encyclopedia of Electrochemical Power Sources Vol. 3.* Elsevier B.V., 2009: p. 533-554.
90. Kurzweil, P., *History — Secondary Batteries; Encyclopedia of Electrochemical Power Sources Vol. 3.* Elsevier B.V., 2009.
91. Mizushima, K., et al., *LixCoO2 (0<x<-1): A new cathode material for batteries of high energy density.* Materials Research Bulletin, 1980. **15**(6): p. 783-789.
92. Takehara, Z.-i., *Future prospects of the lithium metal anode.* Journal of Power Sources, 1997. **68**(1): p. 82-86.
93. Besenhard, J.O., *The electrochemical preparation and properties of ionic alkali metal-and NR4-graphite intercalation compounds in organic electrolytes.* Carbon, 1976. **14**(2): p. 111-115.
94. Flandrois, S. and B. Simon, *Carbon materials for lithium-ion rechargeable batteries.* Carbon, 1999. **37**(2): p. 165-180.
95. Winter, M., et al., *Insertion Electrode Materials for Rechargeable Lithium Batteries.* Advanced Materials, 1998. **10**(10): p. 725-763.
96. Daniel, C. and J.O. Besenhard, *Handbook of Battery Materials.* 2011.
97. Kim, J.H., S.T. Myung, and Y.K. Sun, *Molten salt synthesis of LiNi0.5Mn1.5O4 spinel for 5 V class cathode material of Li-ion secondary battery.* Electrochimica Acta, 2004. **49**(2): p. 219-227.
98. Chan, C.K., et al., *High-performance lithium battery anodes using silicon nanowires.* Nat Nano, 2008. **3**(1): p. 31-35.
99. Winter, M. and J.O. Besenhard, *Electrochemical lithiation of tin and tin-based intermetallics and composites.* Electrochimica Acta, 1999. **45**(1–2): p. 31-50.
100. Cabana, J., et al., *The first lithium manganese oxynitride, Li7.9MnN5 - yOy: preparation and use as electrode material in lithium batteries.* Journal of Materials Chemistry, 2003. **13**(10): p. 2402-2404.
101. Ji, X., K.T. Lee, and L.F. Nazar, *A highly ordered nanostructured carbon-sulphur cathode for lithium-sulphur batteries.* Nat Mater, 2009. **8**(6): p. 500-506.
102. Bruce, P.G., et al., *Li-O2 and Li-S batteries with high energy storage.* Nat Mater, 2012. **11**(1): p. 19-29.
103. Ji, X. and L.F. Nazar, *Advances in Li-S batteries.* Journal of Materials Chemistry, 2010. **20**(44): p. 9821-9826.
104. Mikhaylik, Y.V. and J.R. Akridge, *Polysulfide Shuttle Study in the Li/S Battery System.* Journal of The Electrochemical Society, 2004. **151**(11): p. A1969-A1976.

105. Kasavajjula, U., C. Wang, and A.J. Appleby, *Nano- and bulk-silicon-based insertion anodes for lithium-ion secondary cells.* Journal of Power Sources, 2007. **163**(2): p. 1003-1039.
106. Derrien, G., et al., *Nanostructured Sn–C Composite as an Advanced Anode Material in High-Performance Lithium-Ion Batteries.* Advanced Materials, 2007. **19**(17): p. 2336-2340.
107. Lide, D.R., *CRC Handbook of Chemistry and Physics, 85. Ed.* CRC Press LLC, 2005.
108. Danuta, H. and U. Juliusz, *Electric dry cells and storage batteries.* 1962, Google Patents.
109. Brun, N., et al., *Hydrothermal carbon-based nanostructured hollow spheres as electrode materials for high-power lithium–sulfur batteries.* Physical Chemistry Chemical Physics, 2013. **15**(16): p. 6080-6087.
110. Lee, J.T., et al., *Sulfur-Infiltrated Micro- and Mesoporous Silicon Carbide-Derived Carbon Cathode for High-Performance Lithium Sulfur Batteries.* Advanced Materials, 2013. **25**(33): p. 4573-4579.
111. Dörfler, S., et al., *High capacity vertical aligned carbon nanotube/sulfur composite cathodes for lithium–sulfur batteries.* Chemical Communications, 2012. **48**(34): p. 4097-4099.
112. Kong, J., A.M. Cassell, and H. Dai, *Chemical vapor deposition of methane for single-walled carbon nanotubes.* Chemical Physics Letters, 1998. **292**(4–6): p. 567-574.
113. Choy, K.L., *Chemical vapour deposition of coatings.* Progress in Materials Science, 2003. **48**(2): p. 57-170.
114. Wang, H., et al., *Graphene-Wrapped Sulfur Particles as a Rechargeable Lithium–Sulfur Battery Cathode Material with High Capacity and Cycling Stability.* Nano Letters, 2011. **11**(7): p. 2644-2647.
115. Kuila, T., et al., *Chemical functionalization of graphene and its applications.* Progress in Materials Science, 2012. **57**(7): p. 1061-1105.
116. Xiao, L., et al., *A Soft Approach to Encapsulate Sulfur: Polyaniline Nanotubes for Lithium-Sulfur Batteries with Long Cycle Life.* Advanced Materials, 2012. **24**(9): p. 1176-1181.
117. Sun, X.-G., et al., *Lithium–Sulfur Batteries Based on Nitrogen-Doped Carbon and an Ionic-Liquid Electrolyte.* ChemSusChem, 2012. **5**(10): p. 2079-2085.
118. Scheers, J., S. Fantini, and P. Johansson, *A review of electrolytes for lithium–sulphur batteries.* Journal of Power Sources, 2014. **255**(0): p. 204-218.
119. Marmorstein, D., et al., *Electrochemical performance of lithium/sulfur cells with three different polymer electrolytes.* Journal of Power Sources, 2000. **89**(2): p. 219-226.
120. *http://www.sionpower.com.* 2014.
121. *http://www.iws.fraunhofer.de/malisu.* 2014.
122. *http://www.eurolis.eu/.* 2014.
123. Cheon, S.-E., et al., *Rechargeable lithium sulfur battery I. Structural change of sulfur cathode during discharge and charge.* Journal of The Electrochemical Society, 2003. **150**(6): p. A796-A799.
124. Bergius, F., *Production of hydrogen from water and coal from cellulose at high temperatures and pressures.* Journal of the Society of Chemical Industry, 1913. **32**(9): p. 462-467.
125. Zhao, L., et al., *Carbon Dioxide Capture on Amine-Rich Carbonaceous Materials Derived from Glucose.* ChemSusChem, 2010. **3**(7): p. 840-845.
126. Hu, Y.-S., et al., *Superior Storage Performance of a Si@SiOx/C Nanocomposite as Anode Material for Lithium-Ion Batteries.* Angewandte Chemie International Edition, 2008. **47**(9): p. 1645-1649.
127. Demir-Cakan, R., et al., *Facile One-Pot Synthesis of Mesoporous SnO2 Microspheres via Nanoparticles Assembly and Lithium Storage Properties.* Chemistry of Materials, 2008. **20**(4): p. 1227-1229.

128. Demir-Cakan, R., et al., *Hydrothermal synthesis of imidazole functionalized carbon spheres and their application in catalysis.* Catalysis Today, 2010. **150**(1–2): p. 115-118.
129. Fellinger, T.-P., et al., *Borax-Mediated Formation of Carbon Aerogels from Glucose.* Advanced Functional Materials, 2012. **22**(15): p. 3254-3260.
130. Titirici, M.-M., M. Antonietti, and N. Baccile, *Hydrothermal carbon from biomass: a comparison of the local structure from poly- to monosaccharides and pentoses/hexoses.* Green Chemistry, 2008. **10**(11): p. 1204-1212.
131. Antal Jr, M.J., W.S.L. Mok, and G.N. Richards, *Mechanism of formation of 5-(hydroxymethyl)-2-furaldehyde from d-fructose and sucrose.* Carbohydrate Research, 1990. **199**(1): p. 91-109.
132. Sowden, J.C. and R. Schaffer, *The Isomerization of D-Glucose by Alkali in D2O at 25fl1.* Journal of the American Chemical Society, 1952. **74**(2): p. 505-507.
133. Latham, K.G., et al., *The Nitrogen Doping of Hydrochars Produced Hydrothermal Treatment of Sucrose in H2O, H2SO4 and NaOH.* ACS Sustainable Chemistry & Engineering, 2013.
134. Watanabe, M., et al., *Glucose reactions with acid and base catalysts in hot compressed water at 473 K.* Carbohydrate Research, 2005. **340**(12): p. 1925-1930.
135. Fellinger, T.-P., *Hydrothermal and ionothermal carbon structures: from carbon negative materials to energy applications*. 2011, Universitätsbibliothek.
136. Titirici, M.-M., *Sustainable carbon materials from hydrothermal processes.* Vol. 6. 2013: Wiley Online Library.
137. Fechler, N., et al., *Salt and sugar: direct synthesis of high surface area carbon materials at low temperatures via hydrothermal carbonization of glucose under hypersaline conditions.* Journal of Materials Chemistry A, 2013. **1**(33): p. 9418-9421.
138. Yu, L., et al., *Hydrothermal nanocasting: Synthesis of hierarchically porous carbon monoliths and their application in lithium–sulfur batteries.* Carbon, 2013. **61**(0): p. 245-253.
139. Lozano-Castelló, D., et al., *Carbon activation with KOH as explored by temperature programmed techniques, and the effects of hydrogen.* Carbon, 2007. **45**(13): p. 2529-2536.
140. Falco, C., *Sustainable biomass-derived hydrothermal carbons for energy applications*. 2012, Universitätsbibliothek.
141. Titirici, M.-M., et al., *Black perspectives for a green future: hydrothermal carbons for environment protection and energy storage.* Energy & Environmental Science, 2012. **5**(5): p. 6796-6822.
142. Lillo-Ródenas, M.A., et al., *About reactions occurring during chemical activation with hydroxides.* Carbon, 2004. **42**(7): p. 1371-1375.
143. Frackowiak, E., et al., *Enhanced capacitance of carbon nanotubes through chemical activation.* Chemical Physics Letters, 2002. **361**(1–2): p. 35-41.
144. Lillo-Ródenas, M.A., D. Cazorla-Amorós, and A. Linares-Solano, *Understanding chemical reactions between carbons and NaOH and KOH: An insight into the chemical activation mechanism.* Carbon, 2003. **41**(2): p. 267-275.
145. Falbe, J., H. Römpp, and M. Regitz, *Römpp Chemie Lexikon.* Vol. 3. 1990: Thieme.
146. Stoller, M.D. and R.S. Ruoff, *Best practice methods for determining an electrode material's performance for ultracapacitors.* Energy & Environmental Science, 2010. **3**(9): p. 1294-1301.
147. Falco, C., et al., *Hydrothermal Carbons from Hemicellulose-Derived Aqueous Hydrolysis Products as Electrode Materials for Supercapacitors.* ChemSusChem, 2013. **6**(2): p. 374-382.
148. Fechler, N., *Salts as highly diverse porogens: functional ionic liquid-derived carbons and carbon-based composites for energy-related applications.* 2013, Universitätsbibliothek.

149. Wohlgemuth, S.-A., *Functional nanostructured hydrothermal carbons for sustainable technologies: heteroatom doping and superheated vapor.* 2012, Universitätsbibliothek.

150. Mojarrad, J.S., et al., *Preparation of Glucosamine from Exoskeleton of Shrimp and Predicting Production Yield by Response Surface Methodology.* Journal of Agricultural and Food Chemistry, 2007. 55(6): p. 2246-2250.

151. Azevedo, D.C.S., et al., *Microporous activated carbon prepared from coconut shells using chemical activation with zinc chloride.* Microporous and Mesoporous Materials, 2007. 100(1–3): p. 361-364.

152. Tay, J.H., et al., *Optimising the preparation of activated carbon from digested sewage sludge and coconut husk.* Chemosphere, 2001. 44(1): p. 45-51.

153. Prauchner, M.J. and F. Rodríguez-Reinoso, *Chemical versus physical activation of coconut shell: A comparative study.* Microporous and Mesoporous Materials, 2012. 152(0): p. 163-171.

154. Chung, K.G., *Heteroatom-containing carbons for high energy density supercapacitors.* 2013.

155. Frackowiak, E., et al., *Optimisation of supercapacitors using carbons with controlled nanotexture and nitrogen content.* Electrochimica Acta, 2006. 51(11): p. 2209-2214.

156. Lota, G., et al., *Effect of nitrogen in carbon electrode on the supercapacitor performance.* Chemical Physics Letters, 2005. 404(1–3): p. 53-58.

157. Hulicova, D., M. Kodama, and H. Hatori, *Electrochemical Performance of Nitrogen-Enriched Carbons in Aqueous and Non-Aqueous Supercapacitors.* Chemistry of Materials, 2006. 18(9): p. 2318-2326.

158. Mauricio Mora Jaramillo, A.M., Susana Vaquero, Marc Anderson, Jesus Palma, Rebeca Marcilla, *Role of textural properties and surface functionalities of selected carbons on the electrochemical behavior of liquid bases-supercapacitors.* RCS Advances, 2012.

159. Moshtev, R. and B. Johnson, *State of the art of commercial Li ion batteries.* Journal of Power Sources, 2000. 91(2): p. 86-91.

160. Porada, S., et al., *Direct prediction of the desalination performance of porous carbon electrodes for capacitive deionization.* Energy & Environmental Science, 2013. 6(12): p. 3700-3712.

161. Fic, K., et al., *Novel insight into neutral medium as electrolyte for high-voltage supercapacitors.* Energy & Environmental Science, 2012. 5(2): p. 5842-5850.

162. Demarconnay, L., E. Raymundo-Piñero, and F. Béguin, *A symmetric carbon/carbon supercapacitor operating at 1.6 V by using a neutral aqueous solution.* Electrochemistry Communications, 2010. 12(10): p. 1275-1278.

163. Hamann, C.H. and W. Vielstich, *Elektrochemie: Völlig überarbeitete und erweiterte Auflage.* 1998: Wiley-VCH.

164. Evers, S. and L.F. Nazar, *New Approaches for High Energy Density Lithium–Sulfur Battery Cathodes.* Accounts of Chemical Research, 2012. 46(5): p. 1135-1143.

165. Barchasz, C., et al., *Lithium/Sulfur Cell Discharge Mechanism: An Original Approach for Intermediate Species Identification.* Analytical Chemistry, 2012. 84(9): p. 3973-3980.

166. Patel, M.U.M., et al., *Li-S Battery Analyzed by UV/Vis in Operando Mode.* ChemSusChem, 2013. 6(7): p. 1177-1181.

167. Aurbach, D., et al., *On the Surface Chemical Aspects of Very High Energy Density, Rechargeable Li–Sulfur Batteries.* Journal of The Electrochemical Society, 2009. 156(8): p. A694-A702.

168. Rauh, R.D., et al., *A Lithium/Dissolved Sulfur Battery with an Organic Electrolyte.* Journal of The Electrochemical Society, 1979. 126(4): p. 523-527.

169. Yamin, H., et al., *The electrochemical behavior of polysulfides in tetrahydrofuran.* Journal of Power Sources, 1985. 14(1–3): p. 129-134.

F Appendix

1 List of Abbreviations

AC	alternating current
AV	alternating voltage
CC	constant current
CDC	carbide derived carbon
CDI	capacitive deionization
CMOS	complementary-metaloxide-semiconductor
CsAc	cesium acetate
CV	cyclic voltammetry
EA	elemental analysis
EDLC	electric double layer capacitor
EELS	electron energy loss spectroscopy
EIS	electrical impedance spectroscopy
[EMIM][BF4]	1-ethyl-3-methylimidazolium tetrafluoroborate
ESR	electrical series resistance
EV	electric vehicle
FTIR	Fourier transform infrared spectroscopy
GNU	general public license
HEV	hybrid electric vehicle
HMF	hydroxymethylfurfural
HTC	hydrothermal carbonization
IL	Ionic liquid
LBAE	Lobry de Bruyn - Alberda van Ekenstein
LIB	lithium ion battery
LSB	lithium sulfur batteries
NMR	nuclear magnetic resonance spectroscopy
OCV	open circuit voltage
PTFE	poly tetra fluoro ethylene
PvdF	polyvinylidene fluoride
QSDFT	quenched solid state density functional theory
SC	supercapacitor
SEM	scanning electron microscopy
TC	thermal carbonization
TCA	2-thiophenecarboxylic acid
(HR)TEM	(high resolution) transmission electron microscopy

TGA	thermo gravimetric analysis
XPS	X-ray photoelectron spectroscopy
XRD	X-ray diffraction

2 Applied Methods / Machines

Electrochemical characterization

All supercapacitor tests in 1 M sulfuric acid were recorded on a gamry interface 1000 potentiostate. The SC tests in 1 M sodium chloride solution and the LSB test were performed on a Bio-Logic VMP3.

Elemental analysis (EA)

EA for carbon, nitrogen, hydrogen and sulfur was carried out using a Vario El elemental analyzer.

Fourier-transform infrared spectroscopy (FTIR)

FTIR spectra were recorded on a Varian600 FT-IR spectrometer. The samples were investigated using the ATR (Attenuated total reflectance) mode without any sample preparation.

Nitrogen sorption

The N_2 sorption tests were conducted on a Quantachrome Masterprep system at 77 K. The samples were degassed at 150 °C for at least 20 h under vacuum. The sulfur impregnated carbon samples have been degassed at room temperature under vacuum over for 48 h.

Scanning electron microscopy (SEM)

SEM images were recorded using a Gemini Leo-1550 instrument with an acceleration voltage of 0.1 to 30 kV. The samples were prepared by placing well-grounded powder onto carbon tape and subsequent sputtering with Au/Pd.

Thermo gravimetric analysis (TGA)

TGA data were recorded using a Netzsch TG 209 at a heating rate of 10 K min^{-1}. All samples were investigated using Al_2O_3 crucibles.

Transmission electron microscopy (TEM)

TEM images were taken using a Carl Zeiss Omega 912X with an acceleration voltage of 120 kV. The samples were prepared by dispersing a small amount in abs. ethanol and subsequent drop-casting onto carbon coated copper grids.

High resolution TEM images were recorded on a Philips, CM200FEG microscope (200 kV), equipped with a field emission gun.

X-Ray diffraction (XRD)

XRD diffraction pattern were recorded using a Bruker D8 Advance diffractometer with a Cu-K_α ($\lambda = 0.154$ nm) radiation source. XRD pattern were recorded over a 2 theta range from 5 to 60 ° using a step size of 0.05 °.

3 Experimental Details

3.1 Part B

3.1.1 Hydrothermal Synthesis of N-doped Carbon Monoliths

In a typical synthesis, 5 g glucose and 1 g borax were dissolved in 20 mL of deionized water. Furthermore 1, 1.5 and 2 mL of an ammonia solution (25% in water) was added to achieve a mass ration of glucose to ammonia of 1:0.25, 1:0.50 and 1:0.75, respectively. The solution was transferred into a glass inlet and placed in a teflon lined, stainless steel autoclave (45 ml volume, purchased from Parr Instruments). The autoclave was placed in a pre-heated oven at 200 ° C for 20 h. After cool down to room temperature the obtained carbon monoliths were thoroughly washed with water and ethanol until the washing solution was of light yellow color, afterwards the monoliths were submerged in water. The products were dried using a flash freeze-drying technique. In short, liquid nitrogen was poured onto the monoliths until they were frozen followed by freeze-drying.

3.1.2 Carbonization and CO_2 activation

The pyrolysis and activation was carried out in one step. Usually 500 mg of the samples were placed in a ceramic crucible, which was placed in a nitrogen furnace. The system was purged for 30 min followed by heating to 850 ° C at 8.5 K min^{-1}. The temperature was kept constant for 3 h. After 1.5 h at constant temperature the gas flow was switched to CO_2 for 1.5 h in order to activate the carbon materials. Finally the samples were cooled down under nitrogen flow.

3.2 Part C

3.2.1 Salt Melt Synthesis of Porous Carbons

For the salt template synthesis 1 g of glucose or glucosamine hydrochloride was dissolved in 20 mL of deionized water (250 mg of TCA was added for the sulfur doped samples). The respective salt template ($ZnCl_2$ and/or CsAc) was added in a 1:1 or 1:5 (glucose:salt) ratio. The solution was subsequently transferred into a ceramic crucible and placed in a tube furnace. The furnace was kept under a nitrogen atmosphere throughout the carbonization. The samples were heated to 300 ° C (1 K min^{-1}), followed by a final carbonization at 800, 900 or 1000 ° C (4.5 K min^{-1}). All samples were washed in deionized water for 24 h after the carbonization and subsequently dried at 60 ° C under vacuum.

3.2.2 Test procedures for UV/VIS absorption test of Polysulfides

The polysulfides Li_2S_8, Li_2S_6, Li_2S_4 and Li_2S_3 were synthesized by mixing the respected stoichiometric amount of metallic lithium with sulfur, dissolved in tetrahydrofuran. The mixtures were prepared inside an argon filled glovebox and stirred for 2 weeks followed by a subsequent evaporation of the tetrahydrofuran under nitrogen flow using a schlenk line. The as prepared poly sulfides were dissolved in tetrahydrofuran to yield 1, 2.5, 5 and 10 mM solutions. Those solutions were used to calibrate the UV/Vis spectrometer.

The sorption test itself was performed by dispersing 10 mg of carbon sample in 5 mL of a 10 mM polysulfide solution. The dispersion was stirred for 24 h to ensure complete adsorption of the polysulfides by the carbon material. Each polysulfide was tested separately with the following wavelengths: $\lambda(Li_2S_8)$: 567 nm; $\lambda(Li_2S_6)$: 538 nm; $\lambda(Li_2S_4)$: 514 nm and